UCLA

UCLA Electronic Theses and Dissertations

Title

Thermofluidics of Sulfur-based Thermal Energy Storage

Permalink

https://escholarship.org/uc/item/3xm3j1bp

Author

Jin, Kaiyuan

Publication Date

2019

Peer reviewed|Thesis/dissertation

UNIVERSITY OF CALIFORNIA

Los Angeles

Thermofluidics of Sulfur-based Thermal Energy Storage

A dissertation submitted in partial satisfaction
of the requirements for the degree

Doctor of Philosophy in Mechanical Engineering

by

Kaiyuan Jin

©Copyright by

Kaiyuan Jin

2019

ABSTRACT OF THE DISSERTATION

Thermofluidics of Sulfur-based Thermal Energy Storage

by

Kaiyuan Jin

Doctor of Philosophy in Mechanical Engineering
University of California, Los Angeles, 2019
Professor Richard E. Wirz, Advisor

Thermal energy storage (TES) is crucial for future low-cost and large-scale (GWh) energy use and supply. Sulfur as a storage medium provides exceptional TES system cost efficiency and performance due to several characteristics, including low cost, high availability, excellent thermal stability up to 1200 °C, high heat transfer rates, and impressive material compatibility when compared to existing and competing options. The sulfur-based TES (SulfurTES) systems analogous to shell-and-tube heat exchanger have been successfully demonstrated with attractive energy density and system stability. In such systems, the sulfur heat transfer behavior in isochoric containers play a critical role in performance prediction and optimization and need to be fully understood and quantified.

This dissertation discusses recent studies on sulfur's thermofluidic behavior during thermal charge and discharge for several isochoric configurations. The first study compares experiments and computational analyses performed at UCLA of sulfur inside vertically oriented steel tubes undergoing 25 to 600 °C charge and discharge. The study developed and validated the Nusselt number correlations

to show that low aspect ratio (length/diameter < 7) tubes, when uniformly heated, provide heat transfer performance superior to horizontal tubes.

In comparison to uniform-heating, nonuniform thermal charge including top-heating and bottom-heating are more likely to be encountered in practical SulfurTES with isochoric-tube configuration. In the second study of this dissertation, the combination of experimental and computational investigations elucidates the top-heated sulfur tube exhibits a stable thermal stratification, which leads to superior exergetic performance. On the other hand, bottom-heating scenarios cause rapid mixing between hot and cold sulfur, resulting in high charge rates. With the developed correlations, two analytical procedures are originally proposed and allow estimation of the energy and exergy performance of sulfur in tubes of different sizes with top-heating and bottom-heating, respectively.

In comparison to the isochoric-tube system wherein the sulfur is stored and sealed within multiple tubes, a "bath" configuration is proposed to potentially provide a simplified configuration and attractive thermal performance by maintaining the bulk of sulfur inside a large shell with an array of thermal charge tubes near the bottom and discharge tubes at the top. Validated computational models allow the characterization of sulfur heat transfer behavior dominated by multiple geometric parameters in the bath system. Nusselt number correlations based on Rayleigh number and tube pitch ratio have been developed and utilized for the system parametric design. The preliminary comparison between the tube- and bath-configuration systems proves the potential superiority of the bath system on thermal performance and cost for the industrial-scale thermal storage applications.

All the results in this dissertation provide important qualitative and quantitative heat transfer descriptions and design bases for SulfurTES systems. The observations from these studies and the investigation methods and tools can be utilized in future studies and will encourage further investigations for other novel thermal storage technologies.

The dissertation of Kaiyuan Jin is approved.

Adrienne G. Lavine

Hossein Pirouz Kavehpour

Dante A. Simonetti

Richard E. Wirz, Committee Chair

University of California, Los Angeles
2019

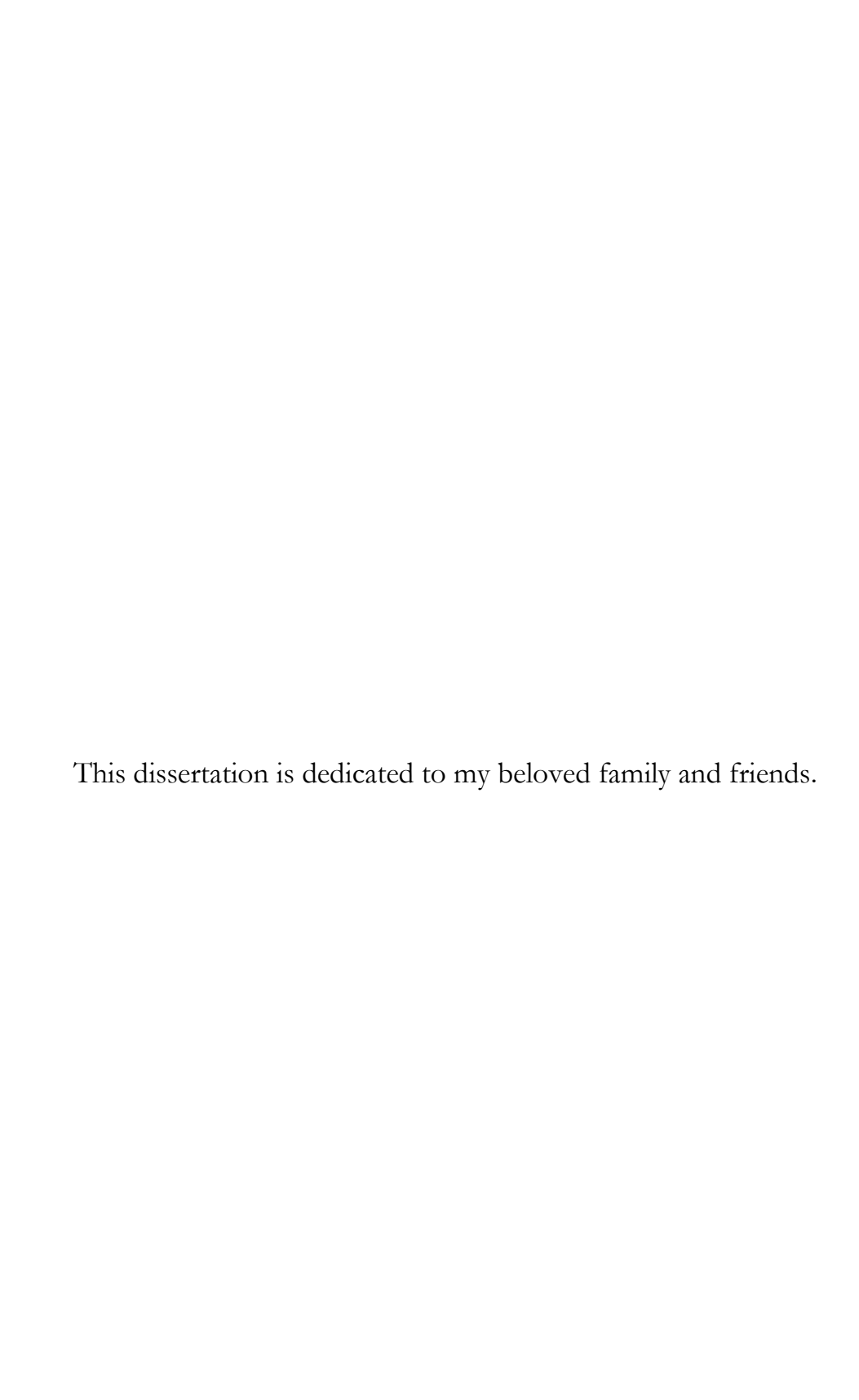


Table of Contents

ABSTRAC	T OF THE DISSERTATION	ii
List of Fig	ures	ix
List of Tal	bles	XV1
List of Syn	nbols	XV11
Acknowled	lgements	xix
Vita		XX
Chapter 1	Introduction	1
1.1.	Scope of TES implementation	1
1.2.	SulfurTES technology	3
1.3.	Objective of study	4
1.4.	Overview of dissertation	5
Chapter 2	Background	7
2.1.	TES mechanisms and storage materials	7
2.2.	Current TES technologies	11
2.3.	Figures of merit for TES system	18
2.4.	Characteristics of sulfur as a storage medium	19
2.5.	Design of SulfurTES system	27
Chapter 3	Sulfur heat transfer in vertical tubes with uniform charge and discharge	32

3.1. Experimental study	33
3.1.1. Experimental system	33
3.1.2. Results and discussions	34
3.2. CFD study	38
3.2.1. Model development	38
3.2.2. Grid size refinement and time step study	42
3.2.3. Model validation	43
3.2.4. Results and discussions	45
3.3. Heat transfer performance analysis	47
3.3.1. Empirical correlations for Nusselt number	47
3.3.2. Comparison with horizontal-oriented tubes	50
3.4. Conclusions	57
Chapter 4 Sulfur heat transfer in vertical tubes with nonuniform char	ge58
4.1. Experimental study	60
4.2. CFD study	64
4.2.1. Experimental boundary conditions	65
4.2.2. Canonical boundary conditions	69
4.3. Heat transfer performance analysis	73
4.3.1. Energy and exergy analysis	73
4.3.2. Simplified numerical methods	77

4.3.3. Nusselt number correlation	85
4.4. Conclusions	86
Chapter 5 Sulfur heat transfer behavior in bath-configuration TES systems	88
5.1. CFD study	89
5.1.1. Model development	89
5.1.2. Parametric study	95
5.2. Thermal performance analysis	110
5.3. Comparison with isochoric tube configuration	113
5.4. Conclusions	115
Chapter 6 Conclusions and future work	116
Appendix A: Insulation system study	118
Appendix B: Demonstrations of SulfurTES thermal battery system	130
Appendix C: Performance analysis for the heat transfer fluid (HTF) side in SulfurTES	S bath systems
	138
References	1./3

List of Figures

Figure 1.1. Rendering of 390-MW CSP power with 5.1-GWh _t molten salt-based TES in Likana, Chile.
[1] (Graphic: Business Wire [2])
Figure 1.2. Schematic for CHP applications with TES in (a) energy charge process and (b) energy
discharge process
Figure 1.3. Schematic of CSP application integrated with a SulfurTES system
Figure 2.1. Main mechanisms for TES: (a) sensible heat storage, (b) latent heat storage, and (c)
thermochemical energy storage
Figure 2.2. Schematic of CSP plant with a two-tank molten salt TES system
Figure 2.3. Schematic of CSP plant with thermocline molten salt TES system
Figure 2.4. Schematic of CSP plant with a rock-based TES system
Figure 2.5. Schematic of CSP plant with (a) encapsulated (b) shell-and-tube LHTES system15
Figure 2.6. Schematic of CSP plant with ammonia-based thermochemical storage system18
Figure 2.7. The chemical reaction of liquid sulfur from 119 to 445 °C
Figure 2.8. The viscosity of pure sulfur in an open system [57], impure sulfur in an open system [58,59],
and impure sulfur in a closed system [58].
Figure 2.9. The chemical reaction of gaseous sulfur[6].
Figure 2.10. Sulfur properties in isochoric system: (a) Density, (b) heat capacity, (c) thermal
conductivity, and (d) viscosity
Figure 2.11. Thickness measurements for the sulfur tubes of various containment materials before and
after the multiple thermal tests. (a) SEM pictures, (b) measurement results
Figure 2.12. Preliminary analysis for the storage cost of competitive TES technologies

Figure 2.13. (a) Schematic of SulfurTES thermal battery system in horizontal-tube configuration.
(b) The lab-scale and (c) the pilot-scale demonstration of the Sulfur TES thermal battery system29
Figure 2.14. Schematic of SulfurTES system in (a) vertical tube configuration and (b)bath
configuration31
Figure 3.1. Schematic of the SulfurTES thermal battery system with vertically-oriented tubes32
Figure 3.2. (a) Picture, and (b) schematic of the experimental facility. (c) Schematic of the
instrumentations
Figure 3.3. Temperature variation of uniform surface temperature condition. (a) Heated from room
temperature to 200 $^{\circ}$ C, (b) heated from 200 $^{\circ}$ C to 600 $^{\circ}$ C37
Figure 3.4. (a) Sulfur viscosity variations: pure sulfur in an open system, impure sulfur in an open
system, and impure sulfur in a closed system. (b) Impure sulfur viscosity and the temperature
difference between the tube wall and sulfur
Figure 3.5. Computational domain and boundary conditions
Figure 3.6. Grashof number for pure and impure sulfur vs. criterion for buoyancy-driven flow
transition to the turbulent regime
Figure 3.7. Grid size refinement study: comparison of one of the local sulfur temperatures (inside the
boundary layer)43
Figure 3.8. Comparison of sulfur temperature variation in experiments and from computational
model: (a) Locations of thermocouples in the experimental system, (b-g) transient temperature
variation of TS1 – TS6
Figure 3.9. Transient variations in sulfur temperature, velocity and viscosity (a) temperature, (b)
viscosity. (c) z-velocity

Figure 3.10. (a) Transient variation of average sulfur and wall temperature, (b) transient variation of
heat transfer coefficient and viscosity47
Figure 3.11. Variation of average Nusselt number with average Rayleigh number for (a) charge
condition and (b) discharge condition
Figure 3.12. Comparison of the dimensionless sulfur temperature from analytical solutions with the
CFD results50
Figure 3.13. Comparison of volumetric-average sulfur temperature variation for (a) charge process
and (b) discharge process in the vertical and horizontal tubes
Figure 3.14. Comparison of (a)thermal charge rate, (b) thermal discharge rate, and heat transfer
coefficient for (c) charge, (d) discharge in vertical and horizontal tubes
Figure 3.15. Comparison of relative charge and discharge heat transfer coefficient for tube dimensions
(length and diameter) and orientation (vertical or horizontal). (Region A: $h_{vert,c} > h_{horiz,c}$
$h_{vert,d} > h_{horiz,d}$. Region B: $h_{vert,c} > h_{horiz,c}$; $h_{vert,d} < h_{horiz,d}$. Region C: $h_{vert,c} < h_{horiz,c}$
$h_{vert,d} > h_{horiz,d}$. Region D: $h_{vert,c} < h_{horiz,c}$; $h_{vert,d} < h_{horiz,d}$)
Figure 4.1. Schematics of thermal charging in thermal battery SulfurTES system in (a) top-heating
scenario, (b) bottom-heating scenario59
Figure 4.2. The steady-state axial temperature profile of the system in the first heating stage for (a) the
top-heating scenario and (b) the bottom-heating scenario.
Figure 4.3. Temporal axial temperature profile of the system in the second heating stage for (a) the
top-heating scenario and (b) the bottom-heating scenario.
Figure 4.4. Comparison of sulfur temperature variation in the experiments and the computational
model: (a-f) the top-heating scenario, (g-l) the bottom-heating scenario

Figure 4.5. Contours of (a) temperature and streamlines, (b) viscosity, (c) z-velocity in the top-heating
scenario, (d) temperature and streamlines, (e) viscosity, and (f) z-velocity in the bottom-heating
scenario. 69
Figure 4.6. Imposed wall temperature for canonical boundary condition studies. (a)top-heating
(b)bottom-heating, (c) uniform-heating scenarios.
Figure 4.7. Contours of temperature and streamlines in (a) top-heating, (b) bottom-heating, and (c)
uniform-heating scenarios; and contours of axial velocity (z-velocity) in (d) top-heating, (e) bottom-
heating, and (f) uniform-heating scenarios for canonical charge study.
Figure 4.8. Temporal energy and exergy variations in the canonical boundary condition study
(a) Energy variation, (b) Energy charge rate variation, (c) exergy variation, (d) Exergy charge rate
variation
Figure 4.9. Charge time for the top-heating, bottom-heating, and uniform-heating scenarios: (a)
Energy charge time and (b) exergy charge time
Figure 4.10. (a) Schematic of the sulfur tube under top-heating charge condition. Comparison of CFD
and TOP procedure results for the (b) experimental and (c) canonical cases
Figure 4.11. (a) Schematic of the sulfur tube under the bottom-heating charge condition. Comparison
of CFD and the BOT procedure results for the (b) experimental and (c) canonical cases
Figure 4.12. Transient variation of (a) charged energy in the experimental cases and (b) the canonical
cases; transient variation of (c) charged exergy in the experimental cases and (d) the canonical cases
Figure 4.13. Variation of average Nusselt number with average Rayleigh number for (a) charge
condition and (b) discharge condition for tube length between 0.1 and 0.5 m
Figure 5.1. Schematic of the SulfurTES both system

Figure 5.2. Schematic of natural convection in SulfurTES bath system90
Figure 5.3. 2D computational domain of SulfurTES bath system with the main geometric parameters
91
Figure 5.4. (a) Schematic of the mesh for sulfur domain and variation of (a) average sulfur temperature
and (b) heat transfer coefficient in grid size refinement study93
Figure 5.5. (a) Schematic of the CFD model with modified settings and (b) comparison between the
results from this CFD model and the previous empirical correlations
Figure 5.6. Schematic of the computational domains with single and multiple tubes96
Figure 5.7. (a) Temperature and streamlines contours, (b) variation of the average sulfur temperature,
and (c) variation of the heat transfer coefficient in the charge scenarios for the single and multiple-
tube domains
Figure 5.8. (a) Temperature and streamlines contours at $T_S \approx 400$ °C, (b) variation of the average
sulfur temperature, and (c) variation of the heat transfer coefficient in the charge scenarios for the
bath system with $H = 12.5, 25$, and $50D$
Figure 5.9. Schematics for computational domains with various D and p in the design space 103
Figure 5.10. Temperature and streamlines contours ((a), (c), (e) and (g)) and the variation of the heat
transfer coefficients ((b), (d), (f), and (h)) for the sulfur in bath system with various geometric
parameters
Figure 5.11. Linear curve fit for (a) $lnNu_{D,avg}$ and $lnRa_{D,avg}$ and (b) lny and lnx
Figure 5.12. Comparison of Nu number from CFD results and the developed correlation in Equation
(5.12)
Figure 5.13. Comparison of CFD and analytical solutions for the average sulfur temperature variation
in the bath system with (a) $D = 5$ mm and (b) $D = 40$ mm

Figure 5.14. Variation of average heat transfer coefficient: (a) 3D plot, (b) 2D plot with D as	the x-
axis, and (c) 2D plot with p as the x-axis. Variation of energy charge rate: (a) 3D plot, (b) 2D plot	ot with
D as the x-axis, and (c) 2D plot with p as the x-axis.	111
Figure A-1. Thermal conductivity of microporous insulation (as a function of T ³)	121
Figure A-2. (a) Schematic and (b) thermal circuit for multilayer insulation system	122
Figure A-3. (a) Picture, (b) Schematic, (c) thermocouple position map for the experimental s	system
with flat-plate configuration	124
Figure A-4. Comparison of the average central outside temperature for the insulation sample be	tween
the experimental and analytical results	125
Figure A-5. Pictures ((a) without reflective layer, (b) with reflective layer)) and (c) schematic	of the
experimental system in tube-configuration	126
Figure A-6. Comparison of the average central outside temperature for the insulation samp	ple (a)
without reflective layer and (b) with reflective layer in the tube-configuration experimental system	n127
Figure A-7. Variation of total heat loss with (a) various space between adjacent reflective layer	rs, and
(b) number and emissivity of the reflective layers	129
Figure B-1. (a) The picture and the design schematic for the lab-scale SulfurTES and (b) sche	ematic
for the sulfur storage tube in the lab-scale SulfurTES	130
Figure B-2. Installation procedures of the lab-scale SulfurTES	131
Figure B-3. Picture of the lab-scale SulfurTES system with a PID air heater	132
Figure B-4. (a) Inlet temperature for continuous 12 thermal cycles for the lab-scale SulfurTES s	system
with a PID air heater	133
Figure B-5. (a) The picture and (b) the schematic for the pilot-scale SulfurTES	134

Figure B-6. Key components of the on-sun CSP system: (a) parabolic mirrors, (b) concer	ntration of
solar energy at the receiver, (c)photosensor, (d) vertical drive, and (e) horizontal drive	135
Figure B-7. Schematics and pictures of the solar receiver	136
Figure B-8. Pictures of the key components for the pilot-scale SulfurTES	136
Figure B-9. (a) The temperature distribution of sulfur storage tubes and (b) thermal storage	ge capacity
in SulfurTES thermal battery during thermal charge process	137

List of Tables

Table 3.1. Thermal charge and discharge periods for vertical and horizontal tubes
Table 3.3. Charge and discharge heat transfer coefficient for vertical and horizontal 1-meter long tubes.
53
Table 4.1. Errors for TOP and BOT procedure on predicting energy and exergy variation84
Table 5.1. Average heat transfer coefficient (from 200 to 550 °C) for various computational domains
(Unit: W/m ² ·K)
Table 5.2. Average heat transfer coefficient (from 200 to 550 $^{\circ}$ C) for various system height, H (Unit:
$W/m^2 \cdot K$)
Table 5.3. Average heat transfer coefficient (from 200 to 580 °C) for various tube diameter, D and
pitch ratio, p (Unit: W/m²·K)
Table 5.4. Comparison among the 1MWh Sulfur TES systems with tube- and bath-configuration 114
Table A-1. High-temperature insulation materials
Table C-1. HTF-side heat transfer coefficients and system pressure drop for SulfurTES systems with
tube- and bath-configuration141

List of Symbols

A	surface average [m²]
c_p	specific heat [J/kg·K]
D	tube diameter [cm]
e	internal thermal energy [J]
E	energy [J]
f	friction factor
g	gravitational acceleration [m/s ²]
Gr	Grashof number
h	heat transfer coefficient [W/m²-K]

h heat transfer coefficient [W/m²-K]
 k thermal conductivity [W/m-K]
 L tube length [m]

L tube length [m]N number of tubesNuNusselt number

p pressure [Pa] or tube pitch ratioP thermal charge rate [kW/kg]

PrPrandtl numberrradial coordinate [m]RaRayleigh numberRtube radius [m]

t time [s]

V volume [m³] W width [m]

v axial velocity [m/s] z axial coordinate [m]

Subscripts and Superscripts

avg average b bath btmbottom С charge \mathcal{C} characteristic condconduction crosscross-section d discharge effeffective

H heater

horiz horizontal configuration

i initial
o overall
rad radiation
S sulfur
t tube

vert vertical configuration

w wall

Greek Symbols

 α thermal diffusivity [m²/s]

 β thermal expansion coefficient [1/K] θ dimensionless sulfur temperature

 $\begin{array}{ll} \mu & \text{viscosity } [\text{Pa·s}] \\ \rho & \text{density } [\text{kg/m}^3] \end{array}$

 $\vec{\tau}$ viscous stress tensor [Pa]

Acronyms

CFD computational fluid dynamics
CSP concentrated solar power
CHP combined heat and power

HTF heat transfer fluid NPS nominal pipe size OD outer diameter ID inner diameter

sCO₂ supercritical carbon dioxide TES thermal energy storage

SulfurTES sulfur-based thermal energy storage

Acknowledgments

I would like to express my appreciation to many wonderful people that helped me with this thesis and other important achievements during my Ph.D. life. First, I sincerely thank my advisor, Prof. Richard Wirz, who is an excellent professor and mentor on so many levels. With his patient and insightful guidance, I have changed from a person knowing little about scientific research to a motivated researcher aiming to lead new frontiers in technology advancement and make the world a better place. In addition to my advisor, I want to appreciate Prof. Adrienne, Prof. Pirouz Kavehpour, and Prof. Dante Simonetti for serving on my doctoral committee and providing instructive comments on my thesis. I owe much gratitude to my colleagues in the Wirz Research Group at UCLA, including members of the Energy Innovation Lab: Dr. Amey Barde, Dr. Karthik Nithyanandam, Dr. Zhitong Chen, Yide Wang, Siddhesh Naik, Mitchell Shinn, Parker Wells, as well as all the members of the Plasma & Space Propulsion Lab, who helped me immensely with adapting to life in the United States and UCLA, as well as completing challenging research tasks. I am also extremely grateful to all my friends, specially Shuaihang Pan and Xiangwei Zhang, for bringing me pleasure and lightening my life during these four years. At last, I would like to present my acknowledgments to my parents and other family members. Their love and encouragement motivate me to constantly challenge myself and become a better person. To all the people who have ever helped me, "Thank you!"

Funding for this research was provided by the Southern California Gas Company Grant Nos. 5660042510, 5660042538, and California Energy Commission Contract No. EPC-14-003, with early funding by the Dept. of Energy ARPA-E award DE-AR0000140. I would like to acknowledgment these funding agencies and thank Prof. Vijay Dhir and Prof. Adrienne Lavine for sharing the lab space needed for the relevant experimental work.

Vita

2015 - 2019	Graduate Student Researcher, Mechanical and Aerospace Engineering
	Department, UCLA.
2011 - 2015	Bachelor of Science in Thermal Engineering, Tsinghua University,
	China.

Publications

K. Jin, R. E. Wirz. "Thermal charge and discharge performance of sulfur in bath-configuration thermal energy storage systems." In preparation.

K. Jin, R. E. Wirz. "Sulfur heat transfer behavior in vertically-oriented and nonuniformly-heated isochoric thermal energy storage systems." *Applied Energy*, in revision.

Y. Wang, A. Barde, **K. Jin**, R. E. Wirz. "System performance analysis of sulfur-based thermal energy storage." *Energy*, in revision.

K. Jin, A. Barde, K. Nithyanandam, R. E. Wirz. "Sulfur heat transfer behavior in vertically-oriented isochoric thermal energy storage systems." *Applied Energy* 240 (2019): 870-881.

A. Barde, **K. Jin**, M. Shinn, K. Nithyanandam, R. E. Wirz. "Demonstration of a low cost, high temperature elemental sulfur thermal battery." *Applied Thermal Engineering* 137 (2018): 259-267.

Chapter 1

Introduction

Thermal energy storage (TES) is an important component of modern energy infrastructures, such as concentrated solar power (CSP) and combined heat and power (CHP), for its ability to provide dispatchability and flexibility to energy supply. Utilizing element sulfur as storage materials can potentially provide much lower cost and better thermal stability for high-temperature systems than the existing technologies. However, the heat transfer behavior of sulfur in isochoric systems, dominating the thermal performance of most sulfur-based TES (SulfurTES), has not been fully understood. Therefore, this dissertation is written to carefully investigate this heat transfer physics and provide critical design and optimization bases of the SulfurTES systems.

This chapter introduces the motivation of this dissertation by identifying the needs and the advantages of SulfurTES technologies and summarizes the main objectives of the current study. Section 1.1 shows the existing and potential TES applications and the main benefits of TES implementation. Section 1.2 discusses the potentials and current challenges of SulfurTES technology. Section 1.3 lists the main objectives of this dissertation. Section 1.4 overviews this dissertation chapter by chapter and introduces the experimental and computational studies of sulfur heat transfer behavior in different systems.

1.1. Scope of TES implementation

Power generation with renewables becomes one of the promising options to solve the worldwide energy crisis and increasingly severe environmental problems by utilizing fossil fuels. Solar is the most abundant renewable energy resources on our planet and can potentially feed the energy demand for the whole community. However, the intermittency of solar energy can cause unbearable dispatching pressure on the grid during solar power generation processes. Energy storage, providing necessary dispatchability for the grid or energy supply, is very important for these power generation applications. In comparison to other energy storage technologies, such as battery, TES is more appropriate for utility-scale applications due to its low costs and long-term durations and therefore is widely applied in concentrated solar power (CSP) plants all over the world. Figure 1.1 shows the 390-MW CSP power with 5.1-GWh_t molten salt-based TES in Likana, Chile.

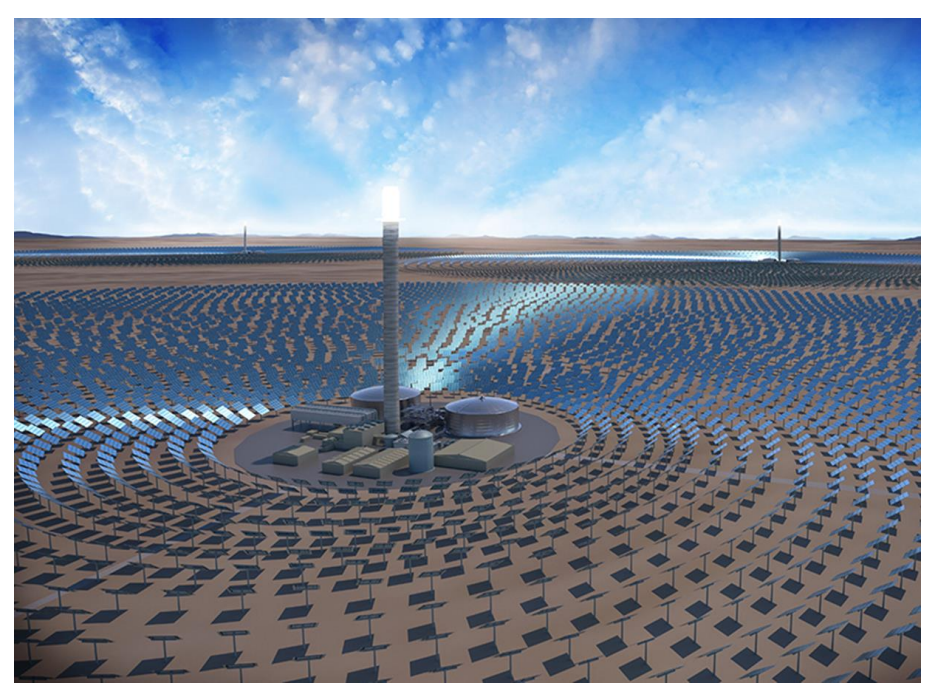


Figure 1.1. Rendering of 390-MW CSP power with 5.1-GWh_t molten salt-based TES in Likana, Chile. [1] (Graphic: Business Wire [2])

In addition to solar power generation, the combined heat and power (CHP) applications, in which the industrial processes demanding both power and heat are integrated with a power plant, can also benefit from energy storage. The implement of TES can improve system flexibility and economic benefits [3,4], as shown in Figure 1.2.

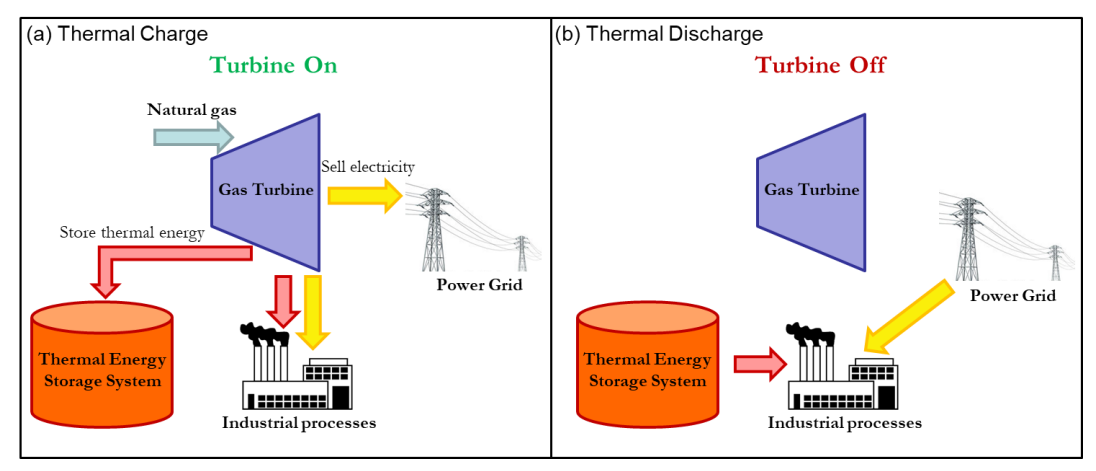


Figure 1.2. Schematic for CHP applications with TES in (a) energy charge process and (b) energy discharge process.

1.2. SulfurTES technology

Element sulfur is of abundant reserves on our planet and is oversupplied as a byproduct from the petroleum industry. The price of elemental sulfur is around \$40-160/ton [5], which is much lower than the competitive storage materials, such as molten salt and phase change materials (PCMs). Furthermore, as an element, sulfur has a very good thermal stability in isochoric containers at high temperature up to 1200 °C [6]. Therefore, sulfur is a promising storage material for low-cost and high temperature TES. UCLA researchers have proposed a SulfurTES system with sulfur stored in isochoric systems, as shown in Figure 1.3 [7]. Multiple analyses [8,9] show that SulfurTES can achieve attractive cost efficiency, thermal stability, and material compatibility with the stainless-steel containment. The current challenge for this technology is to better understand the sulfur heat transfer behavior and further investigate the thermal performance for SulfurTES.

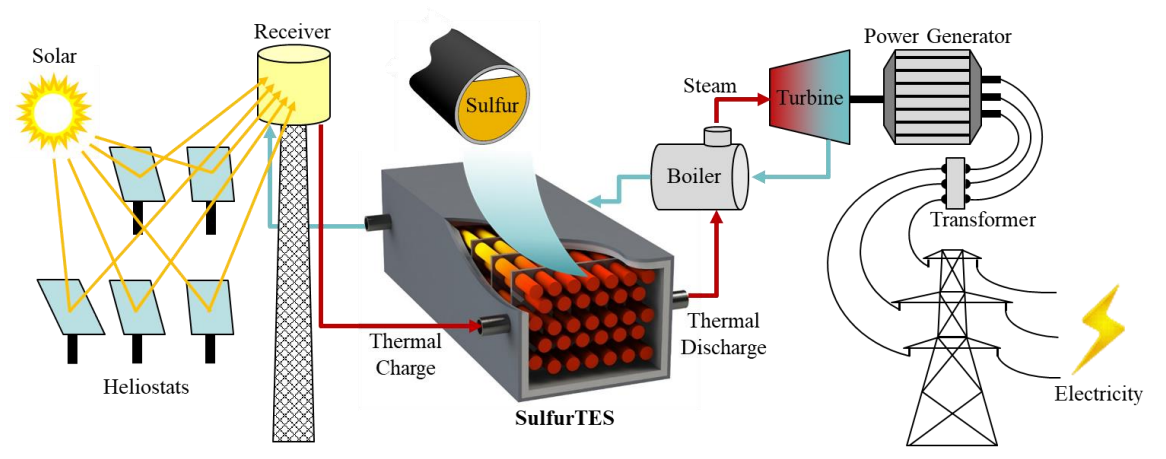


Figure 1.3. Schematic of CSP application integrated with a SulfurTES system.

1.3. Objectives of the study

There're two main conceptual designs for the SulfurTES system: tube-configuration (or named as thermal battery) system and bath-configuration system. In the tube-configuration system, sulfur is stored in multiple isochoric tubes. These storage tubes are enclosed in a shell-and-tube heat exchanger system and heat transfer fluid is pumped into the shell to thermally charge and discharge the sulfur tubes. The previous study has studied the heat transfer performance of horizontally-oriented storage tubes. In comparison to the horizontal configuration, orienting the sulfur tubes in vertical orientation can potentially provide better heat transfer performance, better thermocline behavior, lower cost, and ease of operation and maintenance. The bath-configuration SulfurTES is also analogous to shell-and-tube heat exchanger. In this system, sulfur is stored in the shell and the heat transfer fluid flows through the tubes. This design has potentials to provide lower system costs due to the less usage of containment materials.

Both SulfurTES configurations are of author's interests and therefore the purposes of this dissertation are:

• Study sulfur heat transfer behavior in vertically-oriented isochoric storage tubes under uniform charge and discharge condition.

- Study sulfur heat transfer behavior in vertically-oriented isochoric storage tubes under nonuniform charge and discharge condition.
- Study sulfur heat transfer behavior in bath configuration TES systems.

1.4. Overview of dissertation

In this dissertation, Chapter 2 introduces the background by demonstrating the pros and cons of the existing TES technologies and the characteristics of sulfur as a storage material. I elucidated why the element sulfur can be a promising storage medium for future TES systems. In addition, the heat transfer physics in isochoric storage tubes are also discussed in detail to show the expected thermal performance of sulfur in vertically-oriented isochoric TES tubes.

Chapter 3 presents the study of sulfur heat transfer behavior in vertically-oriented storage tubes with uniform thermal charge and discharge conditions. Section 3.1 introduces the experimental study and discusses the characteristics of heat transfer physics. In section 3.2, I developed a 2-D CFD model to further investigate this phenomenon. The model is successfully validated by the experimental data and provides critical results of sulfur heat transfer performance in the system of various sizes. With the computational results, I developed Nusselt number correlations in section 3.3. In addition, with the developed correlation, an analytical analysis is conducted to quantitively compare the heat transfer rate of sulfur in vertical and horizontal orientated tubes.

In the tube-configuration system, some sulfur storage tubes are thermally charged by the heat transfer fluid from one end to the other, causing nonuniform boundary conditions. Due to the gravity effect, these heat transfer phenomena can be very different from those under uniform charge/discharge conditions. Therefore, I studied sulfur heat transfer behavior in vertically-oriented storage tubes with two nonuniform charge conditions in Chapter 4. Section 4.1 and 4.2 present the experimental and computational study, respectively. In section 4.3, I compared the energy and exergy

charge rate of sulfur under all nonuniform and uniform charge conditions. The simplified analytical procedures were developed afterward to provide efficient and accurate predictions of sulfur energy and exergy charge performance under these nonuniform charge conditions.

In Chapter 5, I conducted a CFD study on sulfur natural convection in bath-configuration TES systems. Section 5.1 introduces the CFD study including model development, grid sizes and time steps study, and parametric study. Section 0 shows the development of Nusselt number correlations and the analytical system heat transfer performance.

Chapter 6 concludes that all the studies in this dissertation provide a good understanding of sulfur heat transfer physics and qualitative and quantitative design bases for different SulfurTES systems. Future efforts will focus on system-level performance study and optimization of SulfurTES.

Other important efforts relevant to this dissertation are summarized in Appendix A to C.

Chapter 2

Background

To increase the dispatchability of the intermittent energy resources, the storage of energy in forms of thermal energy has drawn increasing attention in recent years. Researchers have proposed and developed multiple TES technologies with various storage materials, e.g. molten salt, phase change materials (PCMs) and sulfur. In this chapter, section 2.1 to 2.3 discuss and compare the characteristics of the existing technologies and section 2.4 explains the potential advantages of using sulfur as the storage materials. Section 2.5 introduces various SulfurTES system design.

2.1. TES mechanisms and storage materials

The main mechanisms for TES technologies include sensible heat, latent heat, and thermochemical heat storage [10-13]. In TES applications, the thermal energy can be stored in forms of one or the combination of these internal energies of the storage materials.

Sensible heat storage

Sensible heat storage is based on the temperature change of media in the solid or liquid phase. The capacity of stored thermal energy satisfies following equations and Figure 2.1(a):

$$E_T = \int_{T_i}^{T_f} m c_p dT \tag{2.1}$$

where T_f is final temperature and T_i is the initial temperature for the thermal charge process. m and c_p is the total mass and specific heat of storage materials. From this equation, the operating temperature range, total amount of storage materials, and the specific heat dominate the amount of

energy storage. Therefore, materials with large specific heat, operating temperatures, and low cost can be potential excellent storage media.

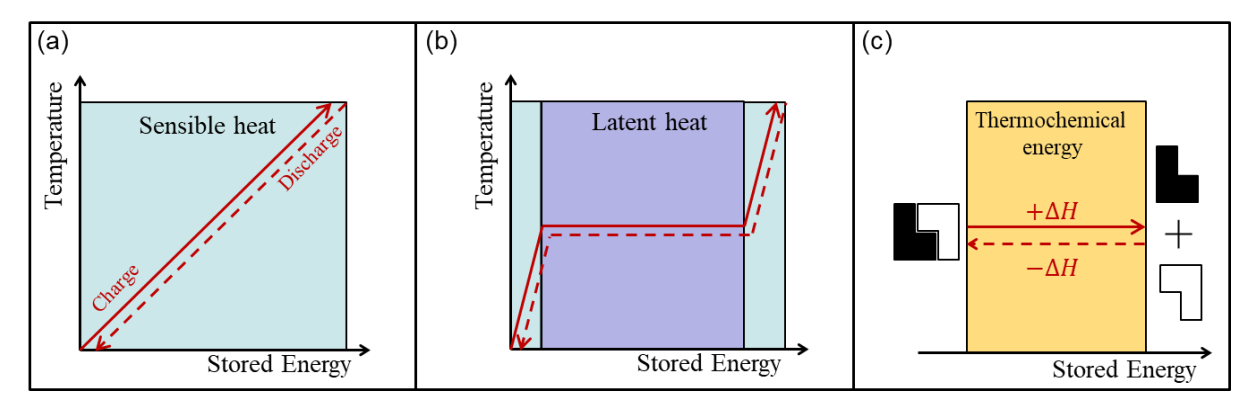


Figure 2.1. Main mechanisms for TES: (a) sensible heat storage, (b) latent heat storage, and (c) thermochemical energy storage.

Sensible heat storage materials are mainly sorted into solid and liquid media [12]. Solid media such as rocks, concrete, fire bricks, and metals have drawn great attention due to its excellent thermal stability at high temperatures. Metallic materials [13] have high densities and excellent thermal conductivities and are ideal solid storage materials. However, the high cost is the main barrier impeding it from being widely used. Except for metallic materials, most of the other solid storage media are very low-cost and abundantly available in the market. The main drawback of them is the low thermal conductivity resulted in a low thermal charge/discharge rate during energy storage processes [14].

Liquid media including water, oils, molten salts have a much better thermal charge/discharge performance due to the convection effect of the liquid flow. Water is an excellent storage media for low-temperature (< 100 °C) TES because of its high heat capacity, heat transfer rate, moderate corrosion rate, and low cost [15]. For medium to high-temperature TES (> 200 °C), however, water is not a good candidate any more due to the extremely high containment cost caused by its huge vapor pressure. Thermal oils can be well operated at the temperature lower than 400 °C and provide excellent performance as storage media [12]. But it faces the same problem as water does for higher

temperatures. For the current CSP plants, requiring the TES application working up to 600 °C, molten salt is the most popular option as the storage media [16-19]. Molten salt, mainly the mixture of different nitrite salts, has high energy density, high heat transfer rate, low vapor pressure, and low corrosion rate. Several high-temperature TES technologies including two-tank and thermocline TES by using molten salt have been developed maturely. However, to further develop this technology in the future, the decomposition of molten salt at temperatures higher than 600 °C and the relatively high cost are the main challenges [12,14].

Latent heat storage

Latent heat storage materials are also called phase change materials (PCMs). In comparison with the sensible heat storage materials, PCMs are usually operated in a smaller temperature range, in which the materials completely undergo a solid-liquid or liquid-gas phase change process [14,20,21]. The storage capacity can be expressed in the following equation and Figure 2.1(b):

$$E_T = \int_{T_i}^{T_{ph}} mc_{p,1} dT + m\Delta h_l + \int_{T_{ph}}^{T_f} mc_{p,2} dT$$
 (2.2)

where T_{ph} is the phase change temperature, $c_{p,1}$ and $c_{p,2}$ are the specific heat of the material before and after the phase change process, respectively. Δh_l is the latent heat of the material and dominates the energy capacity of the TES system.

PCMs are generally classified into organic, inorganic and eutectic materials, as shown in ref. [10]. The organic materials including paraffin, fatty acids are mainly used in low (<100 °C) TES. Inorganic (such as ice, salts, and metals) and eutectic PCMs include more kinds of materials in a wider temperature range. For the high temperature TES applications, molten salts, salt eutectics, metals, and metal eutectics [22,23] are the potential storage materials due to their high melting temperature (> 300 cm).

°C). Hoshi et al. [24] suggested that NaNO₃, NaOH, KNO₃, KOH, LiCl, Pb, and Zn can be the competitive high-temperature storage media with high latent heat and low cost. Since the storing gasphase material is not costly-effective, the potential PCMs for TES are mostly solid-liquid materials [23]. Therefore, similar to the solid sensible heat materials. The low conductivity of solid PCMs is also a critical challenge for these technologies. Researchers have proposed several effective methods to enhance the thermal charge/discharge rate including encapsulating the storage materials [14,25], adding high-conductivity particles [26], installing fins [22], heat pipes [27], graphite foam [28], etc. However, the additional cost of the heat transfer enhancement might significantly decrease the economic profits for the whole TES system [14].

Thermochemical heat storage

As shown in Figure 2.1(c) storing heat in form of thermochemical energy through reversible reactions is also a common mode for high-temperature TES technologies [11,12,29]. The example chemical reaction equation is:

$$A + \Delta H_r \leftrightarrow B + C \tag{2.3}$$

where ΔH_r is the reaction enthalpy. During the thermal charge process, the endothermic reaction step is utilized, during when the reactant A absorbs thermal energy and decompose into reactant B and C. During the thermal discharge process, the combination reaction between B and C form the initial reactant A and releases heat. The total thermal energy stored can be expressed as:

$$E_T = n_A \Delta H_r \tag{2.4}$$

where n_A is the mole number of reactant A.

There are multiple reactants and relative reactions can be utilized for high-temperature thermochemical storage, as shown in [30]. The ammonia-based technology is the most matured one and has been investigated for over 40 years [31,32]. The calcium hydroxide system draws great

attention these years and is promising for high temperature TES [33,34]. In comparison to the sensible and latent heat storage, the emerging thermochemical TES technologies have much higher energy densities and much less heat loss at high temperatures [35]. However, most products from the thermochemical reactions are gases that can be corrosive and cause a higher containment and system cost [14]. The gaseous products also require high-pressure environment for the storage and transportation and the system is technically more complex than the sensible and latent heat storage [35].

2.2. Current TES technologies

In this section, multiple popular high-temperature TES technologies with different storage mechanisms are introduced. The results conclude the pros and cons of the current technologies and discuss the figures of merit of the TES system and storage materials.

Molten salt-based TES

Two tank molten salt TES is the current state of the art technology of high temperature TES [11,18] and has been globally utilized in the CSP applications, such as Solar Two power tower plant near Barstow in the US and Torresol Gemasolar power tower plant in the province of Seville, Spain [16,36]. As shown in Figure 2.2, a two-tank system consists of a hot tank storing the high-temperature molten salt and a cold tank holding low-temperature salt. Salt from the cold tank is heated by the collected solar thermal energy and pumped into the hot tank to store the heat. To run the power block, the high-temperature salt is pumped into the heat exchanger to transfer the heat to the heat transfer fluid (HTF) and then generate steam in the boiler. The cooled salt is accumulated at the cold tank. This technology provides a high system thermal performance (due to the forced convection of molten salt) and a high exergetic efficiency (due to the constant high temperature of the hot salt) [19].

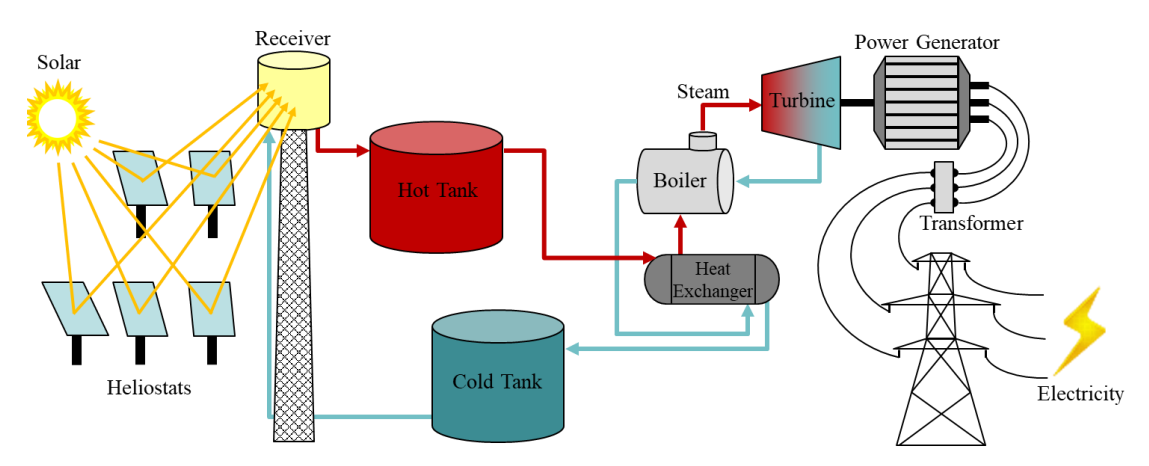


Figure 2.2. Schematic of CSP plant with two-tank molten salt TES system.

In addition to the two-tank system, the one tank thermocline system has also been proposed to significantly reduce the system cost [17,37]. The thermocline system consists of a single tank, where the hot salt accumulates at the top and the cold salt stays at the bottom due to the buoyancy force effect, as shown in Figure 2.3. A low-cost solid storage medium (sand, quartzite, etc.) can be utilized to replace part of the molten salt and act as the primary thermal storage medium [38,39]. With a great saving on storage and containment materials, the cost of thermocline molten salt-based TES can be 35% lower than the two-tank system [39,40].

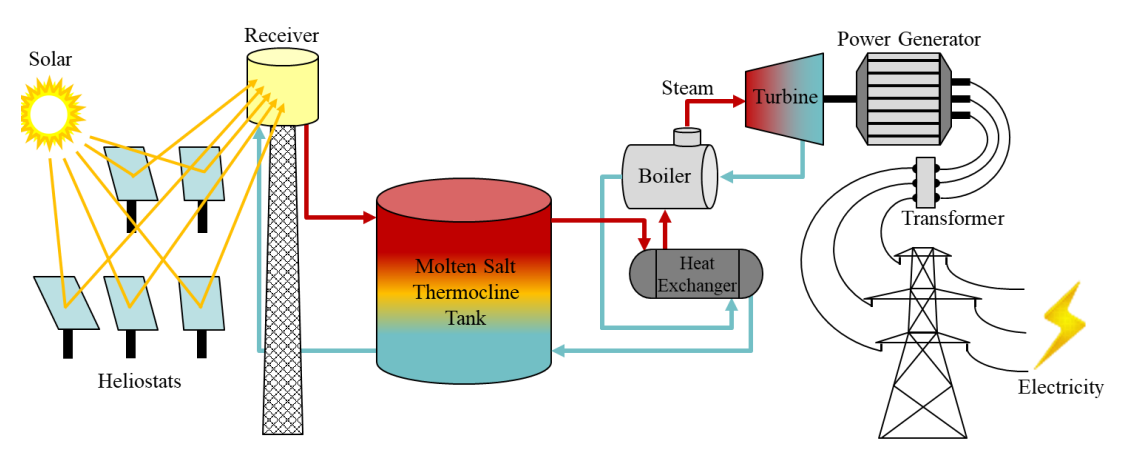


Figure 2.3. Schematic of CSP plant with thermocline molten salt TES system

The bottleneck for molten salt-based TES technologies to be qualified as the next-generation TES is the high system cost and the operating temperature range. Given the lowest price of molten salt product is around 0.45 \$/kg. The capital cost of two tank and thermocline systems are calculated to be around 31 \$ and 20 \$/kWh_t [17], respectively, which are above the US DOE SunShot goal (15 \$/kWh_t) [41]. Moreover, the common salt products (mixture of KNO₃, NaNO₃, etc.) freezes at around 200 °C and decompose at 600 °C [16], critically limits the technology to be used at low-temperature condition and future higher-temperature (> 600 °C) applications, such as CSP plant operated with sCO₂ Brayton cycle [42].

Solid-state TES

Solid materials such as rocks, concrete, sand, metals, etc. can also be used as sensible heat storage materials. Except for the metal material, most solid storage media have a lower cost and wider operating temperature range than the molten salt and therefore are promising materials for low-cost and high temperature TES [11,14].

Concrete-based TES technology has been successfully demonstrated and operated with the parabolic trough power plants by Laing et al. [43]. The system consists of the bulk of storage concrete and tubes for transporting the thermal oil (heat transfer fluid). The system can be operated up to 400 °C and stored around 300 kWh thermal energy in a 6h-charge and 6-h discharge cycle. The most significant challenge for concrete-based TES is the low thermal conductivity of the storage material. This drawback results in weak system thermal performance and therefore requires longer charge time, larger system design capacity, or more metal materials to enhance the heat transfer, which will increase the system cost. Laing et al have estimated the cost for concrete-based TES at 1GWh scale is around 38\$/kWh. A project proposed from ENERGIE Program in European Commission proposed the

cost target for next-generation concrete-based technology is around 26 \$/kWh[12], which is still higher than the SunShot cost goal.

Rock-bed based TES has also been investigated by multiple researchers. Meier et al [44] proposed the design of high temperature TES with rock-bed as the storage medium and air as heat transfer fluid in 1991. Zanganeh et al. [45] have demonstrated this technology in pilot-scale with 6.5 MWh stored thermal energy and highest operating temperature >600 °C as shown in Figure 2.4. The pebbles with an equivalent sphere diameter of 2-3 cm are used as storage medium. Air is flowed from top or bottom to thermally charge or discharge the system, respectively. Similar to the concrete, the thermal conductivity of rock is also very low and causes the poor thermal performance of the whole TES system. Instead of installing the heat transfer enhancement features, such as fine pipes and fins, Zanganeh et al. designed and manufactured the TES system with a much larger storage capacity than it needed in the CSP plant to increase the heat transfer area between the heat transfer fluid and the rocks. In a 6-hour thermal charge cycle, the system can only be charged to around 10% of the total capacity but with more than 95% charge and exergetic efficiency. The shortcoming for this design can be the high cost and high heat loss caused by the oversized TES system.

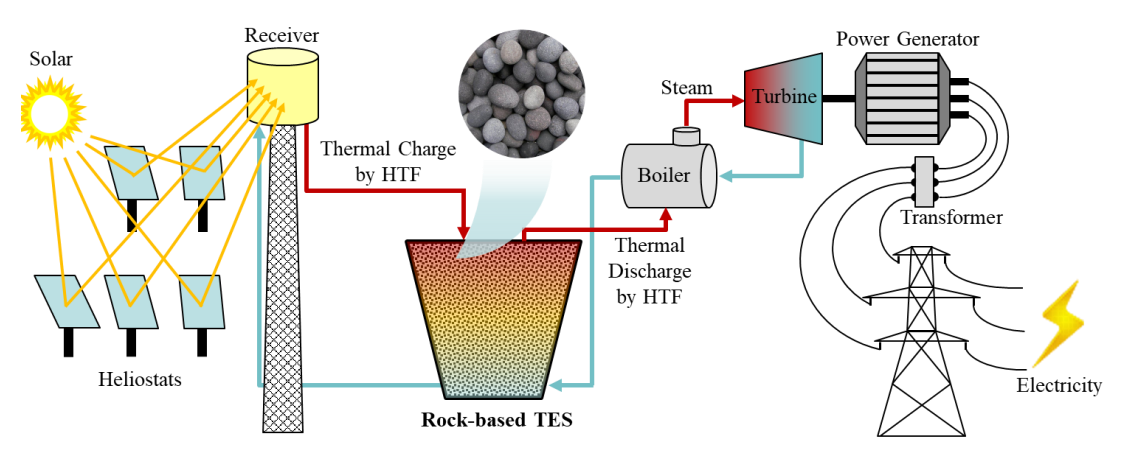


Figure 2.4. Schematic of CSP plant with a rock-based TES system.

PCM-based TES

So far, very few PCM systems have been commercialized for the high-temperature industrial application (such as CSP plants) yet [11,14]. But numerous research projects have developed promising technologies for the latent heat thermal energy storage (LHTES). As discussed in section 2.1, heat transfer enhancement plays a critical role in LHTES and therefore different enhancement methods characterize the technologies with different system configurations, including encapsulated (Figure 2.5 (a)) and shell-and-tube LHTES (Figure 2.5 (b)).

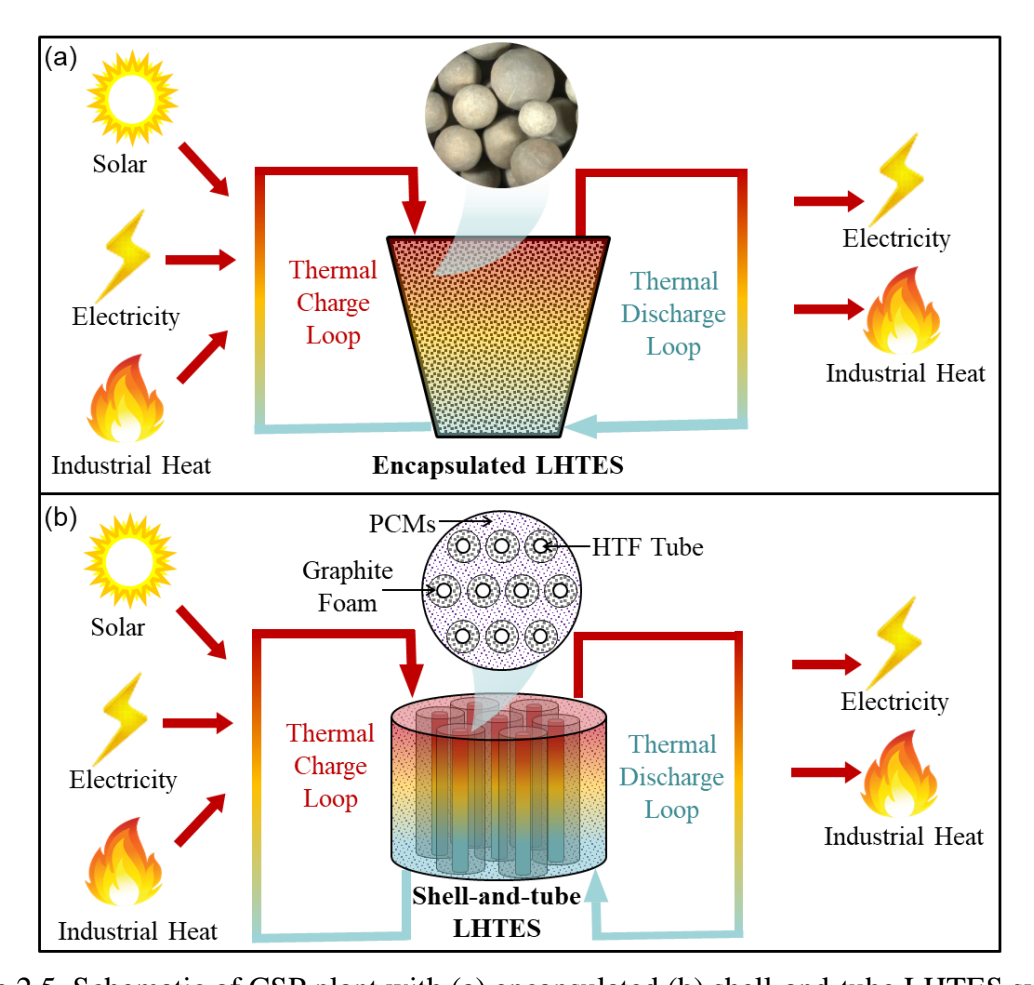


Figure 2.5. Schematic of CSP plant with (a) encapsulated (b) shell-and-tube LHTES system.

Encapsulated LHTES effectively reduces the thermal resistances of solid PCMs by incorporating the PCMs in small capsules to significantly increase the contact area between the HTF and the solid

materials [25]. The capsule layer is usually made of a mixture of high-temperature organic materials, such as Hydroxypropyl Cellulose (HPC), Hydroxypropyl Methyl Cellulose (HPMC), etc., and inorganic materials, such as clay, silica, etc. [46]. The PCM capsules can be stored in large tanks with the HTF vertically flowing through to thermally charge or discharge the system with a stable thermal stratification. Due to the large energy density and the enhanced heat transfer rate, the overall performance of the encapsulated LHTES system can be potentially comparable or even better than the molten-salt system. The system cost is mainly dominated by the PCM and encapsulation material cost and Nithyanandam et al. have analyzed the capital cost of the large capsulated LHTES in scale of over 1 GWh can be 13-17 \$/kWh_t [47].

In shell-and-tube LHTES, the bulk of PCMs is stored in a large shell with multiple fine HTF tubes installed within the shell [20]. The thermal performance of the system can be enhanced by increasing the tube outer surface area (increasing the length, number of tubes), embedding the tubes with heat pipes [27], or embedding the high-conductive packed bed, such as graphite foam [28]. The latter two methods were found to be more effective and are promising for future LHTES. With a huge thermal conductivity, heat pipes can greatly enhance the thermal response rate of LHTES system. The main challenge of this technology is the high cost of the heat pipe. Nithyanandam et al. have analyzed the capital cost of the large capsulated LHTES in scale of over 1 GWh can be 21-30 \$/kWh₁ [47]. Recently, researchers in Argonne National Laboratory have developed high-temperature LHTES system embedded with graphite foam to enhance the thermal performance [28,48,49], as shown in Figure 2.5 (b). The system is also of shell-and-tube configuration and the graphite foam is installed around the HTF tube. By using the chlorate such as MgCl₂ as the PCMs, the system is capable to work up to 610 °C and can provide the exergetic efficiency higher than 97%. The use of graphite foam can help decrease the HTF tubes by a factor of eight. Given the relatively low cost of graphite foam, the technology brings a significant cost reduction for shell-and-tube LHTES. However, more system-level

cost analyses are required to prove LHTES with graphite foam can be a competitive low-cost solution among all sensible heat, latent heat, and thermochemical heat TES technologies.

Thermochemical TES

Thermochemical energy storage (TCES), with the advantage of high energy density, is of the interest by more and more researchers [50]. Ammonia-based TCES is one of the most matured technologies in this field [31,32]. Ammonia is dissociated endothermically to nitrogen (N2) and hydrogen (H₂) and can be unitized to store solar thermal energy. Lavine et al [51-53] have proposed the design for the ammonia-TCES, which can economically operate at the CSP applications based on the supercritical stream cycle (Rankine cycle) at 650 °C, as shown in Figure 2.6. The thermal energy from solar field is stored through the ammonia dissociation reaction in endothermic reactor and is recovered by ammonia synthesis reaction in exothermic reactor to drive the power generator. Liquid ammonia and gaseous products can be stored in salt caverns or shaft drilling undergrounds and separated by chilled separator. Ammonia is transported in gaseous phase by a gas compressor and the heat exchangers are required to utilize the waste heat from both reactions. This ammonia-based system has such positive features as no side reaction, inexpensive reactants, and easy separation between the reactants and productions. In addition, since the gaseous reactants and products for exothermic reactions can be easily transported, the exothermic reactor can be installed in the power block to replace the steam boiler, which can help decrease the total cost for CSP plant. In comparison to the other TES technologies, the main challenges for this system are the high pressure caused by the gaseous products in the system and high risk of operation safety. The complexity of the system can also result in a high capital cost.

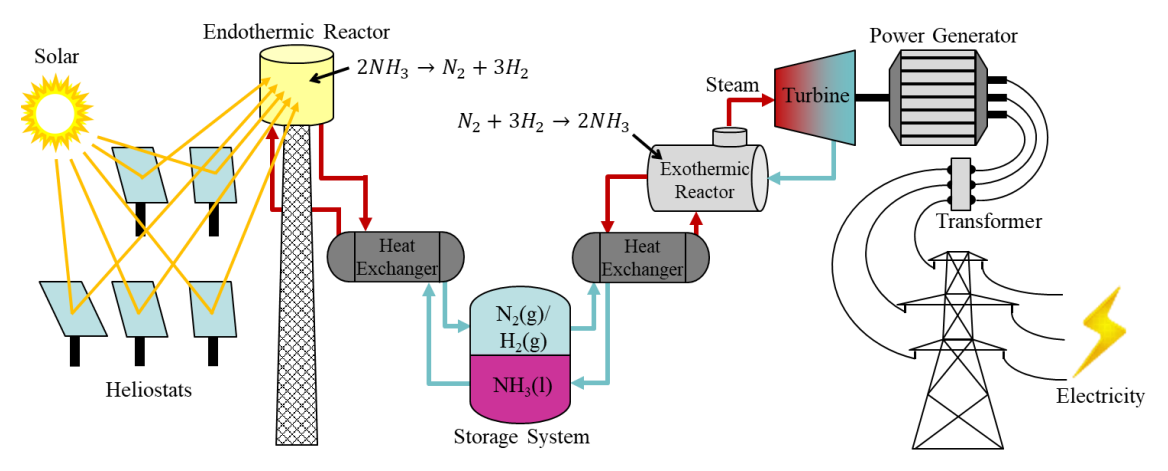


Figure 2.6. Schematic of CSP plant with ammonia-based thermochemical storage system

2.3. Figures of merit for TES system

For energy storage applications, the main functional requirements are to store/retrieve energy in high charge/discharge rate, high efficiency, high quality, and low storage cost. Since energy is stored in form of thermal heat in TES system, system thermal performance, dominating the charge/discharge rate, becomes a primary techno-economic metric. Exergetic efficiency, defined as the ratio between output and input exergy for TES system (as shown in Equation (2.5)), is commonly used to quantify system energy efficiency and quality simultaneously. Therefore, to evaluate a TES system, storage cost, exergetic efficiency, and system thermal performance are the main figures of merit. Therefore, the US department of energy has proposed the cost and performance target for the TES technologies in CSP application (SunShot goal) as 15 \$/kWh_t and > 95% exergetic efficiency by 2020 [41].

$$\varepsilon = \frac{\Xi_{out}}{\Xi_{in}} \approx \frac{Q_{out} \left(1 - \frac{T_{\infty}}{T_{out}}\right)}{Q_{in} \left(1 - \frac{T_{\infty}}{T_{in}}\right)}$$
(2.5)

Among different TES technologies, these metrics are mainly governed by multiple properties of storage material. The cost of TES is mainly affected by the storage medium and containment material cost and the latter usually depends on corrosivity, operating pressure, and temperature of the former.

The energy density of the storage medium can also more or less affect the storage cost, since the system footprint, thermal losses, and cost of containment materials decreases with it. As shown in Equation (2.5), with the given input parameters, system exergetic efficient increases with the output energy and temperature. For a well-designed TES system, the output energy can usually be close to the input energy and system output temperature is limited by the thermal stability of storage material. For most current TES technologies, system thermal performance depends most likely on the heat transfer rate of the storage material. Therefore, a promising storage material should have following properties: low cost, low operating pressure, good material compatibility, good thermal stability, high energy density, and high heat transfer rate.

2.4. Characteristics of sulfur as a storage medium

In this section, I am going to introduce the physical and chemical nature of sulfur and explain why sulfur can be a promising lost-cost and high-temperature storage medium. In addition, more characteristics of sulfur including the necessary properties and the material compatibility performance are also discussed.

The nature of sulfur

Sulfur is abundantly reserved as elemental sulfur and sulfur compounds on our planet. Most elemental sulfur is produced as a byproduct from petroleum process industry, such as heavy crude oil desulfurization, and the production should be adequate for the foreseeable future. Other supplies of elemental sulfur including natural mineral deposit and metallurgical industry are also quite sufficient and stable. Therefore, elemental sulfur is dirt cheap on market and its cost is as low as 0.04\$-0.11\$/kg [5]. At room temperature, elemental sulfur is at solid-state and in a powered or block form. It melts at around 113 to 119 °C and vaporizes at around 445 °C under atmospheric pressure [54]. As an element, sulfur has very good thermal stability and does not decompose at high temperatures.

Sulfur crystallizes into two main forms: rhombic sulfur (S_{α}) and monoclinic sulfur (S_{β}) . Both crystalline sulfur is composed of one sulfur allotrope, S_{λ} , which is the only stable allotrope of sulfur at solid-state. At the temperature below 96 °C, S_{α} is stable and S_{β} changes to S_{α} gradually. At the temperature between 96 and 119 °C, S_{β} is stable and the other allotropes slowly change into this form. S_{α} and S_{β} melt at around 113 and 119 °C, respectively. After solid sulfur melts, small amount of liquid sulfur changes to another allotrope, S_{π} , which has a lower melting point. Therefore, molten sulfur solidifies at around 115 °C.

There are mainly three allotropes, S_{λ} , S_{π} , and S_{μ} , existing in liquid sulfur. As the temperature increases, the concentration of S_{λ} decreases from 97% to 59% at the boiling point and the concentration of S_{μ} increases from 0 to 37%. S_{π} is always at a low concentration, which is smaller than 7%, at the liquid state. The molecular configuration of S_{λ} is a puckered S_{8} ring and S_{μ} consists of long chains (S_{n}) of an uncertain number of sulfur atoms. Therefore, liquid sulfur changes according the equilibrium equation in Equation (2.6) with temperature increasing. The enthalpy change for the reaction among three allotropes of sulfur is around 26 kJ/kg [55] in total from around 160 °C to the boiling point, which contributes an increase of effective heat capacity of liquid sulfur.

$$\frac{n}{8}S_8(S_\lambda, \text{ring}) \xrightarrow{+\Delta H} S_n(S_\mu, \text{chain})$$
 (2.6)

The formation of the long chains of sulfur atoms can significantly increase the viscosity of liquid sulfur. Therefore, starting from 160 °C, many observations show that the sulfur viscosity increases greatly. However, at a temperature higher than the critical temperature, which is around 188 °C for 100% pure sulfur, the long chains begin to break up and therefore the viscosity decreases as the temperature rises from the critical point. By adding a small amount of foreign substance (impurities), such as hydrogen sulfide and halogens, the viscosity of sulfur will markedly drop for all temperatures.

This phenomenon is likely to be caused by that the foreign atoms replace some of sulfur atoms and breaks up the long chains. All the discussed chemical reaction in liquid sulfur has been shown in Figure 2.7.

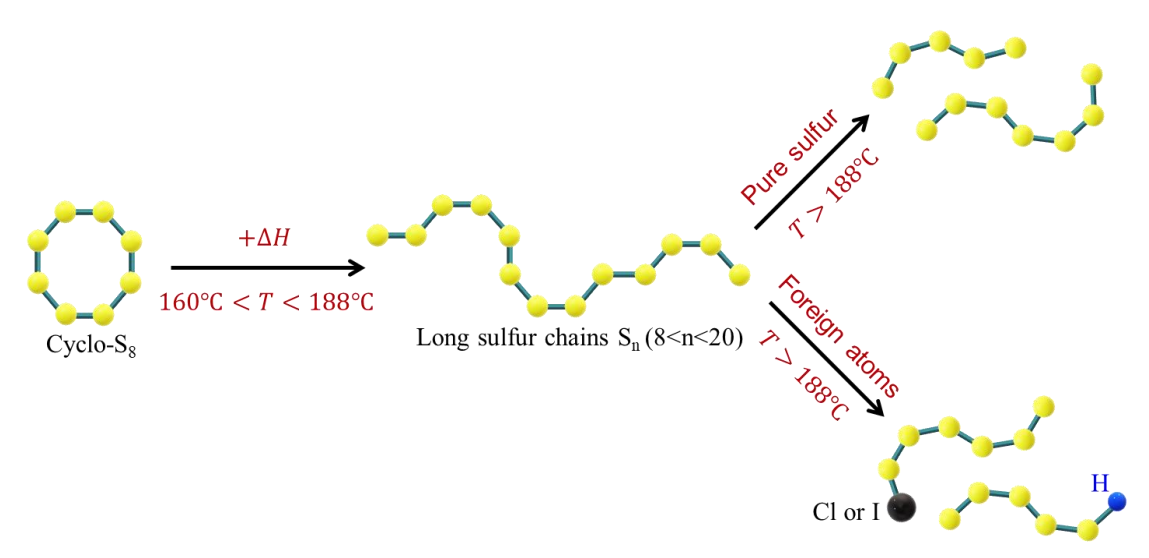


Figure 2.7. The chemical reaction of liquid sulfur from 119 to 445 °C.

In addition to the temperature and the purity, the sulfur viscosity is also affected by the pressure [56]. High pressure will favor long chains against short chains and S₈ rings since the long chains have the lowest volume (highest density). Therefore, the viscosity of liquid sulfur increases with pressure. Under isochoric conditions (in closed system), system pressure gradually increases with the temperature due to the expansion and the vaporization of sulfur. Thus, the sulfur viscosity in closed system will be higher in open system at high temperatures close to boiling point. Figure 2.8 shows the viscosity for pure sulfur in open system [57], the impure sulfur (with 0.4% impurities) in open system [58,59], and the impure sulfur in closed system [58].

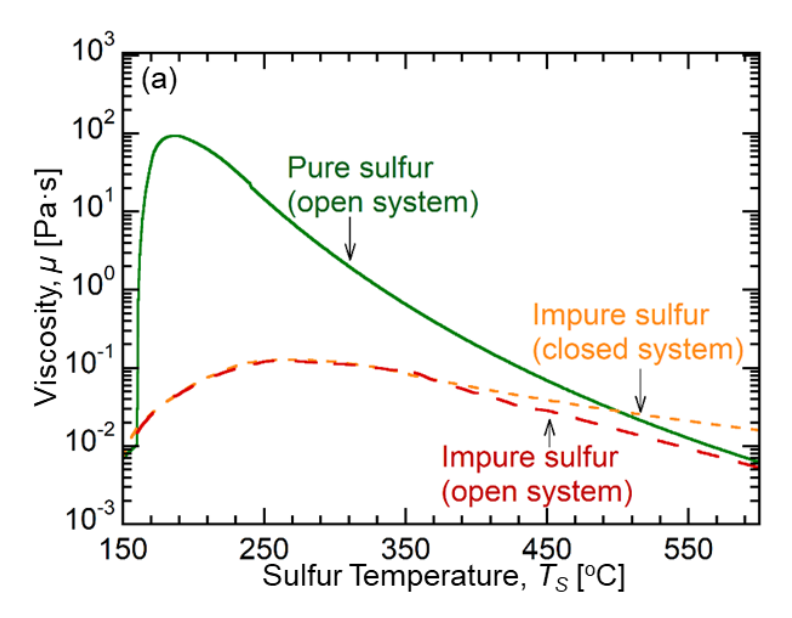


Figure 2.8. The viscosity of pure sulfur in an open system [57], impure sulfur in an open system [58,59], and impure sulfur in a closed system [58].

Sulfur vaporizes at around 445 °C under atmospheric pressure. Gaseous sulfur consists of a mixture of S_8 , S_7 to S_2 and all the allotropes will change into S_2 by 1000 °C endothermically, as shown in the following equation and Figure 2.9 [6].

$$S_n \xrightarrow{+\Delta H} \frac{n}{2} S_2 \tag{2.7}$$

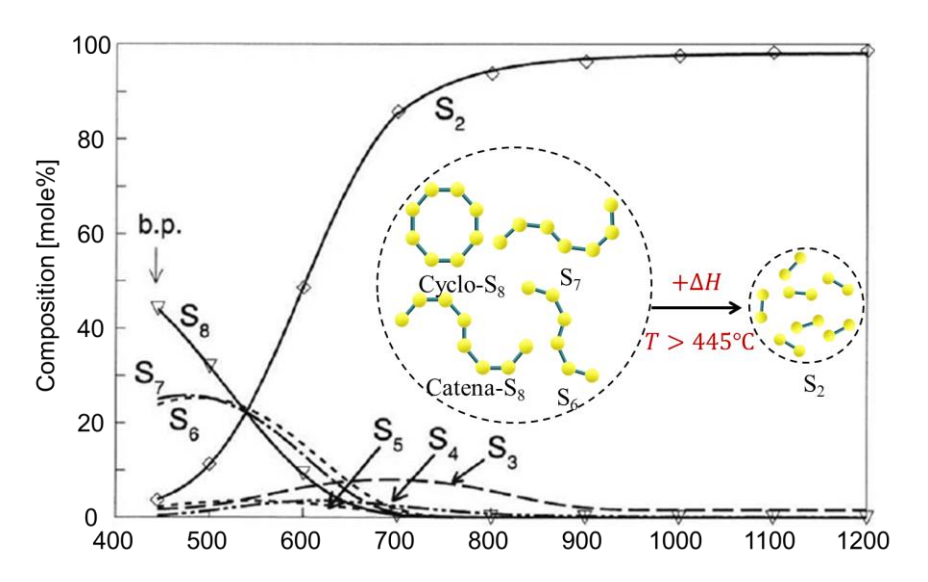


Figure 2.9. The chemical reaction of gaseous sulfur (adapted from ref. [6]).

The enthalpy increase, ΔH , for this reaction is around 1617 kJ/kg, which is comparative to many reversible chemical reactions used in current thermochemical energy storage technologies. Therefore, vapor sulfur can potentially be a very good thermochemical storage material for future ultra-high temperature (1000 °C) TES.

From another point of view, liquid sulfur with moderate energy density, but high thermal stability and low cost, can be a promising candidate for sensible heat storage media. The saturated vapor pressure of sulfur at 600 °C is around 6.44 atm, which indicates sulfur can be held at liquid state in an isochoric container with a sulfur vapor pressure higher 6.44 atm from around 120 to 600 °C. For higher temperature at 650 °C, the saturated vapor pressure is around 10 atm [54]. The pressure requirement is quite moderate and will not be a challenge for the common-used metal containers. Therefore, Wirz, et al. [7] proposed elemental sulfur as a thermal storage medium for medium to high-temperature thermal storage applications.

Properties and a preliminary study for isochoric condition

Storing sulfur in isochoric containers can naturally achieve the saturated vapor pressure to main sulfur at liquid state for high-temperature (600 °C) TES system. Shows the necessary properties of liquid sulfur under the isochoric condition from 120 to around 650 °C. The density data for saturated liquid sulfur were obtained by West [60]., as shown in Figure 2.10(a). Lewis et al [61] measured and derived heat capacity for liquid sulfur up to 420 °C, which is shown by solid line and markers in Figure 2.10(b). The heat capacity data for the temperature higher than 420 °C were extrapolated linearly based the given data (dash line in Figure 2.10(b)). There is a sharp hump on heat capacity curve between around 160 and 250 °C, which is caused by the reaction among S_{λ} , S_{μ} , and S_{π} . The average heat capacity is around 1.16 kJ/kg·K, which is around 77% of it for molten salt. But considering the much wider operating temperature range, the energy density for liquid sulfur TES is higher than the molten

salt-based system. Figure 2.10(c) shows the thermal conductivity was obtained and extrapolated from the experimental study by El-sharkawy and Dessoudy [62] in 1983. Sulfur viscosity is significantly affected by the temperature, the pressure, and the concentration of impurities. Bacon and Fanelli [57] have measured viscosities of pure sulfur in open system (solid line and round markers in green) and of impure sulfur with different purities in closed system (data for impure sulfur with 0.4% impurities is shown in red solid line with triangle markers). Given the 0.4% concentration of impurities is quite small, the commercially available sulfur (the purity is usually claimed to be 99%) is likely to have a similar grade. The results also indicated that (1) Effect of pressure (caused by the closed system) is not significant at temperature lower than 300 °C (2) at temperature higher than 300 °C, the logarithm of viscosity decreases with logarithm of temperature linearly. (3) for all impure sulfur in closed system, the extrapolated viscosity at 1000 °C is around 0.003 Pa·s and it is reasonable to assume that the viscosity of pure sulfur also decreased to this value at 1000 °C. Therefore, the viscosity for pure sulfur in closed system [58] at the temperature higher than 300 °C was extrapolated as the dash green line in Figure 2.10(d). The later sections in this dissertation will discuss the comparison between the experimental and computational results by using pure sulfur and impure sulfur viscosities.

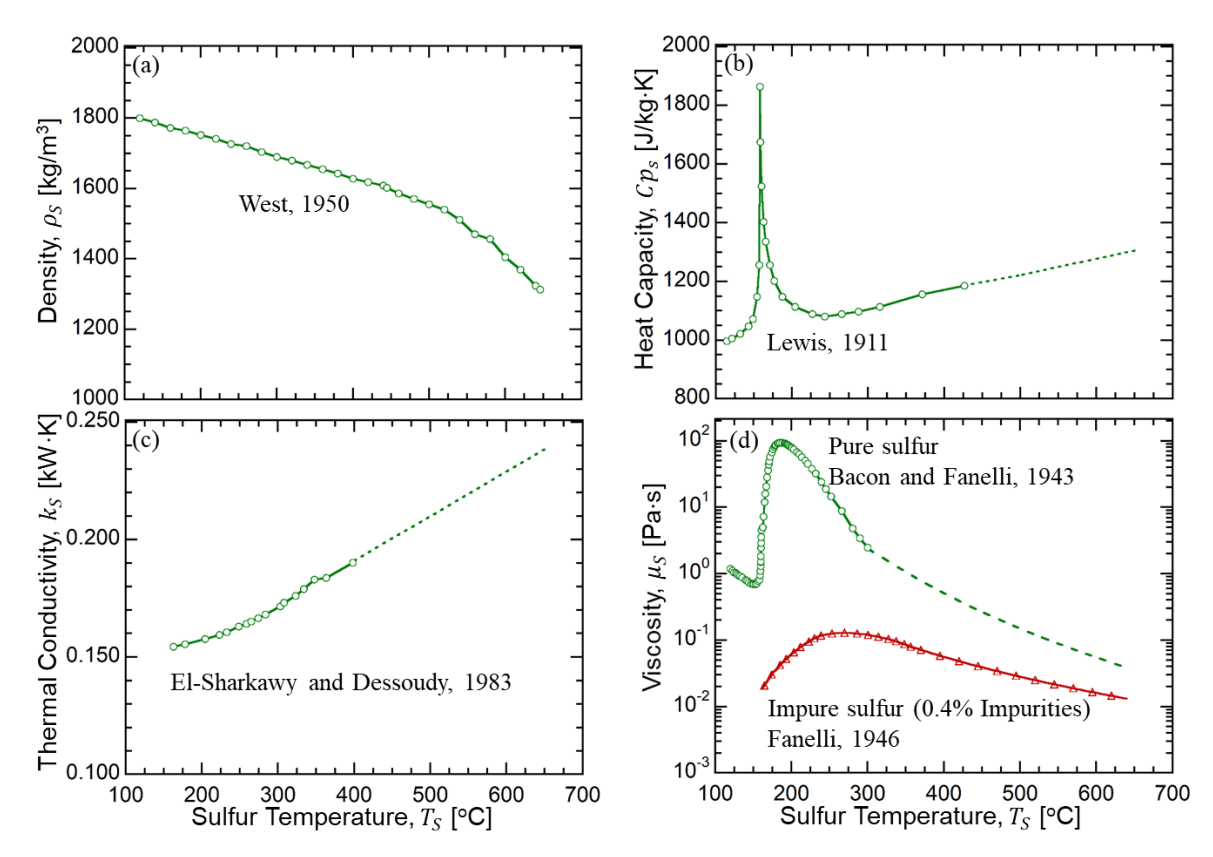


Figure 2.10. Sulfur properties in isochoric system: (a) Density, (b) heat capacity, (c) thermal conductivity, and (d) viscosity.

UCLA energy innovation lab conducted a material compatibility study [8,9] to investigate the corrosion rate of sulfur with three potential containment materials or SulfurTES, namely Stainless Steel (SS) 304, SS 316, and Inconel. Three tubes of each material were thermally cycled to 500 °C for 100, 600, and 900 hours and to 600 °C for 100 hours. The tube samples were then completely cleaned up with CS₂ solvent to remove the sulfur residuals on tube inner surface. Scanning Electron Microscope (SEM) Nova230 was used to visualize the cross-section of the sulfur tube and provide the wall thickness measurement before and after the tests to determine the amount of tube wall materials reacting with sulfur, as shown in Figure 2.11(a). Figure 2.11(b) shows the measurement results for 500 °C tests. The rapid decrease of wall thickness for SS 304 tube indicates the material is quite corrosive with sulfur. However, for SS 316 and Inconel tubes, the thickness of tube increased

after each test period because the sulfide layers formed. Given the sulfide is firm and dense, this phenomenon can be regarded as protection of material from being corroded by sulfur. Therefore, both SS 316 and Inconel can be used as containment materials for SulfurTES due to their high corrosion resistance. In consideration of the material cost, SS 316, with a moderate cost of around 1-2 \$/kg, is the best candidate for containment of sulfur.

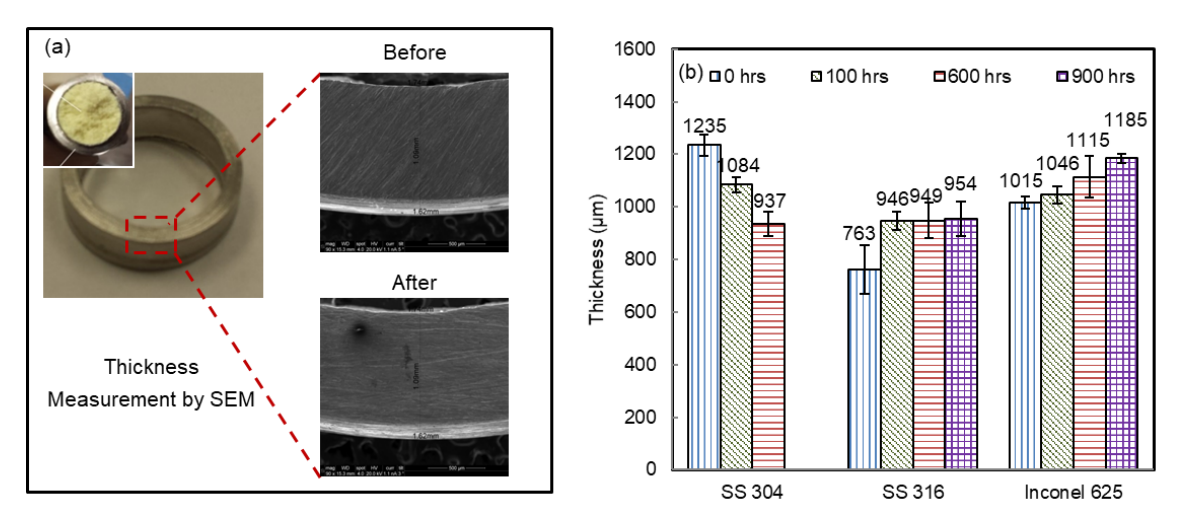


Figure 2.11. Thickness measurements for the sulfur tubes of various containment materials before and after the multiple thermal tests. (a) SEM pictures, (b) measurement results.

Further containment study was conducted to determine the lifetime for the tube-shape container under day-by-day thermal cycles between 200 to 600 °C. Naik [63] has investigated the SS 316 tube of various loading fraction (20 to 80%), diameter (2 to 8 inches), and thickness (Sch5 to 40). The experimental results show that, after several conditioning cycles, the maximum pressure within the tube with an 80% loading fraction is around 200 psi, which is quite moderate for SS 316 containers. The potential failure analyses proved that the container with a very thin wall thickness (Sch 5) can survive for over 40-year charge (600 °C) and discharge (200 °C) operation against creep deformation, thermal shock, and metal fatigue.

Wang [64] has conducted a preliminary analysis for the main cost in SulfurTES system and it is compared with the other TES technologies [40,45,47,65], as shown in Figure 2.12. It can be observed that SulfurTES has apparently more potentials to fulfill the 2020 SunShot cost goal.

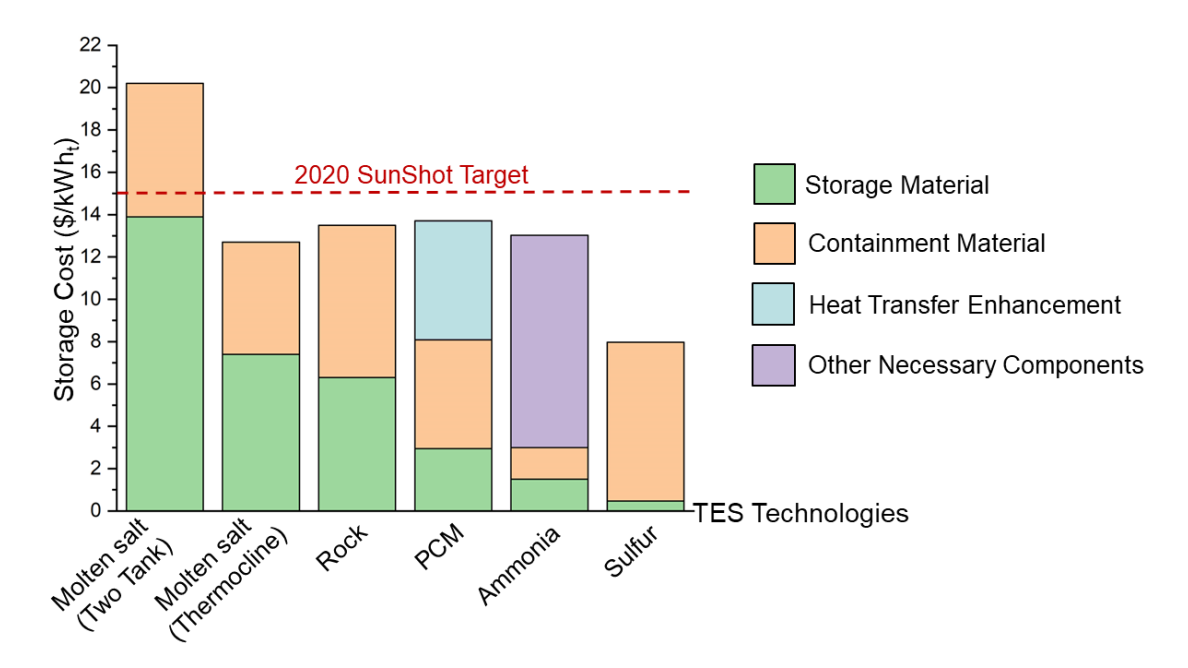


Figure 2.12. Preliminary analysis for the storage cost of competitive TES technologies.

2.5. Design of SulfurTES system

As a sensible heat TES, operating liquid sulfur in two-tank or thermocline systems as molten-salt-based TES is a potential option for SulfurTES system design. However, the particular challenges including maintaining the system pressure, pumping sulfur at high temperatures exist in the liquid-sulfur system and can cause a significant increase in system cost or safety risk.

Therefore, the UCLA Energy Innovation lab proposed design of SulfurTES system in thermal battery configurations [8,9]. For this TES system, sulfur is isochorically stored in multiple sealed tubes enclosed in a shell-and-tube heat exchanger system, as shown in Figure 2.13(a). Heat transfer fluid is pumped into the system to thermally charge or discharge the sulfur storage tubes. Heat transfer performance of sulfur in these isochoric tubes plays a critical role in system thermal performance.

Nithyanandam et al. [66-68] and Barde et al. [69] investigated the sulfur heat transfer behavior in horizontally-oriented sulfur-filled tubes (as shown in Figure 2.13 (a)) of various configurations and dimensions. In the horizontal orientation, the natural convection in the cross-section plane dominates the heat transfer between the tube wall and the sulfur, yielding an attractive thermal charge rate. A 10-kWh SulfurTES thermal battery system with horizontally-oriented tubes was developed to study the system-level performance, as shown in Figure 2.13 [70]. The experimental results show that this labscale SulfurTES system has high energy density (around 255 kWh/m³) and attractive thermal performance. In addition to this lab-scale SulfurTES prototype, a pilot-scale SulfurTES system has been set up, integrated with a concentrated solar power (CSP) dish system (shown in Figure 2.13(c)) [9]. In this demonstration, solar thermal energy was efficiently collected by the CSP system and transported it to our SulfurTES system through the solar receiver and the air charge conduits. The maximum energy storage capacity for this system is > 30kWh, which meets the storage target of the project EPC-14-003 by California Energy Commission (CEC). More details can be found in Appendix B.

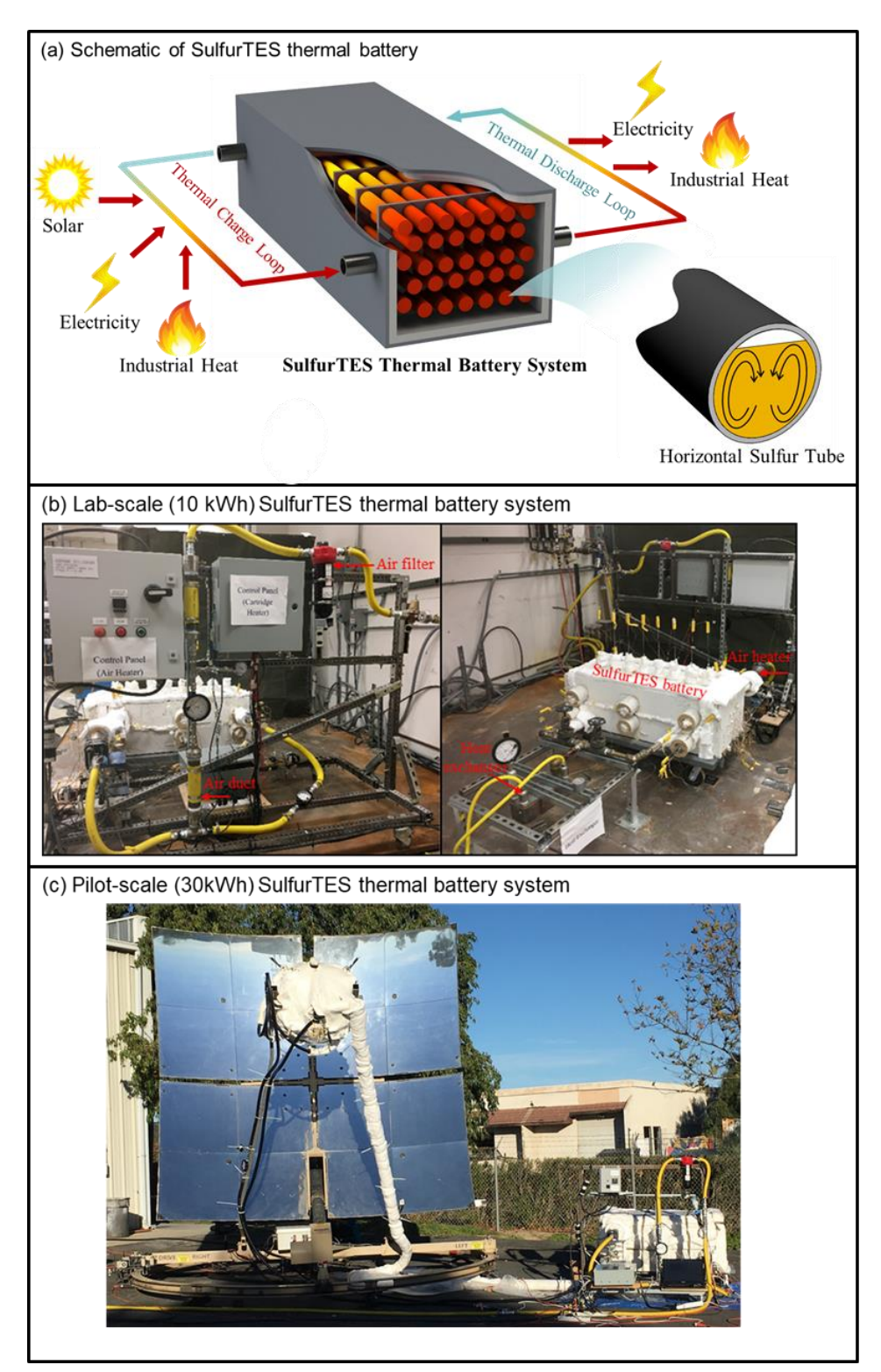


Figure 2.13. (a) Schematic of SulfurTES thermal battery system in horizontal-tube configuration. (b)The lab-scale and (c) the pilot-scale demonstration of the SulfurTES thermal battery system.

Compared with the horizontal tube configuration, orienting the sulfur-filled tube vertically (as shown in Figure 2.14(a)) can significantly affect the heat transfer behavior because the characteristic length is the tube length, instead of the tube diameter. Lakeh, et al. [71] showed that heat transfer performance of supercritical CO2 (sCO2) stored in a vertical container with an aspect ratio of 3.57 or higher, is superior as compared to the same container in the horizontal orientation, with $\sim 20\%$ lower thermal charge period. In addition, the vertical configuration potentially brings more benefits for the TES system, such as compact footprint, lower cost, thermocline behavior, simplified loading, and ease of operation and maintenance. For the vertical tube configuration, the thermal charge direction has a critical impact on the heat transfer and storage behavior. Theoretically, when a storage tube is thermally charged from top to bottom, an axial thermocline will form and be held within the sulfur due to the buoyancy effect. Therefore, it is safe to assume the sulfur will have a higher exergy charge rate compared to either charging the tube uniformly in a vertical orientation [72,73] or charging the tube in a horizontal orientation. When the tube is charged uniformly or from bottom to top, the buoyancy effect will cause a strong mixing between the hot and cold sulfur, potentially yielding higher heat transfer rates. The heat transfer behavior under uniform charge/discharge condition is discussed in Chapter 3, and the effect of charge/discharge direction is investigated in Chapter 4.

In addition to thermal battery (tube-configuration) system, where sulfur is sealed in the tubes and HTF flows within the shell, we can design the system in a revised way, in which the sulfur is stored in the shell and HTF flows through the tubes, as shown in Figure 2.14(b). The system is named as SulfurTES bath system, where the charge tubes are installed at the bottom of system to continuously heat the cold sulfur by utilizing the buoyancy-driven flow. Symmetrically, the discharge tubes are implemented at the top. Due to the large temperature difference between the tube wall and the sulfur, this SulfurTES bath system could have a superior heat transfer rate and therefore greatly decrease the overall containment cost, in comparison to the tube-configuration system. To obtain more

quantitative proof of this expectation and provide the necessary design bases, we conducted a computational study of the sulfur heat transfer behavior in SulfurTES bath system and more details are discussed in Chapter 5.

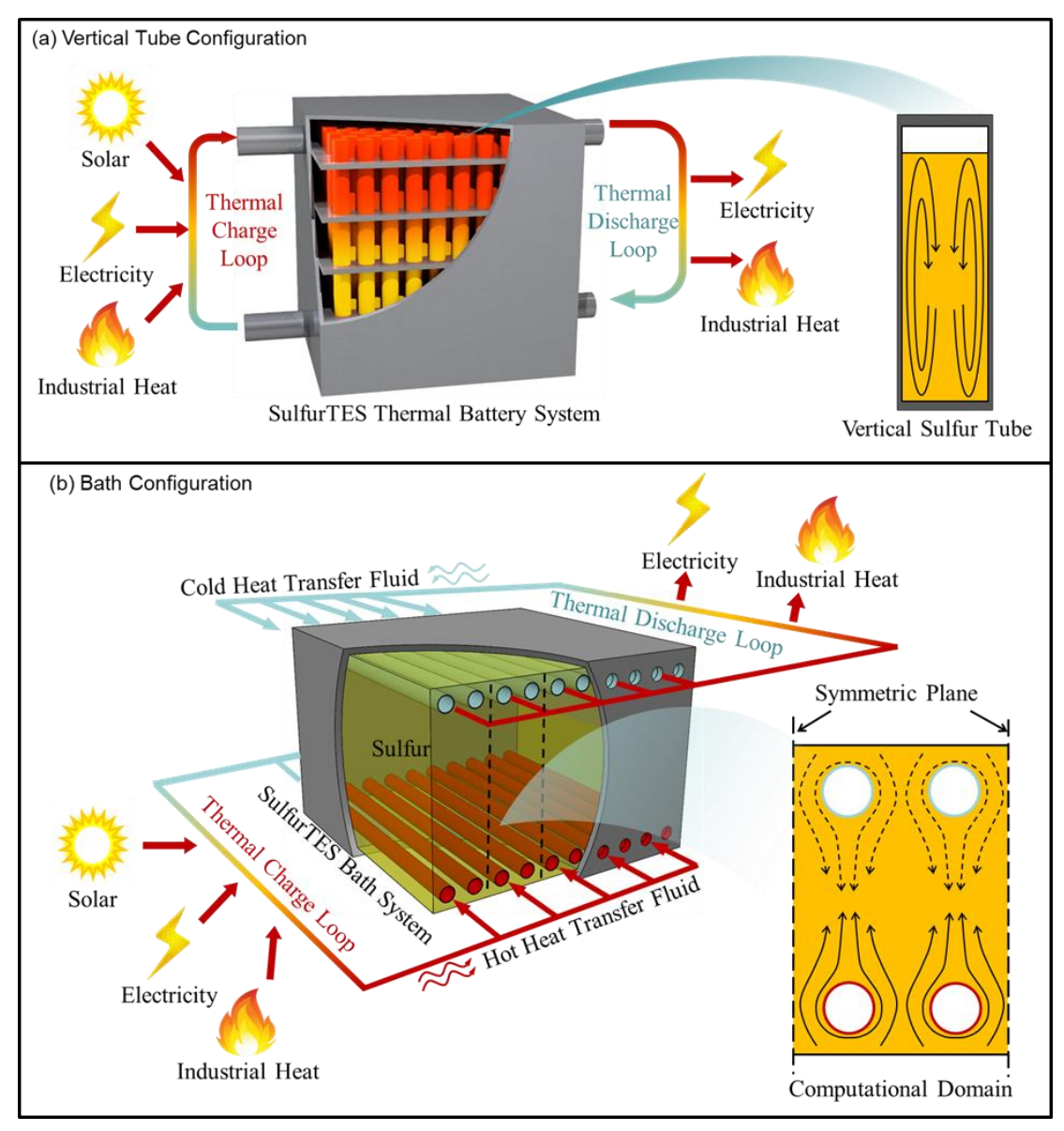


Figure 2.14. Schematic of SulfurTES system in (a) vertical tube configuration and (b)bath configuration.

Chapter 3 Sulfur heat transfer in vertical tubes with uniform charge and discharge

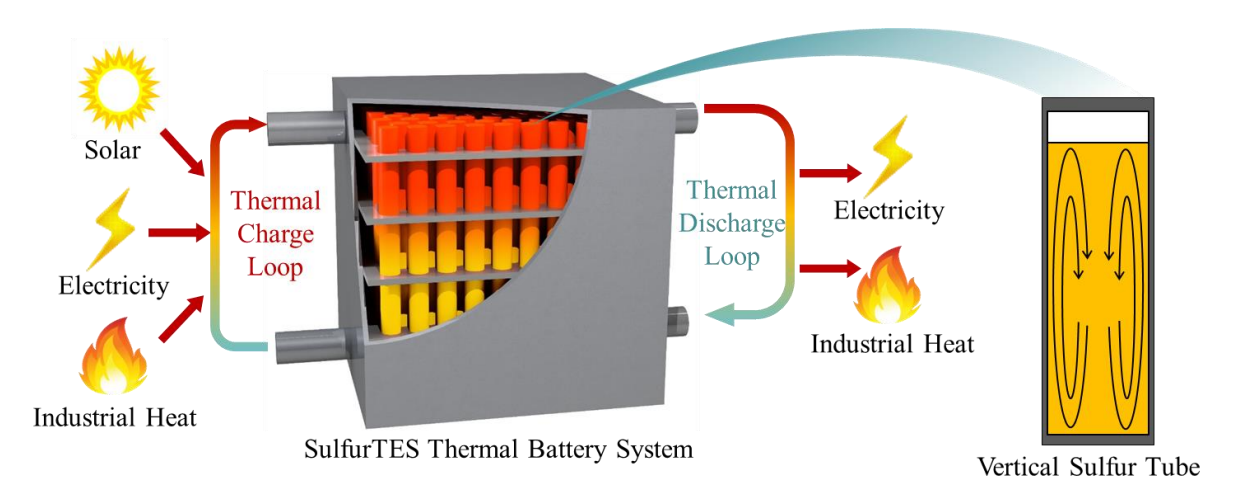


Figure 3.1. Schematic of the SulfurTES thermal battery system with vertically-oriented tubes.

The objective of this effort is to investigate the heat transfer behavior of sulfur isochorically stored in a vertically oriented steel tube in the temperature range of 25 to 600 °C. For the experimental analysis, the system was uniformly heated from 25 to 600 °C to study the effect of solid-liquid phase change and viscosity variation on the sulfur heat transfer behavior. We developed a computational model to further investigate the sulfur heat transfer behavior from 200 °C to 600 °C. With the computational model, Nusselt number correlations for sulfur heat transfer in a vertical tube were developed. The thermal performance was assessed based on thermal charge period, thermal charge rate, and the heat transfer coefficient, and compared with the results reported by Nithyanandam et al. [66] for the horizontal tube configuration. This is a first of its kind study revealing a unique heat transfer behavior of sulfur in a vertical configuration that must be further explored for its application in the real-world SulfurTES system development.

3.1. Experimental study

3.1.1. Experimental system

Figure 3.2 shows the picture and schematics of the experimental facility developed to study the heat transfer performance of sulfur isochorically stored in a vertical container. The container was comprised of a 6.03 cm (2" NPS) O.D., Sch. 10, 1m long SS316 tube, sealed by 1.27 cm (0.5") thick caps at either end, similar to the steel tube used for sulfur heat transfer study in horizontal configuration [66-70]. Three instrumentation tubes were welded to each end cap that provides access to the sulfur thermocouples and the pressure gauge. The total mass of sulfur in this system was 3.37 kg and corresponds to ~80% volumetric loading fraction of sulfur. As shown in Figure 3.2(b), the void section of the tube is filled with argon to maintain an inert environment during thermal cycling, preventing the sulfur from burning or contamination.

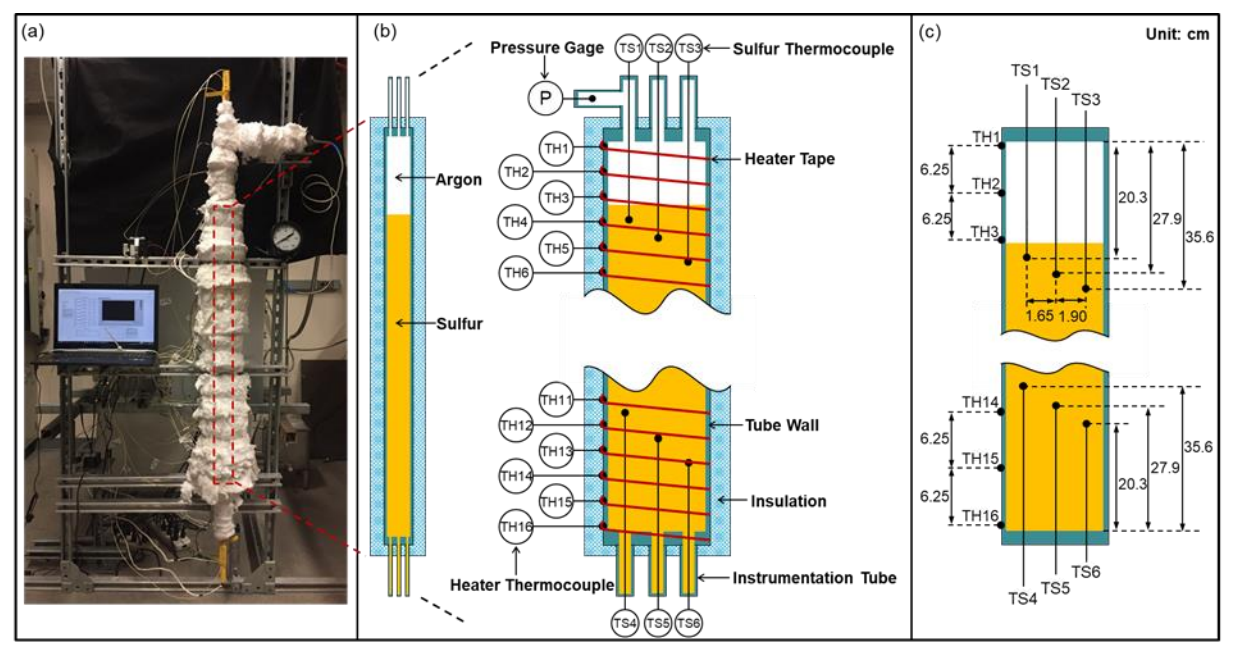


Figure 3.2. (a) Picture, and (b) schematic of the experimental facility. (c) Schematic of the instrumentations

Eight heater tapes (120V, 312W) were wrapped around the steel tube to achieve the required temperature distribution along the tube surface during the charging process. The power input to each heater tape was controlled by the PID controller for the safe and effective thermal charging process. Sixteen K type thermocouples (TH1-TH16), equispaced along the tube surface, were used to measure the tube temperatures. Moreover, six K-types thermocouples were installed through the instrumentation tubes to measure the sulfur temperature at the select axial and radial positions. The locations of all thermocouples are shown in Figure 3.2(c).

A pressure gage was installed at the top of the steel tube through one of the instrumentation tubes to monitor system pressure during the experiments. The connection to the pressure gauge was maintained at 200 °C (> 114 °C, the melting point of sulfur) with the help of an independent heater to prevent clogging of this connection due to sulfur solidification.

The heat transfer behavior of sulfur was studied in two distinct temperature ranges: ~50-200 °C, and 200-600 °C. In the first stage of thermal charging, the tube surface was uniformly heated to 200 °C, and sulfur temperatures were recorded until the steady-state was achieved. In the second stage, the tube surface was heated to 600 °C at a controlled ramp rate, and again the sulfur temperatures were recorded until the system achieved a steady state. At the end of thermal charging, heaters were turned off and the system was cooled naturally to room temperature. The procedure was repeated to ensure that reliable experimental measurements were obtained.

3.1.2. Results and discussions

The system was operated for multiple thermal cycles using the procedures explained in section 3.1.1 to study the sulfur heat transfer behavior.

In the first stage, the system was thermally charged from room temperature to 600 °C, during which sulfur undergoes the solid-liquid phase change. The temporal sulfur temperature variation is

shown in Figure 3.3(a). It is shown that the sulfur temperature is greatly dependent upon the position of thermocouple within the steel tube. The Peripheral sulfur temperatures increased faster than core sulfur temperatures (e.g., TS1 > TS2, TS4 > TS5) because of their proximity to the heat source at the wall. Moreover, the sulfur near the wall melted first and was raised to the top section of the tube due to buoyancy-driven flow. This sulfur, in turn, preferentially heated the top region of the tube and cold sulfur descended to the bottom region of the tube. Therefore, the ramp rates of the temperatures in the top region were higher than them in the bottom region at the same radial position (e.g., TS2 > TS5, TS3 > TS6). The comparison between some sulfur temperatures, such as TS2 and TS3, does not show a specific trend due to the simultaneous effect of multiple mechanisms. For example, TS2 is located higher than TS3 and thus is exposed to hotter sulfur. However, TS3 is closer to the tube wall and thus closer to the heat source. These physical mechanisms affected the temperature ramp rate and therefore the temperature for a specific location might not be consistently higher or lower than the other locations.

As shown in Figure 3.3(a), TS4 is higher than TS1 in the beginning (t < 0.15h). However, we expected TS1 to be higher than TS4 since TS1 is positioned at the same radial location, but the higher axial location as compared to TS4. This behavior is observed due to the likely deviation of the TS4 thermocouple probe tip towards the wall. The TS4 instrumentation tube was welded to end cap at an angle that is not perfectly perpendicular to the end cap, causing its tip to slightly tilt towards the tube axis. Therefore, the tip of the thermocouple probe for TS4 was tilted towards the tube wall. Furthermore, the thermocouple probe was installed before the sulfur was loaded in the tube. The instrumentation tube for TS1, which locates right above the TS4 probe tip (as shown in Figure 3.2(b)), was also used to load molten sulfur in the steel tube. Molten sulfur falling on TS4 under gravity might have further bent the thermocouple probe towards the wall. Consequently, it is likely that the TS4 probe tip is actually closer to the wall than TS1. During the initial 10 minutes, most of the sulfur was

still at the solid phase and the heat transfer was dominated by heat conduction. Therefore, TS4 was higher than TS1 because it is closer to the heat source. As thermal charging progressed, sulfur liquid fraction increased significantly, causing natural convection as the dominant heat transfer mechanism. Thus, for t > 10 min, TS1 rapidly increased to temperatures higher than TS4.

The viscosity of sulfur is another important factor that governs the heat transfer behavior of sulfur. In Figure 3.4(a), viscosity curves for three grades of sulfur are shown. The solid line presents the viscosity of pure sulfur in an open system [57], which is an ideal laboratory status for sulfur. The other two lines show the viscosity of sulfur in more practical conditions, where the sulfur is impure and dissolves a trace amount (~0.4% molar fraction) of impurity atoms (e.g., hydrogen and iodine atoms) [56,58], decreasing the sulfur viscosity significantly. At the temperatures higher than ~350 °C, the viscosity of impure sulfur in a closed system is higher than it in an open system, due to the higher pressure in the enclosure. Figure 3.4(a) indicates that the variation of the sulfur viscosity with the temperature is significant, which greatly affects the heat transfer characteristics of sulfur. For example, TS5 shows rapid ramp rate from 114 °C (the melting point of sulfur) to 170 °C. During this temperature range, the viscosity of sulfur is significantly low (as is shown in Figure 3.4(a)), resulting in strong convective heat transfer. Beyond 170 °C, the viscosity of sulfur shows a significant increase with temperature, which adversely affects the convective heat transfer within sulfur resulting in slower ramp rate from 170 °C to 200 °C. Similar behavior was exhibited by other sulfur thermocouples at temperatures > 170 °C underlining the effect of viscosity.

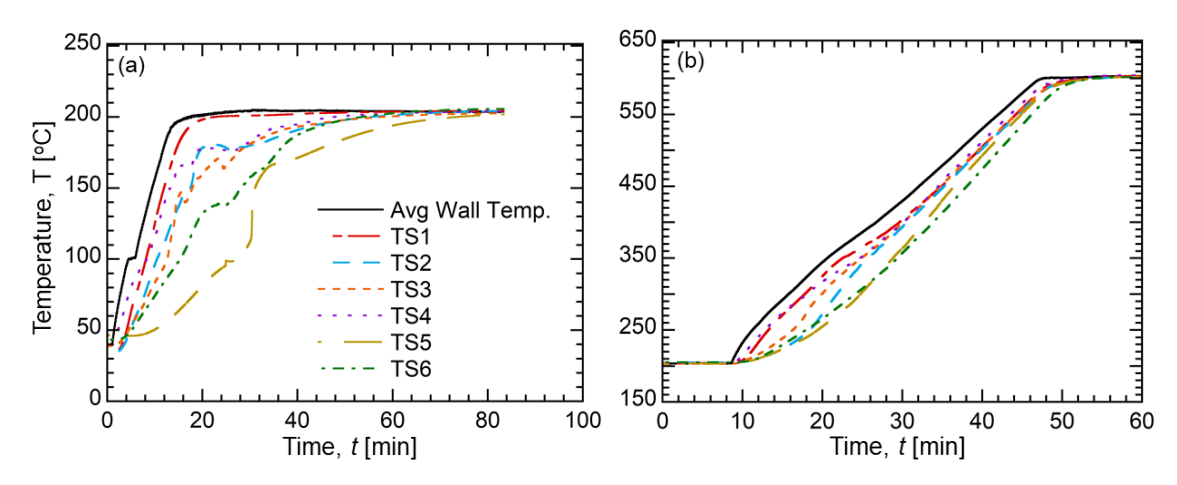


Figure 3.3. Temperature variation of uniform surface temperature condition. (a) Heated from room temperature to 200 $^{\circ}$ C, (b) heated from 200 $^{\circ}$ C to 600 $^{\circ}$ C.

In the second stage, the heat transfer behavior of liquid sulfur was investigated from 200 to 600 °C. The temporal variations in sulfur and wall temperatures are shown in Figure 3.3(b). In this temperature range, the buoyancy-driven natural convection is a dominant heat transfer mechanism that resulted in higher temperature ramp rates as compared to thermal charging in the low-temperature regime. In Figure 3.4(b), we plot the impure sulfur viscosity and the difference between tube wall temperature, T_w , (average of TH1 to TH16), and sulfur temperature, T_S (average of TS1 to TS6), as a function of sulfur temperature. For the sulfur temperatures below 275 °C, the viscosity of sulfur increases with sulfur temperature and decreases the overall heat transfer rate. Therefore, the temperature difference between the wall and the sulfur also increases, reflecting that the thermal response of sulfur is slowing down. For sulfur temperatures above 275 °C, the temperature difference monotonically decreases, due to higher sulfur heat transfer rates in response to the decrease in sulfur viscosity.

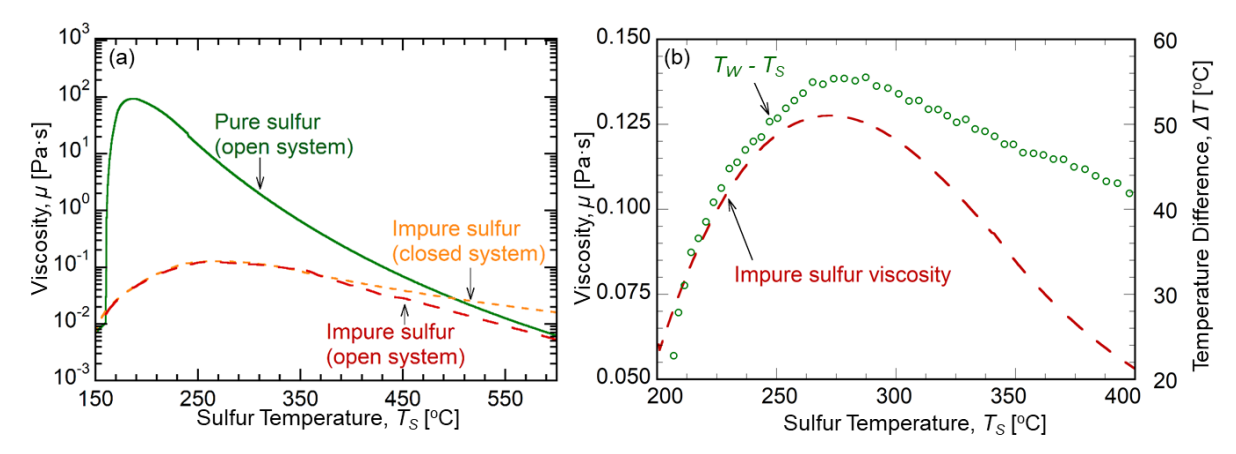


Figure 3.4. (a) Sulfur viscosity variations: pure sulfur in an open system, impure sulfur in an open system, and impure sulfur in a closed system. (b) Impure sulfur viscosity and the temperature difference between the tube wall and sulfur.

The experimental study demonstrates the features of sulfur heat transfer phenomena in both solid-liquid phase change and pure liquid scenarios from 25 to 600 °C. During the thermal charge process, sulfur melts from the periphery of the tube and rises up due to the buoyancy force effect, causing the temperatures at the top and peripheral locations are higher than the bottom and core region. For liquid sulfur, natural convection dominates the heat transfer in the vertical tube and brings a higher heat transfer rate than the solid-liquid phase change scenario. The variation of the heat transfer rate is also affected significantly by the sulfur viscosity, which varies with the sulfur temperature greatly.

3.2. CFD study

3.2.1. Model development

A two-dimensional axisymmetric computational model was developed to further investigate the heat transfer behavior of sulfur. Figure 3.5 shows the computational domain including both the stainless-steel wall of the tube and the sulfur. In the previous study involving isochoric heat transfer characterization of sulfur in the horizontal tube, Nithyanandam et al. [66] assumed sulfur to be in the liquid phase for the temperature range of 200 to 600 °C. The assumption was based on the fact that

the rise in internal pressure during temperature excursion delays the boiling point of sulfur. The computational results obtained with the assumption agreed well with the experimental temperature sensor measurements for various thermal charge scenarios. Hence, we also assumed that the sulfur was at the liquid phase in the vertical isochoric tube for the considered temperature range.

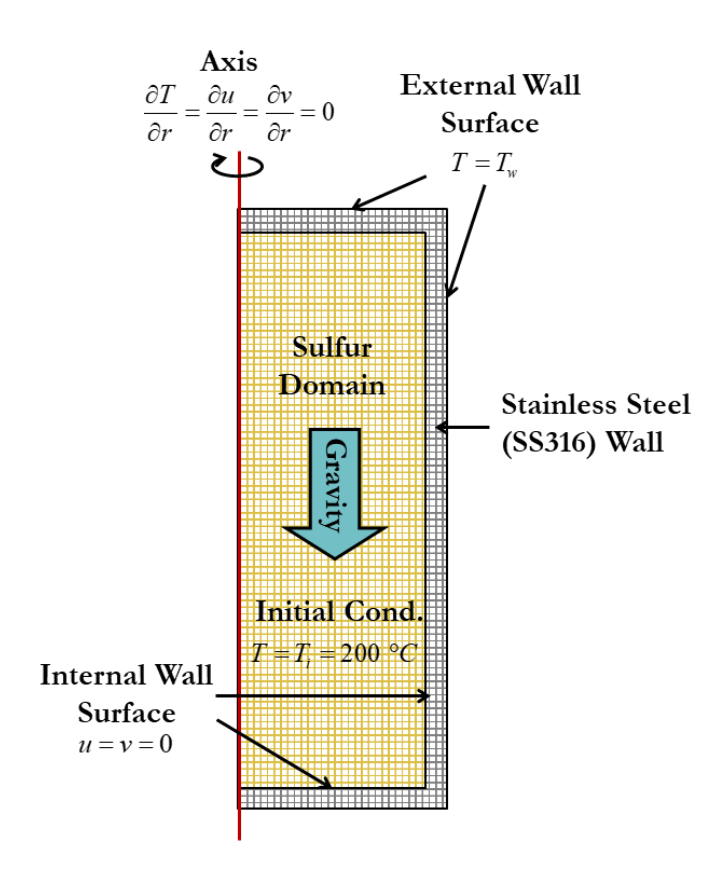


Figure 3.5. Computational domain and boundary conditions

The initial temperature of the system, T_i , was 200 °C and the external wall surface temperature, T_W , was controlled as a uniform temperature boundary condition. The Grashof number, Gr, which is a measure of the ratio of the buoyancy forces to the viscous forces, is defined in Equation 3.1, where g is the acceleration due to gravity, β is the thermal expansion coefficient, ρ is the density, L is the tube length (1 m), μ is the viscosity, and ΔT is the temperature difference between the wall and the

sulfur. The temperature-dependent sulfur density (from 200 to 600 °C) shown in ref. [60] was used in this study and we calculated the thermal expansion coefficient based on Equation (3.2) [74].

$$Gr = \frac{g\beta\Delta T\rho^2 L^3}{\mu^2} \tag{3.1}$$

$$\beta = \frac{1}{\rho} \left(\frac{\partial \rho}{\partial T} \right)_{P} \tag{3.2}$$

The viscosities of both pure and impure sulfur (closed system) shown in Figure 3.4(a) were used to calculate the Grashof number. Figure 3.6 shows the Grashof number for pure and impure sulfur, respectively, as a function of average sulfur temperature. The maximum Grashof number was around 5×10^9 . Evans et al. [75] reported $Gr < 10^{11}$ as the criterion for buoyancy driven flow transition to the turbulent regime. Hence, the laminar flow model was used in this study, since the maximum Grashof number of the sulfur was much lower than the criterion.

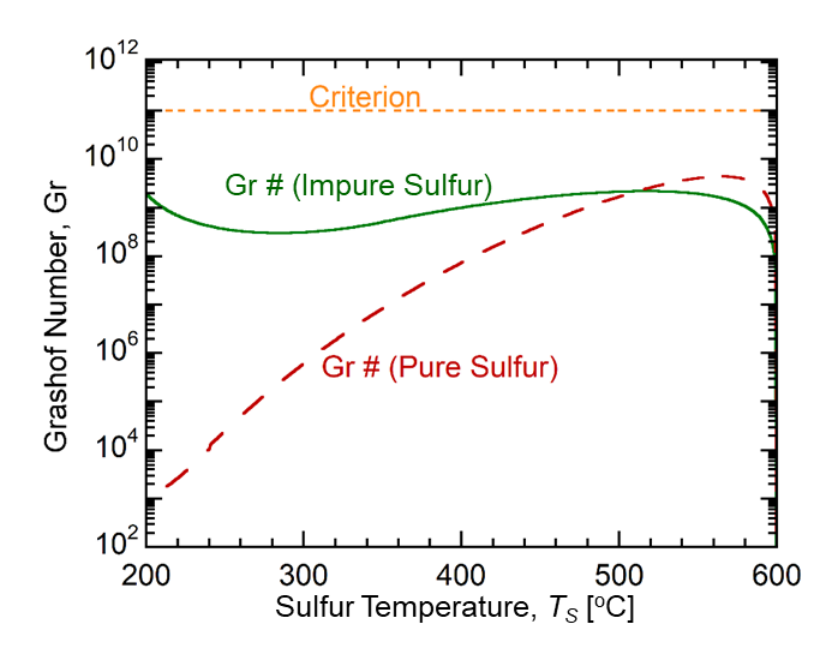


Figure 3.6. Grashof number for pure and impure sulfur vs. criterion for buoyancy-driven flow transition to the turbulent regime.

The coupled continuity, momentum and energy transport equations governing the isochoric thermal charging of sulfur are:

$$\frac{\partial \rho}{\partial t} + \nabla(\rho \vec{v}) = 0 \tag{3.3}$$

$$\frac{\partial \rho \vec{v}}{\partial t} + \nabla \cdot (\rho \vec{v} \vec{v}) = -\nabla p + \nabla \vec{\tau} + \rho \vec{g}$$
(3.4)

$$\frac{\partial}{\partial t}(\rho e) + \nabla \cdot [\vec{v}(\rho e + p)] = \nabla \cdot \left[k \nabla T + (\vec{\tau} \cdot \vec{v}) \right]$$
(3.5)

where the viscous stress tensor $\vec{\tau}$ and the internal thermal energy e are defined in Equation (3.6) and (3.7).

$$\vec{\bar{\tau}} = \mu \left[(\nabla \vec{v} + \nabla \vec{v}^T) - \frac{2}{3} \nabla \cdot \vec{v} I \right]$$
 (3.6)

$$e = h - \frac{p}{\rho} + \frac{|\vec{v}|^2}{2} = \int_{T_{ref}}^{T} c_p dT - \frac{p}{\rho} + \frac{|\vec{v}|^2}{2}$$
(3.7)

In the fluid domain, the temperature-dependent specific heat and thermal conductivity values of sulfur were used, similar to the sulfur heat transfer study in the horizontal configuration by Nithyanandam et al. [66]. Moreover, the model predictions of sulfur temperatures are reported for both pure sulfur and impure sulfur viscosity. Equation (3.8) shows the expressions of density defined by Boussinesq approximation [74]. The reference temperature, T_{∞} , was 400 °C. Considering the loading fraction of current system (~80%), the reference density, ρ_{∞} , and the average thermal expansion coefficient, β , were calculated to be 1380.84 kg/m³ and 4.98 × 10⁻⁴ K⁻¹, respectively.

$$\rho = \rho_{\infty} [1 - \beta (T - T_{\infty})] \tag{3.8}$$

In the solid domain, the constant properties of stainless steel were used. The density, thermal conductivity, and specific heat were 7900 kg/m³, 20.1 W/m·K, and 560 J/kg·K [66], respectively.

3.2.2. Grid size refinement and time step study

A grid size refinement study was conducted to obtain an appropriate mesh for the computational model. The wall temperature was controlled and was uniformly increased from 200 to 600 °C to simulate the experimental wall temperature measurements. The local and volumetric average sulfur temperatures were monitored for four cases with a mesh size of 27 cells/cm², 55 cells/cm², 110 cells/cm² and 220 cell/cm². All the meshes were refined near the wall where the velocity gradient of the flow and the temperature gradient tended to be of higher magnitude. The comparison of the volumetric average sulfur temperatures for these four cases shows the variation among them is less than 0.1%. In addition, the sulfur temperatures at 64 locations uniformly distributed in the domain, were also monitored, with one of the locations being at the bottom region, inside the thermal boundary layer. The effect of the mesh size variation on the temperature of this location is the most obvious, due to relatively higher velocity and temperature gradients. The comparison of this temperature for all four cases is shown in Figure 3.7. The temperature differences between the two consecutive mesh sizes (i.e., 27 vs. 55 cells/cm², 55 vs. 110 cells/cm² and 110 vs. 220 cells/cm²) are 1.8%, 1.5%, and 1.0%, respectively. The mesh size of 110 cells/cm² was selected based on the trade-off between the increase in the accuracy of the numerical simulation results and the increase in computational cost.

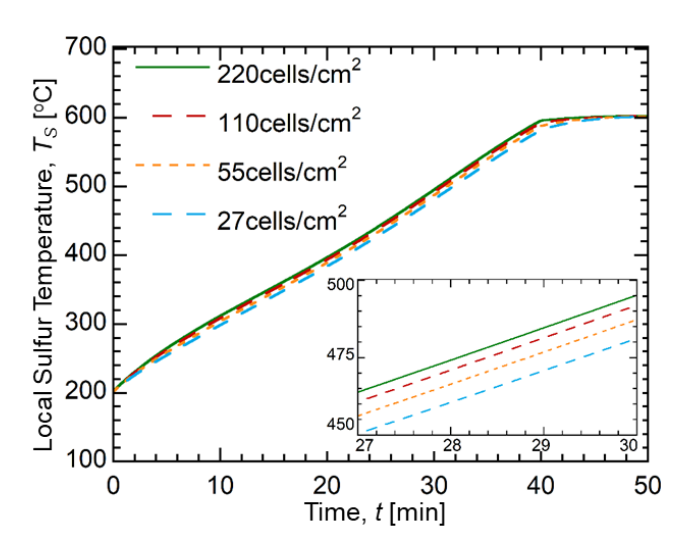


Figure 3.7. Grid size refinement study: comparison of one of the local sulfur temperatures (inside the boundary layer)

The time-step study with three different time steps 0.2 s, 0.1 s, and 0.05 s showed that the variations in both volumetric average temperature and monitored local temperatures were much smaller than 0.1%. Finally, the time step of 0.1 s was used for the numerical simulations.

3.2.3. Model validation

The validation of the computational model included the reproduction of the temperature variations of sulfur stored in an isochoric container of the same size as the tube in the experiments introduced in section 3.1 and comparing them with the experimental results.

The temperature variations of sulfur measured at six different locations during the experimental study were also monitored in the numerical analysis for both pure and impure of sulfur and the results are shown in Figure 3.8. The average errors between the predicted temperatures in the low viscosity (impure sulfur viscosity in a closed system, as shown in Figure 3.4) model and the experimental measurements of TS1 to TS6 are 2.7%, 2.9%, 1.8%, 7.5%, 2.6%, and 1.6%, respectively. Compared with the high viscosity (pure sulfur) case, for which the errors are 6.9%, 3.9%, 5.0%, 11.9%, 7.3%, and 4.8%, the computational model with the low viscosity had a better agreement with the

experiments. Therefore, this viscosity was used in all the later studies, which is consistent with the conclusion in ref. [66]. For TS4, we found the experimental results were consistently higher than the computational results, which is likely caused by position uncertainty of the thermocouple probe tip as discussed in section 3.1. However, even with this uncertainty, the good overall agreement with the experiments provides confidence in the utility and interpretation of the computational model results.

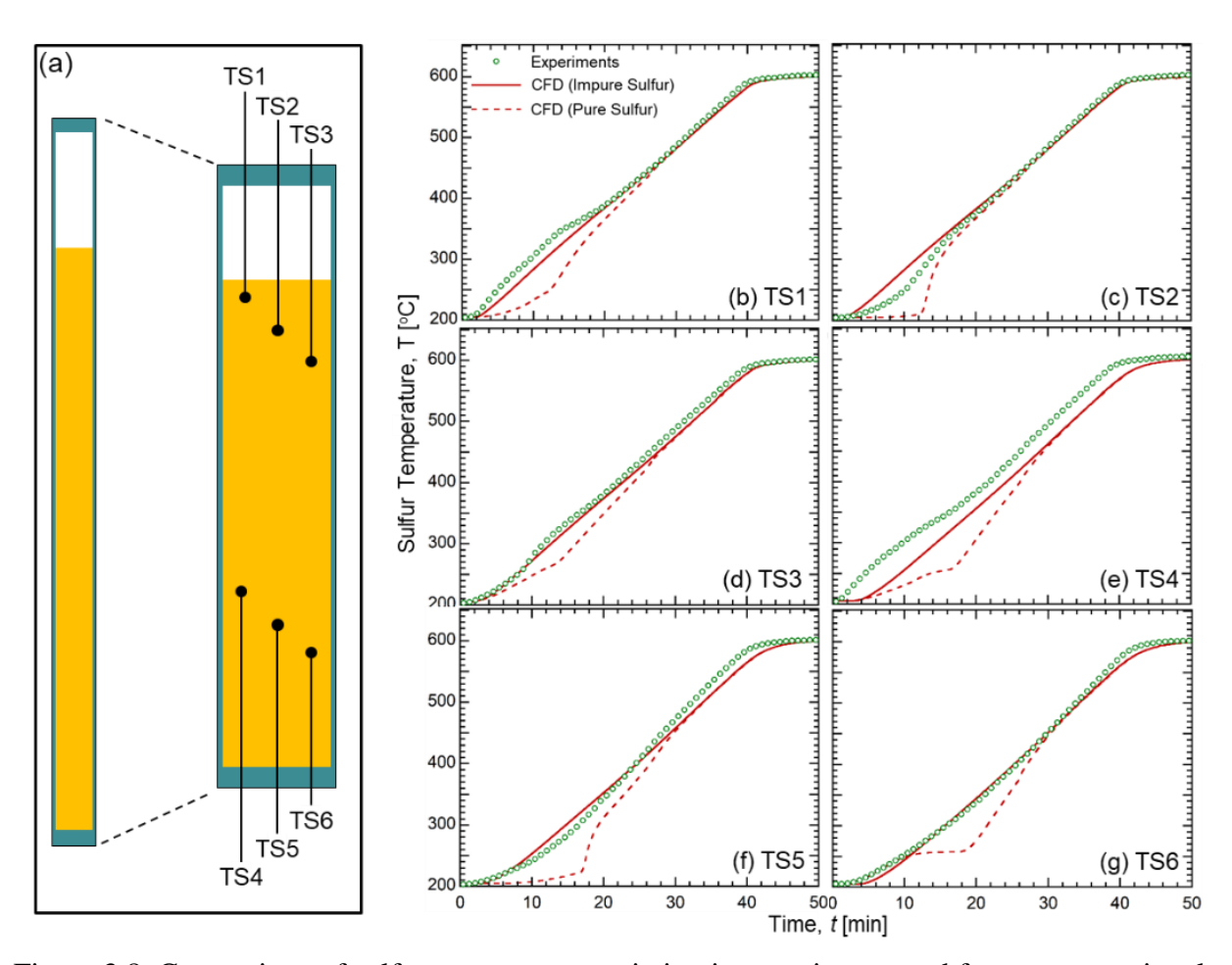


Figure 3.8. Comparison of sulfur temperature variation in experiments and from computational (CFD) model: (a) Locations of thermocouples in the experimental system, (b-g) transient temperature variation of TS1 – TS6

3.2.4. Results and discussions

The computational model was used to further understand the characteristics of buoyancy-driven convective heat transfer in sulfur. Figure 3.9 shows the temperature, velocity, and viscosity contours for three different time instances. During the thermal charge process, the sulfur at the inner wall was preferentially heated and ascended to the top region of the tube, while relatively colder sulfur at the core descended to the bottom of the tube due to buoyancy force resulting in the axial temperature gradient. Early in the simulation, t = 10 min., the average sulfur temperature was around 250 °C, resulting in highly viscous sulfur, especially at the core of the tube. However, the buoyancy-driven currents preferentially heated the top region to a relatively higher temperature (~300 °C) at which the sulfur viscosity is lower than the peak value near 250 °C. Moreover, sulfur at the tube bottom was at ~200 °C with the lowest viscosity within the sulfur domain. At t = 30 min., the average sulfur temperature reached around 450 °C at which the viscosity is significantly lower than that at 250 °C. The effect of the decrease in sulfur viscosity with temperature is reflected in the velocity contours. As shown in Figure 3.9(c), a velocity boundary layer is formed at the wall, wherein the velocity of sulfur ascending through a small area is significantly higher than the sulfur at the core descending to the bottom of the tube through a larger cross-section of the tube. The magnitude of this velocity continuously increased with thermal charging due to the decrease in sulfur viscosity with temperature. At t = 40 min., the charging process was close to its completion, and the viscosity of the sulfur dropped to a very low value (~0.01 Pa·s). In the top region, where the temperature differences between sulfur and the wall were very small, the global circulation became unstable and disintegrated into localized circulations (vortices). The effect of these vortices on the heat transfer behavior of sulfur was likely to be insignificant since they only formed when the sulfur temperature was reaching the wall temperature (near the end of charge).

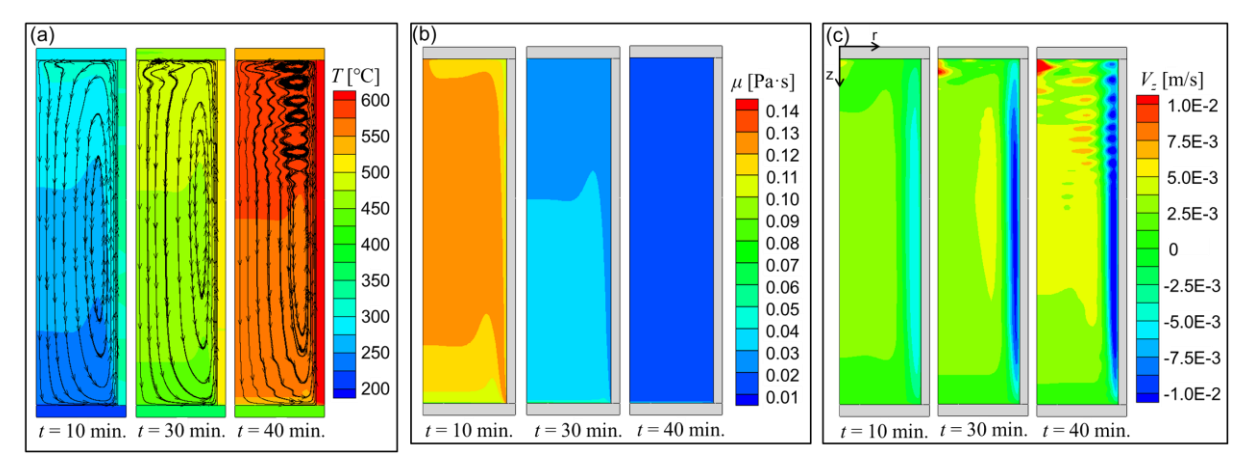


Figure 3.9. Transient variations in sulfur temperature, velocity and viscosity (a) temperature, (b) viscosity, (c) z-velocity.

The computational results were used to calculate the volumetric average sulfur temperature, $T_{S,avg}$, and surface average wall temperature, $T_{w,avg}$, during the thermal charging process. As shown in Figure 3.10(a), the difference between the wall and sulfur temperature decreased with time beyond ~ 250 °C due to the decrease in viscosity at higher temperatures, as discussed earlier in section 2.3. To quantify the heat transfer rate during thermal charging, we define the convective heat transfer coefficient in Equation (3.9). The variation of this heat transfer coefficient as a function of the sulfur average temperature along with the corresponding sulfur viscosity (impure sulfur in a closed system) is presented in Figure 3.10(b). At the beginning of the charging process, the heat transfer coefficient was significantly high due to a step change in the wall temperature, however, it was quickly reduced to $\sim 60 \text{ W/m}^2\text{-K}$. As the thermal charging progressed, the heat transfer coefficient increased with the rise in sulfur temperature. In the temperature range of 200-250 °C, the heat transfer coefficient increased due to the larger temperature difference between the wall and sulfur temperature despite the increase in sulfur viscosity (Figure 3.10(b)). Beyond 250 °C, the convective heat transfer was assisted by the continuous decrease in sulfur viscosity resulting in a higher heat transfer coefficient. Beyond 500 °C, small but consistent fluctuations in the heat transfer coefficient are observed. These

fluctuations are likely due to the formation of local vortices, as shown in Figure 3.9(a) and (c). As the sulfur temperature approached 600 °C, the heat transfer coefficient started to decrease due to a temperature difference between the sulfur and the wall resulted in a rapidly-reduced heat transfer rate.



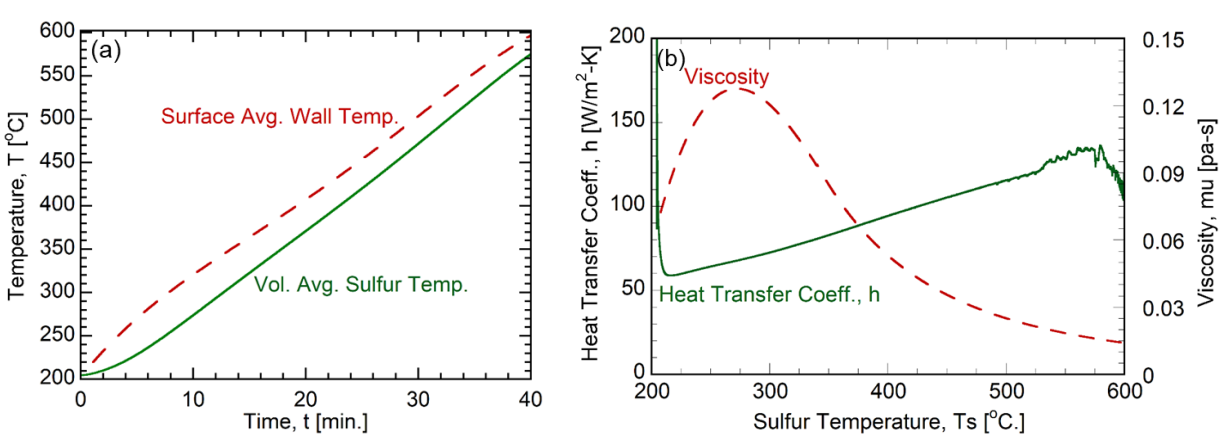


Figure 3.10. (a) Transient variation of average sulfur and wall temperature, (b) transient variation of heat transfer coefficient and viscosity.

3.3. Heat transfer performance analysis

3.3.1. Empirical correlations for Nusselt number

In order to provide an overarching description of the natural convection behavior within the vertical behavior within the vertical tube, this section develops Nusselt number correlations using the computational results. For natural convection over a flat plate, Churchill and Chu [76] suggested that the average Nusselt number is characterized by Rayleigh number and Prandtl number in the form shown in Equation 10. Generally, the function of the Prandtl number is only governed by the material properties and is independent of the geometric parameters. This relation is also supported by multiple studies, e.g. Nithyanandam et al. [66], Lakeh et al [77], Macgregor and Emery [78], and Markatos and Pericleous [79], such that we can express the Nusselt number as:

$$Nu_{L,avg} = f(Pr) \cdot Ra_{L,avg}^m = C \cdot Ra_{L,avg}^m$$
(3.10)

where the exponent, m, and the constant, C, vary with the geometry of the heat transfer domain. We investigated the heat transfer behavior of sulfur in 12 vertical tubes, with length, L as 0.5, 1, 2, and 3 m and the diameter, D as 5.5, 10.8 and 21.2 cm (2, 4, and 8"). Both charge and discharge conditions are considered in this study. During charging, the wall was uniformly maintained at the charge temperature, T_c of 600 °C and during discharging, at discharge temperature, T_d of 200 °C. Based on the method introduced by Lakeh et al [77], the exponent of Rayleigh number, m, was calculated as 0.314 and 0.274 respectively for the charge and discharge conditions. We obtained the constant, C, for the two conditions by conducting a linear curve fit for average Nusselt and Rayleigh number as shown in Figure 3.11.

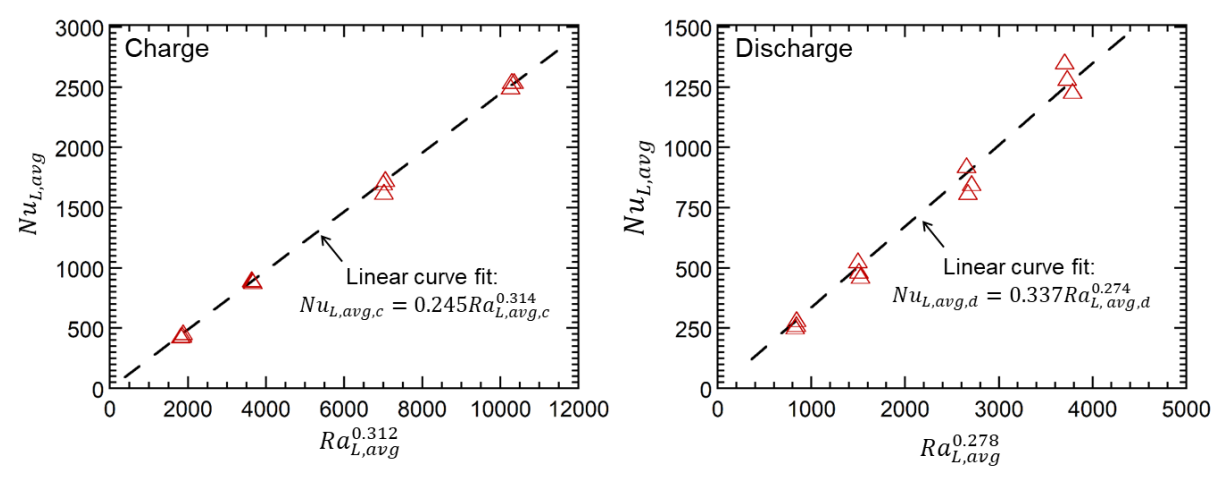


Figure 3.11. Variation of average Nusselt number with average Rayleigh number for (a) charge condition and (b) discharge condition.

The final correlations (2 \times 10¹⁰ < $Ra_{L,avg}$ < 6 \times 10¹²) for charge and discharge conditions are shown in Equation (3.11) and (3.12)

Charge(c):

$$Nu_{L,avg,c} = 0.245Ra_{L,avg,c}^{0.314} (3.11)$$

Discharge(d):

$$Nu_{L,avg,d} = 0.337Ra_{L,avg,d}^{0.274} (3.12)$$

The above correlations can be utilized to predict the sulfur temperature variation using analytical methods. We validated the correlations by comparing these analytical solutions with the results from the computational model.

The energy equation for the volumetric-average sulfur temperature can be expressed as:

$$\rho c_p V \frac{dT_S}{dt} \cong h_{L,avg} A(T_w - T_S)$$
(3.13)

where V is the total sulfur volume, A is the total sulfur surface area, and T_W is the wall temperature, which is 600 °C for the charge condition and 200 °C for the discharge condition. We define the dimensionless sulfur temperature $\theta_S = (T_S - T_d)/(T_c - T_d)$. Then the analytical solutions for θ_S are:

Charge(c):

$$\theta_{S,c} = 1 - \exp\left(-4\frac{L}{D} \cdot Nu_{L,avg,c} \cdot Fo_{L.avg}\right)$$
(3.14)

Discharge(d):

$$\theta_{S,d} = exp\left(-4\frac{L}{D} \cdot Nu_{L,avg,d} \cdot Fo_{L,avg}\right)$$
(3.15)

The variations of dimensionless temperature with Fourier number, $Fo_{L.avg}$ for different systems can be derived by substituting Equation (3.11) and (3.12) into Equation (3.14) and (3.15) respectively. The comparison between the analytical and computational results for the system with a length of 0.5 and 3 m is shown in Figure 3.12. The errors between the two results for all systems vary from 0.5-3.0%, which shows good agreement between computational and analytical results, thus, providing confidence in the Nusselt number correlations as derived.

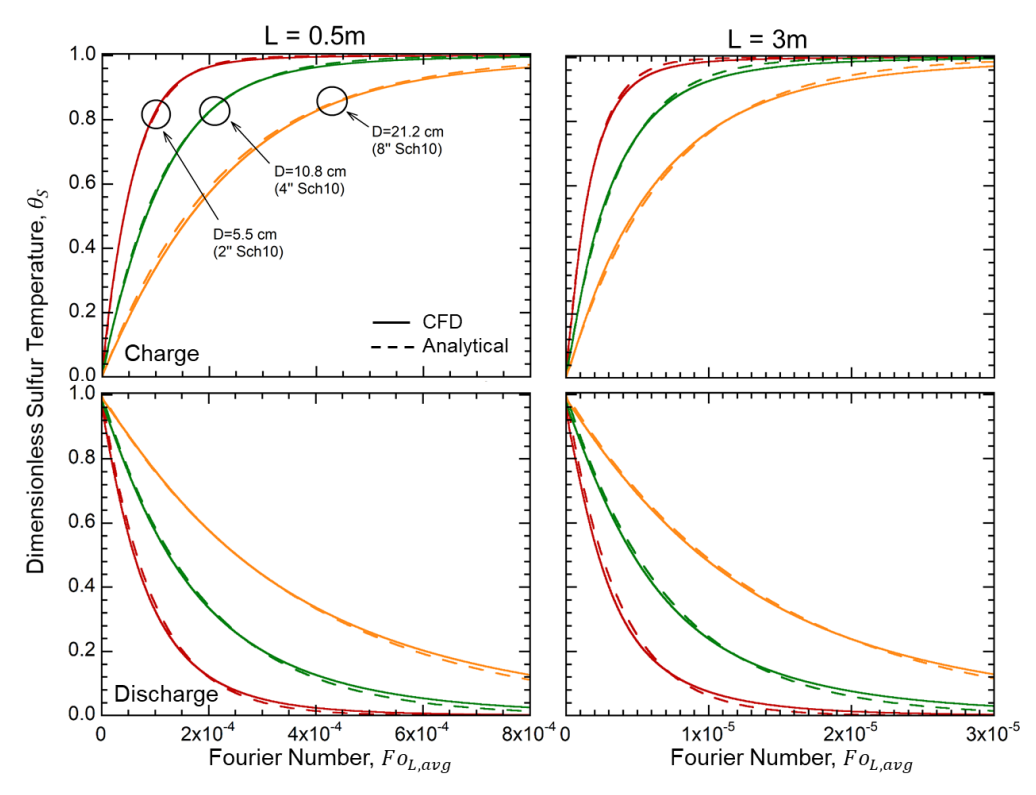


Figure 3.12. Comparison of the dimensionless sulfur temperature from analytical solutions with the CFD results.

The current study provides useful information and reliable tools to estimate the sulfur heat transfer behavior in vertical tubes. These correlations are important design inputs for the system-level performance analysis of SulfurTES applications, such as CSP and CHP.

3.3.2. Comparison with horizontal-oriented tubes

The following discussion compares the thermal charge/discharge performance of the elemental sulfur isochorically stored in vertical and horizontal tubes by comparing thermal charge rates and heat transfer coefficients for a range of tube dimensions and conditions. Nithyanandam, et al. [66] have characterized the thermal charge/discharge performance of sulfur for horizontal tube configuration for the temperature range of 200-600 °C. The computational model developed in this study was used to predict the heat transfer behavior for vertical tubes with the same dimensions; i.e., tube diameters

(5.5, 10.8, or 21.2 cm) and length (1 m); and boundary and initial conditions used in the horizontal tube study.

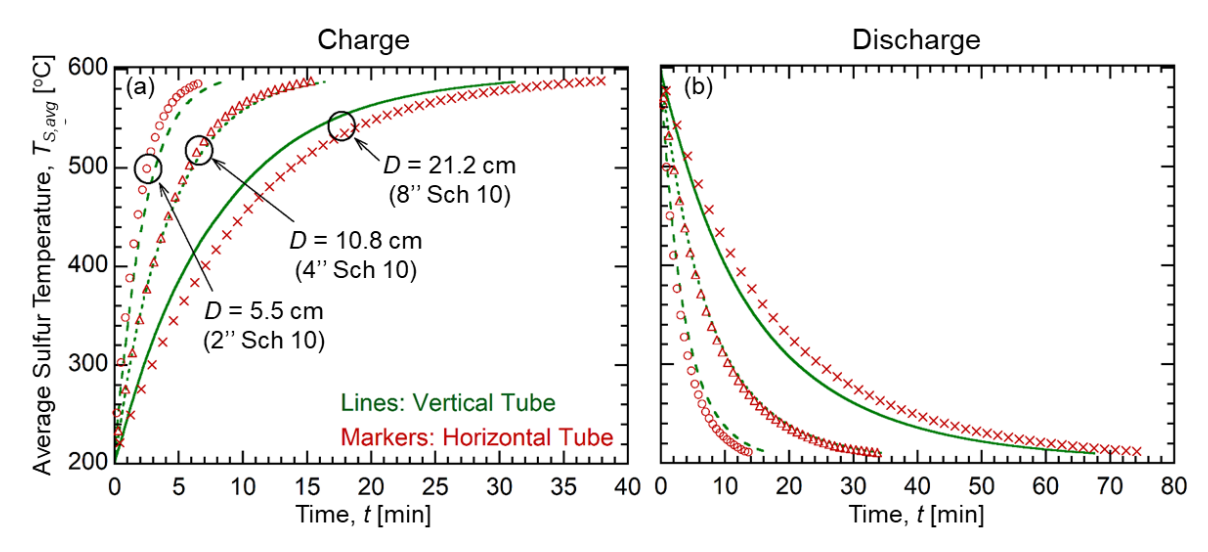


Figure 3.13. Comparison of volumetric-average sulfur temperature variation for (a) charge process and (b) discharge process in the vertical and horizontal tubes.

Table 3.1. Thermal charge and discharge periods for vertical and horizontal tubes.

Tube Diameter, D [cm]	Thermal Charg	ge Period (min)	Thermal Discharge Period (min)		
	Vertical Configuration	Horizontal Configuration	Vertical Configuration	Horizontal Configuration	
5.5	7.1	5.7	13.3	11.1	
10.8	13.8	12.7	26.9	25.8	
21.2	26.2	31.1	52.0	60.7	

Figure 3.13 shows the temporal variation of volume-averaged sulfur temperature for uniform temperature thermal charge ($T_{S,i} = 200 \,^{\circ}\text{C}$, $T_W = 600 \,^{\circ}\text{C}$) and discharge ($T_{S,i} = 600 \,^{\circ}\text{C}$, $T_W = 200 \,^{\circ}\text{C}$) processes. The effective charge and discharge period are assumed to be when the volume-averaged sulfur temperature reaches 580 and 220 $^{\circ}\text{C}$, respectively, as shown in Table 3.1. For both tube orientations, the charge and discharge periods increase with the tube diameter due to the decrease in

the tube surface area per unit sulfur volume. Compared with the charge condition, the discharge process takes more time to complete due to the significant increase of sulfur viscosity with the progression of the discharge process (from 600 to \sim 250 °C). These results also indicate that for the small diameter tube (D = 5.5 cm), the horizontal tube has a higher heat transfer rate, while the large diameter tube (D = 21.2 cm) exhibits higher heat transfer in vertical orientation. As enumerated in Table 3.1, the charge and discharge periods for the vertical tube with diameter of 5.5 cm are about 25% and 20% higher than the horizontal tube, respectively. For the 21.2-cm diameter tube, the vertical charge and discharge periods are about 16% and 14% faster than the horizontal tube.

Figure 3.14 (a) and (b) show the thermal charge/discharge rates, |P|, as a function of average sulfur temperature calculated using Equation (3.16). For both charge and discharge cases, since the temperature difference between the sulfur and the tube wall keeps decreasing, the thermal charge/discharge rates for all the systems also decrease with the progression of charge/discharge processes. Similar to Figure 3.13(a) and (b), Figure 3.14(a) and (b) shows that the horizontal tube with the small tube diameter (D = 5.5 cm) has higher thermal charge/discharge rate than the same-size vertical tube, but for the large-diameter system (D = 21.2 cm), the thermal charge/discharge rate for the vertical tube is almost always higher than the horizontal one.

$$|P| = C_p \left| \frac{dT_S}{dt} \right| \tag{3.16}$$

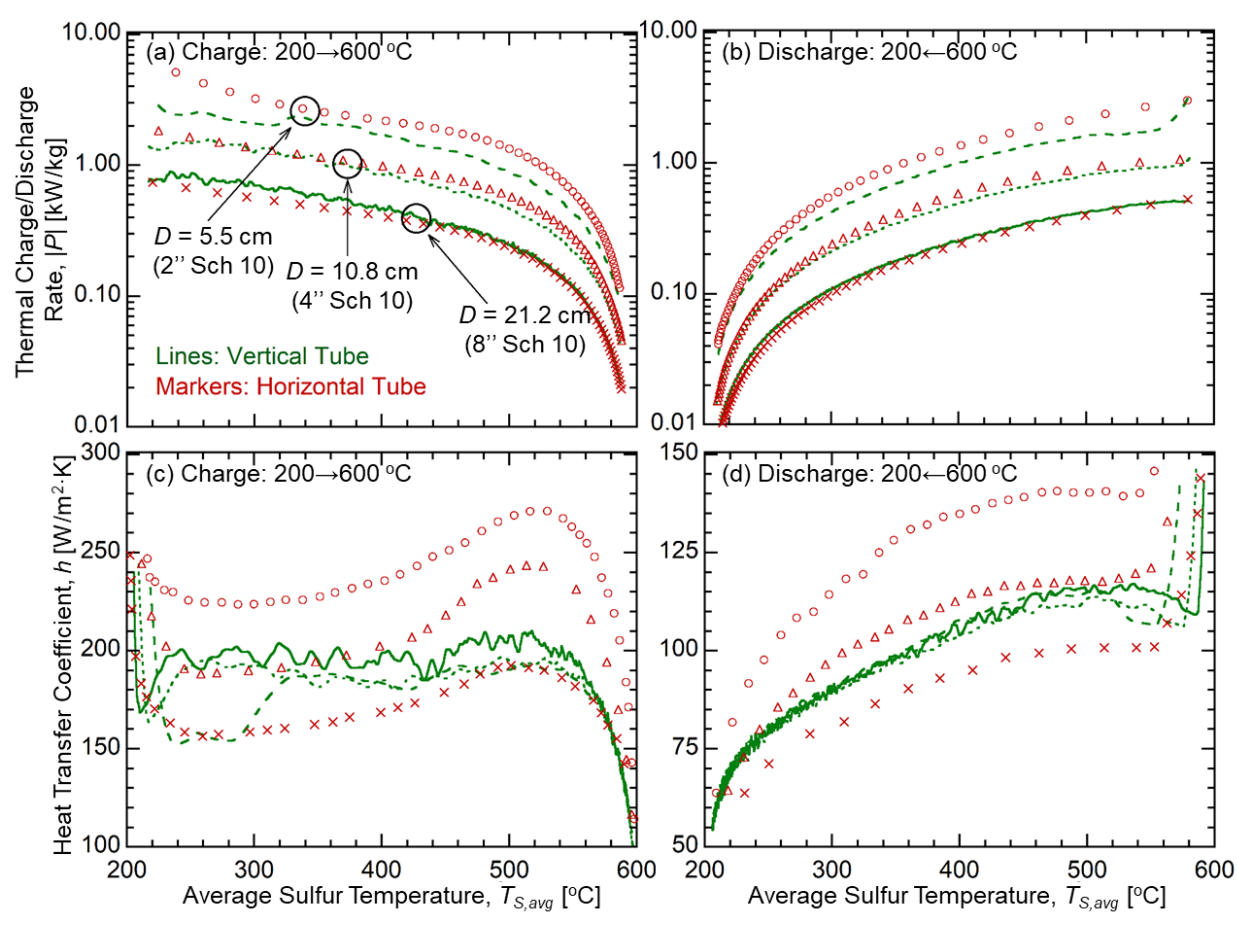


Figure 3.14. Comparison of (a)thermal charge rate, (b) thermal discharge rate, and heat transfer coefficient for (c) charge, (d) discharge in vertical and horizontal tubes.

Table 3.2. Heat transfer coefficients for 1-meter long vertical and horizontal tubes.

Tube Diameter, D [cm]		leat Transfer nt (W/m²·K)	Discharge Heat Transfer Coefficient (W/m²·K)		
	Vertical Tube	Horizontal Tube	Vertical Tube	Horizontal Tube	
5.5	193.4	244.0	119.3	135.9	
10.8	191.4	210.4	108.5	109.6	
21.2	189.1	172.7	102.2	88.9	

As defined in Equation (3.9), we also plot the heat transfer coefficient, h, based on the average sulfur temperature in Figure 3.14(c) and (d). For the horizontal tubes, where the natural convection phenomena are characterized by the tube diameter, the system with a smaller diameter has a larger

heat transfer coefficient during both charge and discharge processes, i.e. h (for D=5.5 cm) >h (for D=10.8 cm) >h (for D=21.2 cm). As for the vertical tubes, the effect of diameter is not dominant since the characteristic length is the tube length instead of the diameter. The average heat transfer coefficients are calculated and shown in Table 3.2. Comparing with the horizontal orientation, the average heat transfer coefficient of vertical is about 21% (charge) /12% (discharge) lower for the small-diameter (5.5 cm) tube, but about 9% (charge) /15% (discharge) higher for the large-diameter (21.2 cm) tube.

The effect of characteristic length on the heat transfer coefficient in both configurations can be better understood by employing the correlations discussed in the previous section. As shown in Equation (3.10), the Nusselt number, Nu_L is governed by Ra_L^m , where m is a non-dimensional parameter. Further, the heat transfer coefficient of natural convection, h, is proportional to the characteristic length, L_C , to the power of 3m-1, as is shown in Equation (3.17).

$$h = \frac{Nu \cdot k}{L_C} \sim L_C^{3m-1} \tag{3.17}$$

Nithyanandam et al. [66] found m to be 0.242 and 0.238, respectively, for thermal charge and discharge of sulfur in horizontal tubes. By substituting these values into Equation (3.17), we obtain the horizontal tube heat transfer coefficient for charge and discharge as:

$$h_{horiz,c} \sim L_C^{-0.274}$$
 (3.18)

$$h_{horiz.d} \sim L_C^{-0.286}$$
 (3.19)

These expressions indicate that the heat transfer rate is inversely related to the characteristic length, which explains the decrease in the thermal charge and discharge performance of horizontal tubes with the characteristic length (tube diameter). For the vertical tubes, the Nusselt number correlations from

Equation (3.11) and (3.12) provide the relationship of heat transfer coefficient and characteristic length as:

$$h_{vert,c} \sim L_C^{-0.058}$$
 (3.20)

$$h_{vert,d} \sim L_C^{-0.178}$$
 (3.21)

Therefore, the heat transfer rate of vertical tubes also decreases with the characteristic length, which is the tube length in this study. Furthermore, since the absolute values of the exponent for the vertical tubes (in Equation (3.20) and (3.21)) are lower than those for the horizontal tubes (in Equation (3.18) and (3.19)), it follows that the heat transfer coefficient for vertical orientation is less sensitive to the characteristic length.

The Nusselt number correlations discussed in section 3.3.1 can be used to compare the relative merit of thermal performance for tubes of different combinations of tube dimension (diameter and length) and orientation (vertical vs. horizontal) for thermal charge and discharge. The results of this comparison are shown in Figure 3.15. Tube dimensions that exhibit identical heat transfer coefficients during the charge process for both vertical and horizontal orientations fall on the red solid line. Similarly, tube dimensions for the red dashed line exhibit identical heat transfer coefficients during the discharge process for both orientations. For tube dimensions located in region A, the heat transfer coefficient for vertical tubes is higher than it for horizontal during both charge and discharge processes. In region B, the heat transfer coefficient for vertical is higher than horizontal during the charge process but is lower than horizontal during the discharge process but lower than horizontal during the charge process. And, in region D, the heat transfer coefficient for vertical is lower than horizontal during both charge and discharge processes. Therefore, with the specific tube geometric parameters, the better orientation could be selected based on this result.

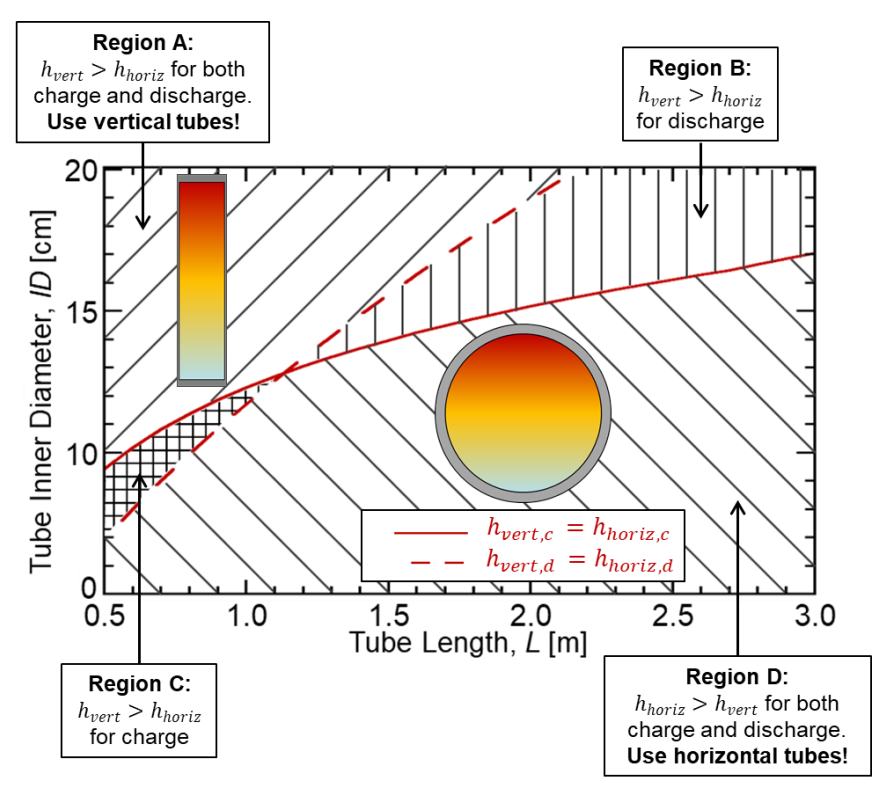


Figure 3.15. Comparison of relative charge and discharge heat transfer coefficient for tube dimensions (length and diameter) and orientation (vertical or horizontal). (Region A: $h_{vert,c} > h_{horiz,c}$; $h_{vert,d} > h_{horiz,d}$. Region B: $h_{vert,c} > h_{horiz,c}$; $h_{vert,d} < h_{horiz,d}$. Region C: $h_{vert,c} < h_{horiz,c}$; $h_{vert,d} > h_{horiz,d}$. Region D: $h_{vert,c} < h_{horiz,c}$; $h_{vert,d} < h_{horiz,d}$)

In general, increasing the tube diameter and length can significantly decrease the heat transfer performance for horizontal and vertical tube configurations, respectively. For lower aspect ratio $(L/D < \sim 7)$ tubes, the heat transfer coefficients in a vertically oriented tube tend to be higher, while the higher aspect ratio tubes are more likely to provide higher heat transfer coefficients in horizontal orientation. The selection of tube orientation strongly depends on the specific values of these geometric parameters. For the design of a SulfurTES, the results from the current study can guide designers to select the appropriate tube configuration based on the system dimensions and performance requirements.

3.4. Conclusions

The present study examines the important characteristics of the heat transfer behavior of sulfur isochorically stored in vertically oriented tubes. Comparisons of experimental, computational, theoretical results show that distinct physical mechanisms govern sulfur heat transfer performance between the room temperature (25 °C) and 600 °C. For sulfur temperatures from 25 to 275 °C, the solid-liquid phase change and the viscosity rise in lower temperature liquid sulfur result in relatively slow heat transfer rates. For temperatures higher than 275 °C, the viscosity of liquid sulfur drops rapidly and helps increase the thermal charging rates. The validated computational model was further utilized to develop the Nusselt number correlations for both thermal charge and discharge.

Compared with the horizontal tube configuration, the heat transfer rate between 200 and 600 °C for the 1-m long vertical configuration is about 10-25% lower for small-diameter (5.5 cm or smaller) tubes but about 9-15% higher for large-diameter (21.2 cm or larger) tubes under both charge and discharge conditions. Heat transfer performance is inversely proportional to the characteristic length for both horizontal and vertical tubes. The more desirable tube orientation in a SulfurTES system depends on the tube and system dimensions. In general, it is found that lower aspect ratio (L/D) tubes provide higher heat transfer coefficients in a vertical orientation while the high aspect ratio tubes provide higher heat transfer coefficients in a horizontal orientation. This is because the characteristic length for the heat transfer coefficient for vertical and horizontal tubes is based on the length and diameter, respectively. We also developed the comparison diagram of the heat transfer coefficients in the two orientations for various tube dimensions. The current study is a first of its kind and provides important quantitative and qualitative design and performance relationships for SulfurTES systems that employ sulfur isochorically contained in tube-shaped vessels.

Chapter 4

Sulfur heat transfer in vertical tubes with nonuniform charge

Heating sulfur tubes predominantly from one end (nonuniform charge) is more likely to be encountered in practice for SulfurTES thermal battery systems with vertical sulfur-filled tubes. As shown in Figure 4.1, for vertical tube configurations, the heat transfer fluid can thermally charge the sulfur tube predominantly from one end. In Figure 4.1(a), the hot heat transfer fluid enters the top of the shell and exits at the bottom. In this way, the tube is progressively heated from top to bottom (in the direction of gravity), which we call the "top-heating" in this study. In contrast, in the second scenario as shown in Figure 4.1 (b), the sulfur tube is heated from bottom to top, in the direction against the gravity, which we call a "bottom-heating". The two conditions could provide significantly different sulfur heat transfer behavior in vertical tubes. One would expect that an axial thermocline will form and be held within the sulfur due to the buoyancy effect for top-heating and this can result in a higher exergy charge rate compared to the uniform- or bottom-heating. On the other hand, for bottom-heating, we expect the buoyancy effect will cause a strong mixing between the hot and cold sulfur, potentially yielding higher energy charge rates.

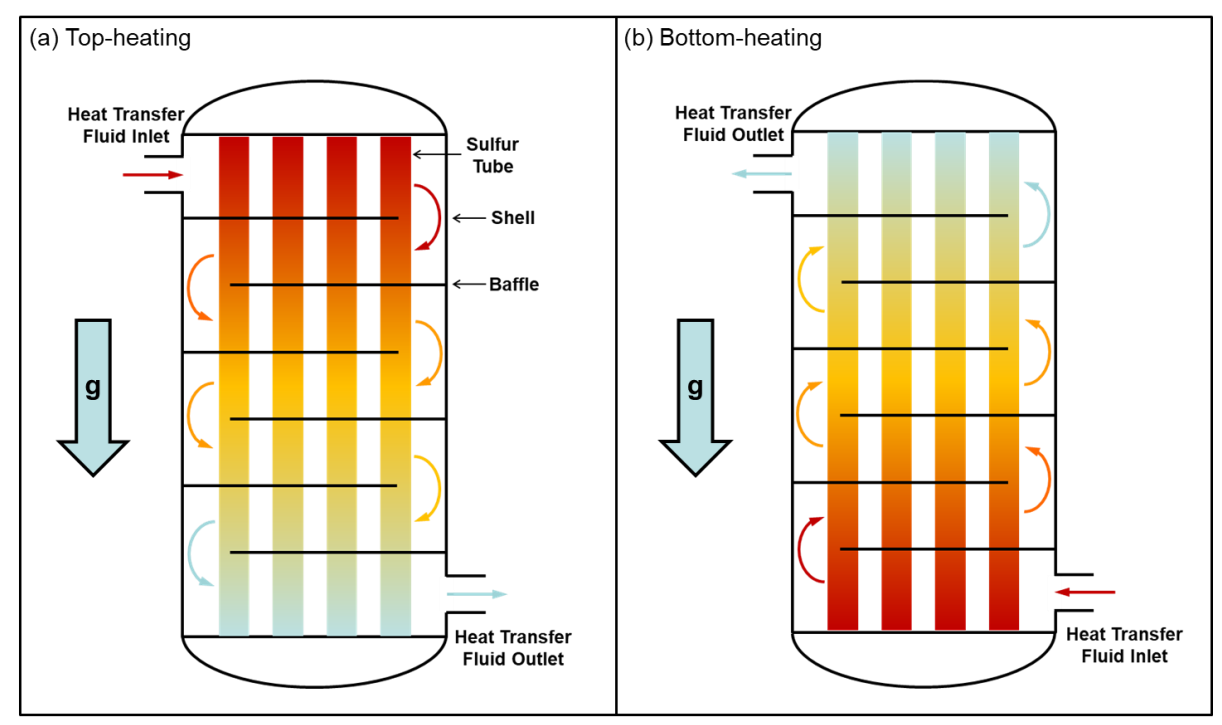


Figure 4.1. Schematics of thermal charging in thermal battery SulfurTES system in (a) topheating, (b) bottom-heating.

The objective of this study is to investigate the heat transfer behavior of sulfur in verticallyoriented tubes undergoing the nonuniform thermal charge conditions, i.e., top heating and the
bottom-heating. These two conditions simulate two practical charge behaviors in a thermal battery
system with vertical tube configuration wherein the heat transfer fluid is introduced from the top or
the bottom of storage tubes. A series of experimental tests were conducted to understand the
characteristics of the sulfur heat transfer behavior in both top heating and bottom-heating. An
accompanying computational study was used to examine detailed characteristics of the flow and
temperature field within the sulfur. The energy and exergy charge rate for the two scenarios were
investigated and compared with the uniform-heating. The advantages and disadvantages of both
charge conditions are discussed, and the simplified analytical procedures are purposed to estimate the
energy and exergy charge behavior of sulfur in tubes of various sizes. The results from this study
provide critical design bases for the development of sulfur-based TES systems.

4.1. Experimental study

In this experimental study, the facilities developed in Chapter 3 were utilized to investigate the heat transfer behavior of sulfur in a vertically-oriented isochoric stainless-steel tube. This tube is thermally charged by 8 PID controlled heaters to mimic the top-heating and the bottom-heating scenarios in the real thermal battery system. The temporal temperature distributions of the tube wall and the sulfur were measured to exhibit the heat transfer characteristics under the two nonuniform charge scenarios.

There were two thermal charge stages in the tests. In the first stage, a linear wall temperature distribution along the axial was imposed. The temperature was 600 °C at the hot end and was 250 °C at the cold end. After the sulfur temperature field became steady, we started the second thermal charge stage, where the whole tube was heated to 600 °C gradually from the hot end to the cold end. In this stage, the heater temperature of the section near the hot end was set to be 600 °C first. After the wall temperature of this section reached 600 °C, we began to heat the next section in the same manner, until the whole tube was charged to 600 °C.

Figure 4.2 shows the steady-state axial temperature profile for the system in the first charge stage. For the top-heating scenario, the imposed wall temperatures were set in sequence to be 600, 550 to 250 °C from top to bottom, as shown in Figure 4.2(a). Because of the effect of buoyancy, the hotter fluid with lower density rose and stayed at the top region and the colder sulfur accumulated at the bottom, resulting in a thermal stratification along the tube length. Due to the absence of significant mixing of sulfur mass and the poor axial conduction heat transfer, the temperature gradient of both sulfur and tube wall could be maintained very well. The experimental measurements show that all 6 sulfur temperatures (TS1 to TS6) are consistent with the wall surface temperatures in the same axial location, which also match well with the set temperature values.

In the first charge stage of the bottom-heating scenario, the wall temperatures were set to be 250, 300 to 600 °C from top to bottom, as shown in Figure 4.2(b). From the measurements, neither wall nor sulfur temperatures are able to reach the set values. The bottom wall temperatures are higher than sulfur temperature (TH12 to TH16 > TS4 to TS6). On the contrary, the top wall has a lower temperature than the sulfur does (TH1 to TH5 < TS1 to TS3). In this case, the directions of heat flow in the top and the bottom regions were opposite. At the bottom section, the wall temperature was always higher than sulfur temperature, resulting in the heat flow from the wall to sulfur. The sulfur close to the wall in the bottom region was heated and therefore had a lower density than the sulfur at the top. The buoyancy force lifted the hotter sulfur to the relatively cold top region, wherein the sulfur temperature is higher than wall temperature, resulting in the outward flow of heat from sulfur to the wall. Compared with the top-heating, this global natural convection causes a much stronger mixing between the hot and cold fluid and is likely to have a higher heat transfer rate. In the plot of Figure 4.2(b), TH1 and TH2 are much lower than the other temperatures. It is likely due to the presence of void at the top region, which contributes much less to convective heat transfer than sulfur does. In addition, heat loss from the top end of the system could also contribute to lower TH1 and TH2.

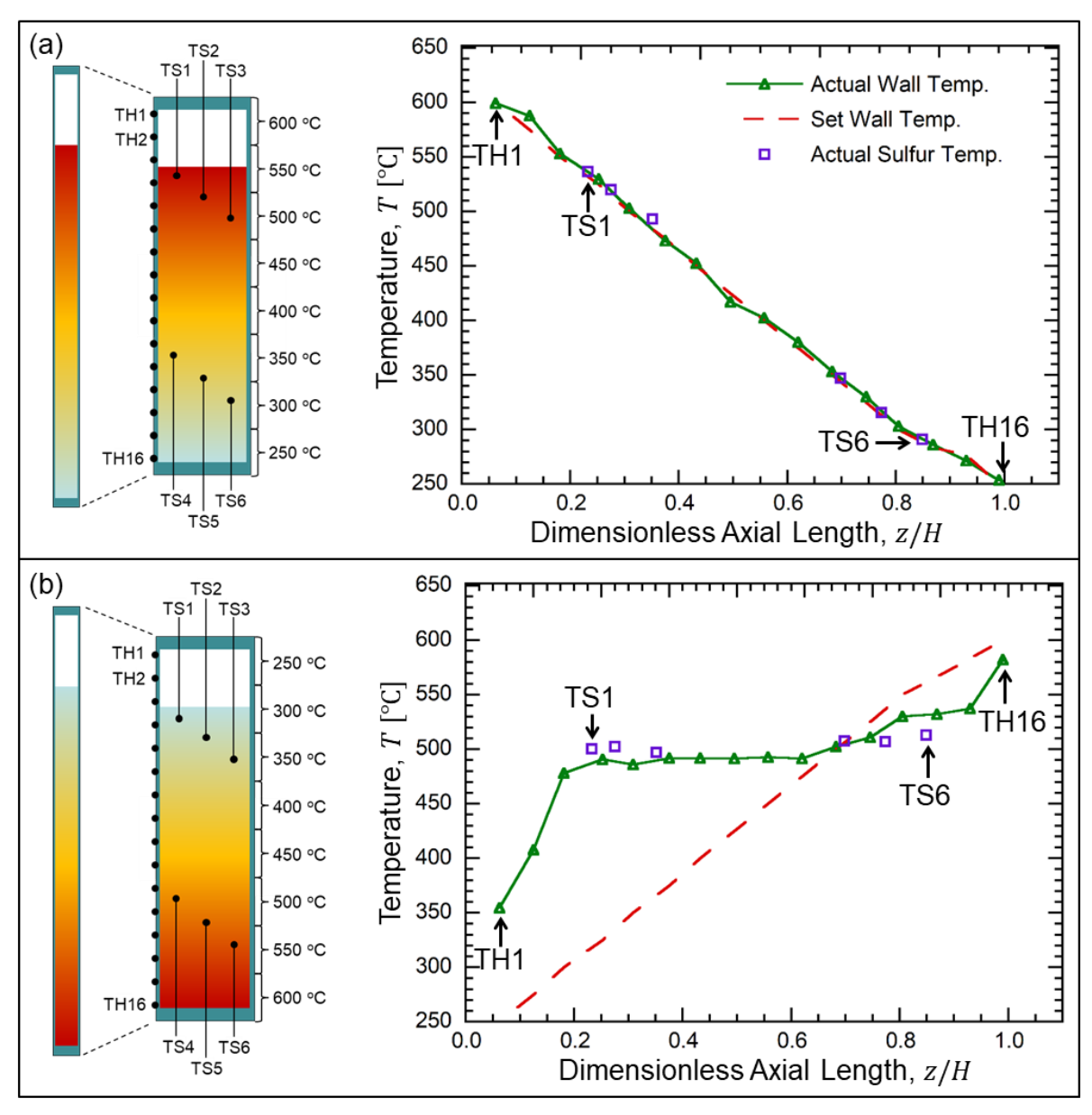


Figure 4.2. The steady-state axial temperature profile of the system in the first heating stage for (a) the top-heating scenario and (b) the bottom-heating scenario.

In the second stage, the wall temperatures controlled by the 8 heaters were set to 600 °C from the hot end to the cold end in turns. Figure 4.3 shows the temporal axial temperature profiles for both heating cases during this stage. For the top-heating scenario, the system was heated to 600 °C from the top to the bottom. In Figure 4.3(a), the starting point of the timeline is when the steady-state of the first stage was reached. At this moment, top heater temperature (TH1 and TH2) reached 600 °C

and the subsequent heater temperature (TH3 and TH4) was just set to 600 °C. During the whole charging process, the sulfur axial temperature distribution was found to be consistent with the wall temperature at different times, because of the absence of the mixing between hot and cold fluid.

Figure 4.3(b) presents the axial temperature distribution for both wall and sulfur temperature at different time instances for the bottom-heating scenario, wherein the heater temperatures were set to 600 °C in turns from the bottom to the top. In this case, the global natural convection became dominant and the temperature field was not able to achieve the set temperatures. The sulfur temperatures at the bottom (TS4 to TS6) were lower than the wall temperatures (TH11 to TH16) before they reached 600 °C, while the sulfur temperatures at the top (TS1 to TS3) were higher than the wall temperature (TH1 to TH5). During the whole charging process, sulfur extracted heat from the wall at the bottom region and rose to the top, heating the wall in this region.

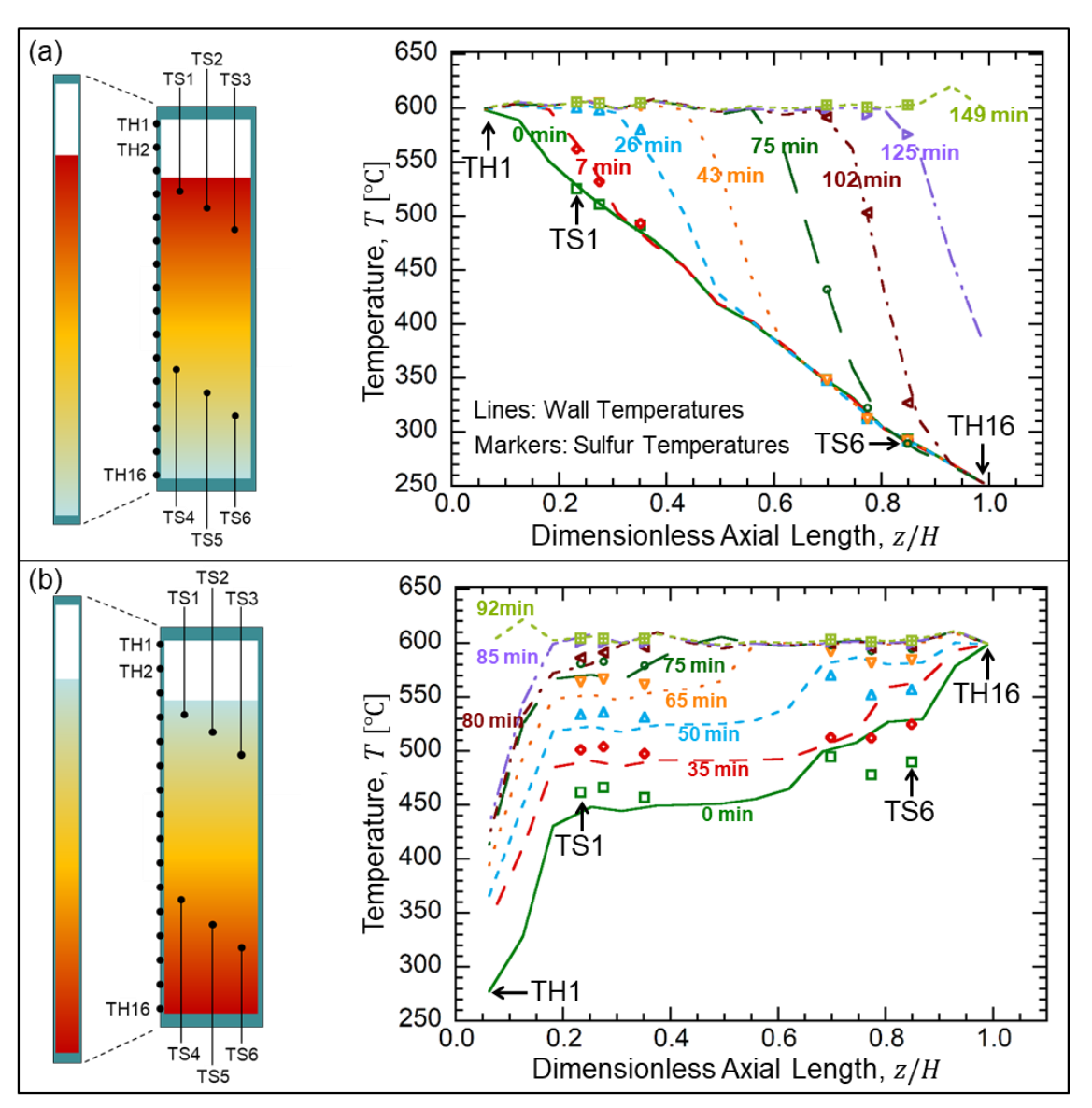


Figure 4.3. The temporal axial temperature profile of the system in the second heating stage for (a)-(b) the top-heating scenario and (b) the bottom-heating scenario.

4.2. CFD study

In the previous study (section 3.2), we developed and validated a two-dimensional axisymmetric CFD model to study the heat transfer behavior of sulfur in uniform charge and discharge scenarios. This computational model was also used in the current study to investigate the sulfur heat transfer behavior under the nonuniform charge conditions.

4.2.1. Experimental boundary conditions

The computational model was used to predict the temperature and the flow field of sulfur for the experimental boundary conditions discussed in section 2. Figure 4.4(a)-(f) show the comparison between the measurements in the experimental and computational predictions of the sulfur temperature for the top-heating scenario. The average errors between the two results on TS1 to TS6 are 1.5%, 1.0%, 1.7%, 1.7%, 1.8%, and 1.5%, respectively. For the bottom-heating scenario, the comparison is shown in Figure 4.4(g)-(l) and the average disagreements between the two results on TS1 to TS6 are 1.6%, 2.0%, 1.8%, 6.4%, 3.1%, and 4.1%, respectively. Overall, the computational model predictions agree very well with experimental results for both cases, further validating this computational heat transfer model.

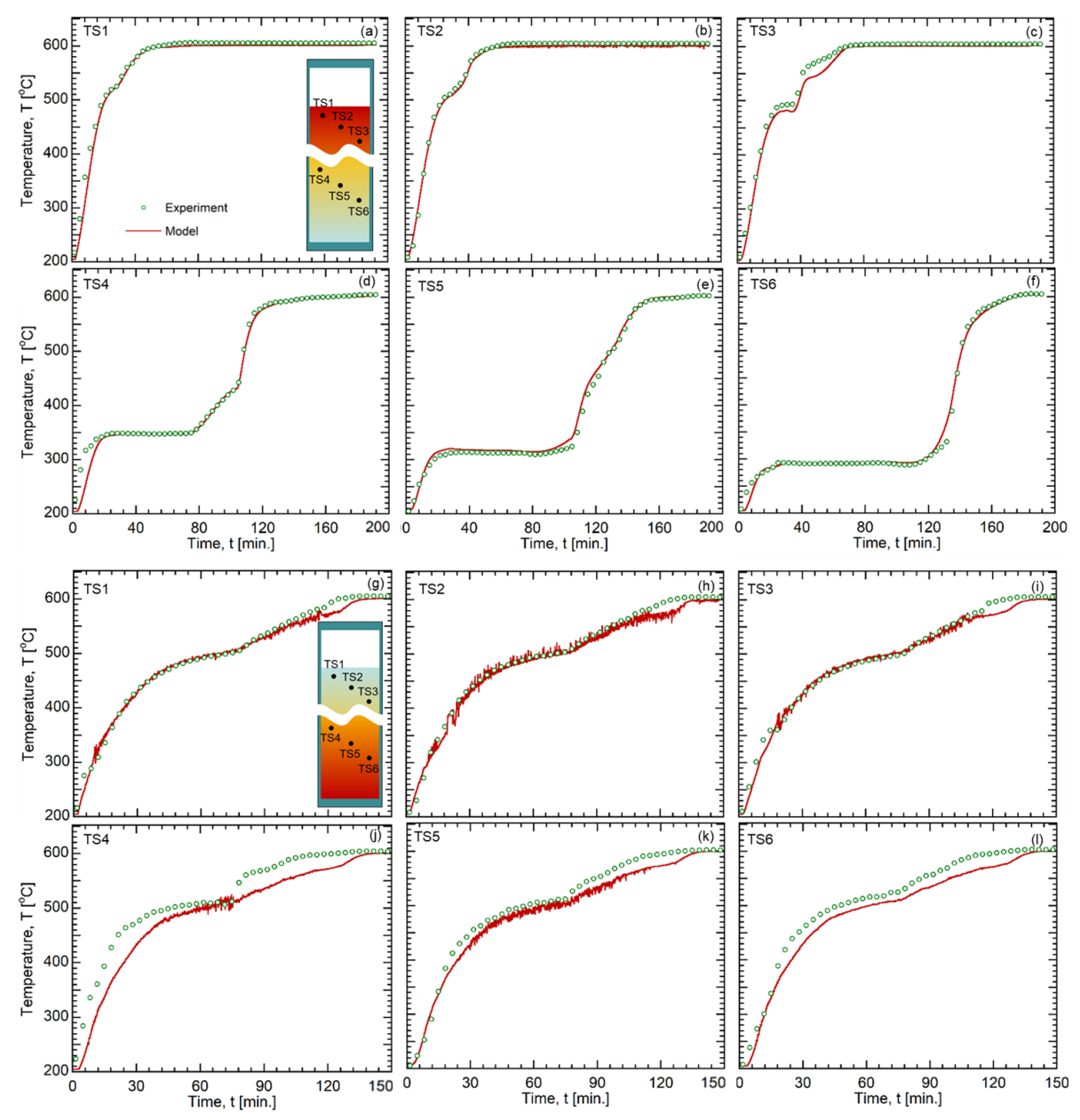


Figure 4.4. Comparison of sulfur temperature variation in the experiments and the computational model: (a-f) the top-heating scenario, (g-l) the bottom-heating scenario.

With the CFD model, we further studied the temperature and flow field of sulfur for the experimental boundary conditions. Figure 4.5 shows the temperature & streamlines, the viscosity, and the axial velocity contours in the 2-D domain at different time instants for both cases. For the top-heating scenario (Figure 4.5(a)), at t = 20 min, the temperature profiles of the wall and the sulfur are

almost linear from 600 °C at the top to 250 °C. The sulfur is heated to the imposed temperature and rises along the wall, forming global convection currents. Afterward, at t = 40 min and 120 min, the imposed thermal front of the wall is propagating from the very top region to the subjacent region. The temperature stratification of both the wall and the sulfur is held very well during the whole thermal charging process. The convection currents break into multiple localized convection cells. The rotating orientation of the neighboring cells is opposite to keep the finite shear stress at the interface. The axial velocity contours in Figure 4.5(c) also supports these observations. The existence of these convection cells validates our expectation that the global convection currents are absent during the thermal front propagation process, but the small-scale local convection currents still exist and dominate the heat transfer of liquid sulfur. The viscosity map of sulfur is shown in Figure 4.5(b). Since the viscosity is significantly dominated by the sulfur temperature, the low viscosity front (around 0.01-0.02 pa·s) propagates from top to bottom with the sulfur thermal front. It also reflects the stable thermal stratification of sulfur during the top-heating charge process. In the velocity contours (Figure 4.5(c)), the velocity of the currents in the high temperature (around 600 °C) region is significantly higher than the other parts due to the lower viscosity. For the region where the sulfur is being heated from 250 to 600 °C, the axial velocity magnitude of the buoyancy-driven flow is around 0.002 m/s.

For the bottom-heating scenario, Figure 4.5(d) shows the temperature & streamline map at the three different time instants. At t = 20 min, the linear temperature profile from 250 °C to 600 °C is imposed on the tube surface using heaters. In the lower half region (around 2/3 of the height from the bottom), the wall has a higher temperature and thus heats the sulfur. The heated sulfur at the bottom rises along the wall and forms a counter-clockwise rotating convection cell in this region. At the top region (around 1/3 the of height from the top), sulfur gains the heat by the advection from the bottom and has a higher temperature than the wall, resulting in clockwise-rotational convection currents. These currents break apart at the top left part of the tube and there forms another convection

cell with the inverse rotating direction. The reason is that the sulfur temperature at this part is low due to the heat loss from the top wall of the tube There is no thermocline within the sulfur because of the global natural convection currents. In Figure 4.5(e), the uniformity of the viscosity map also reflects that the temperature field of sulfur is nearly uniform, due to the effect of global natural convection currents. At t = 40 min, the imposed thermal front of the wall has propagated further to the top. From the streamlines (Figure 4.5(d)) and velocity contours (Figure 4.5(f)), the counter-clockwise convection cell occupies around 2/5 of the tube at the bottom, where the wall temperature is higher than sulfur temperature. As the imposed thermal front propagates from bottom to top, the flow of heat is from wall to sulfur and the counterclockwise currents span almost the entire length of the tube as observed in Figure 4.5(d) for t = 120 min. The velocity maps in Figure 4.5(f) show that the velocity magnitude of the natural convection currents is around 0.04 m/s, which is an order of magnitude higher than that observed for the top-heating scenario (around 0.002 m/s), thus substantiating the higher intensity of natural convection currents in bottom-heating scenario compared to the top-heating scenario.

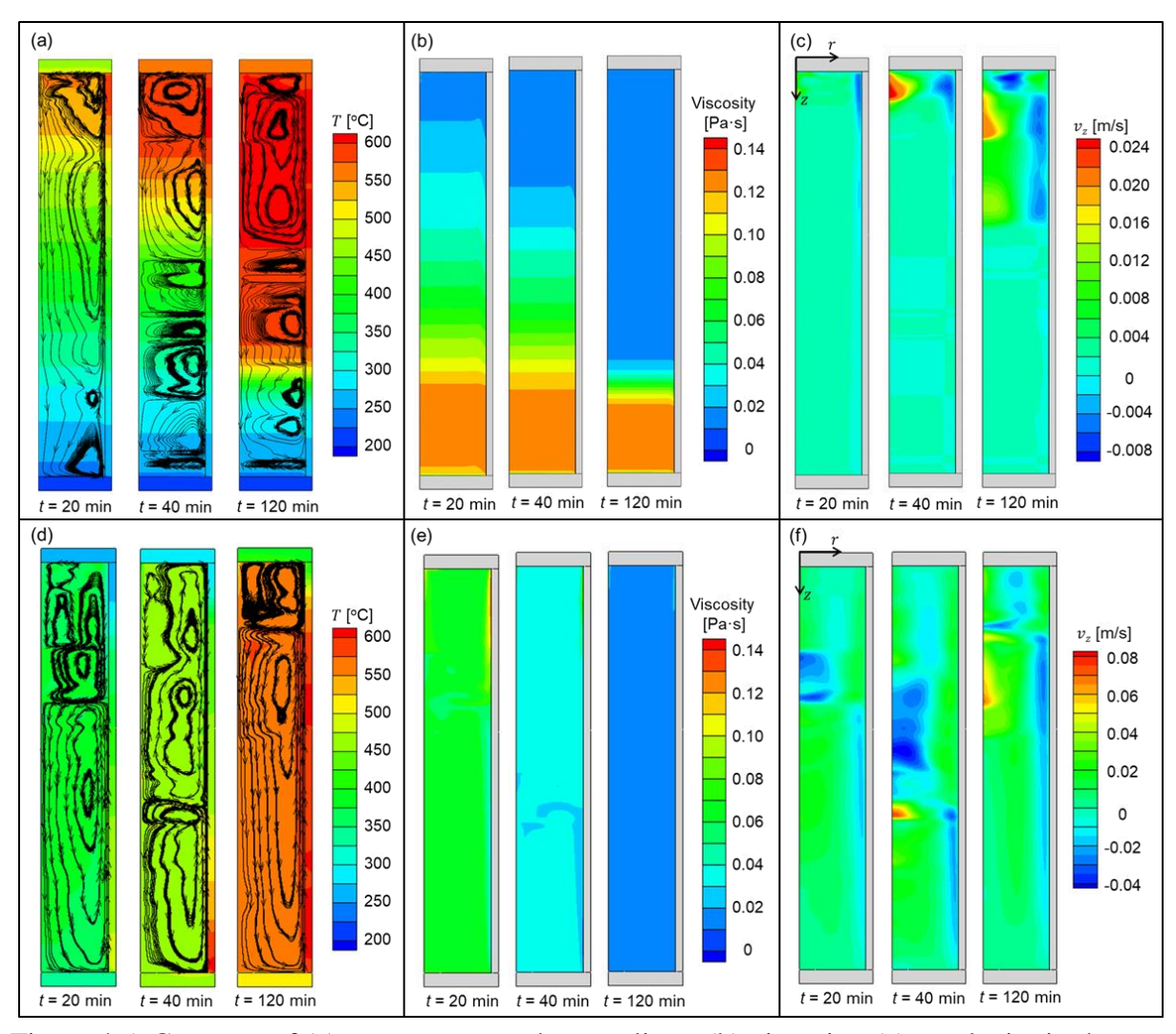


Figure 4.5. Contours of (a) temperature and streamlines, (b) viscosity, (c) z-velocity in the top-heating scenario, (d) temperature and streamlines, (e) viscosity, and (f) z-velocity in bottom-heating scenario.

4.2.2. Canonical boundary conditions

In the investigation for the cases with the experimental boundary condition, the distinct characteristics of the heat transfer for the two nonuniform charge cases are revealed. However, the imposed boundary conditions of these two cases are not comparable, since we were not able to fully control the wall temperature for the bottom-heating scenario because sulfur transfers heat to the wall.

Hence, a further computational study is conducted to compare the energy and exergy charge rates for various scenarios with well-prescribed canonical thermal charge conditions.

Three different scenarios, including top-heating, bottom-heating, and uniform heating, are investigated and discussed in this section. The spatial average wall temperature in these cases is identical during the charging process, to guarantee that three cases are comparable.

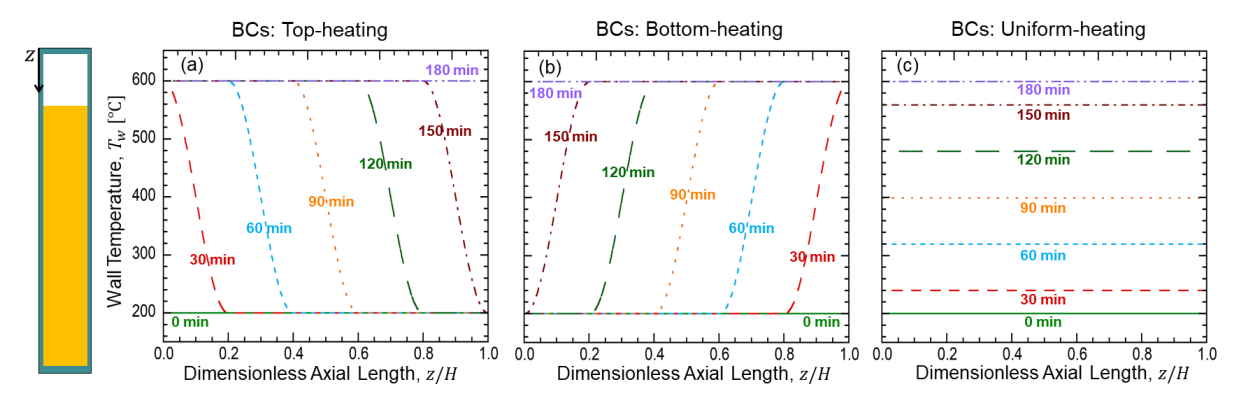


Figure 4.6. Imposed wall temperature for canonical boundary condition studies. (a) top-heating, (b) bottom-heating, (c) uniform-heating scenarios.

Figure 4.6 shows that imposed wall temperature at different time instants for these three cases. For the top-heating scenario, as shown in Figure 4.6(a), the wall temperature is a function of both time and non-dimensional axial length and is governed by the following expression:

$$T_{w}(z,t) \ [^{\circ}C] = \begin{cases} 200 & t \ [s] \le 9000z/H \\ 400 + 200 \sin \left[\frac{\pi}{1800}(t - 9000z/H - 900)\right] & t \ [s] \le 9000z/H + 1800 \\ 600 & t \ [s] > 9000z/H + 1800 \end{cases}$$
 (4.1)

The initial wall temperature is at 200 °C. At t = 30 min, the temperature of the top region, which is 0.2 meters long, reaches and stays at 600 °C. The subjacent 0.2-meter long region is heated from 200 to 600 °C and the rest of the wall is still at 200 °C. During the rest of the charging process, this 600 °C thermal front propagates from the top to the bottom until the temperature of the very bottom wall reaches 600 °C at t = 180 min. Afterward, the wall is held at 600 °C

As shown in Figure 4.6(b), the transient wall temperature boundary condition in the bottom-heating scenario is spatially symmetric to the top-heating scenario, thus ensuring the thermal front of 600 °C propagates from the bottom to the top. The expression of the wall temperature is:

$$T_{w}(z,t)[^{\circ}C] = \begin{cases} 200 & t [s] \leq 9000(1-z/H) \\ 400 + 200 \sin\left[\frac{\pi}{1800}(t + 9000z/H - 9900)\right] t [s] \leq 9000(1-z/H) + 1800 \\ 600 & t [s] > 9000(1-z/H) + 1800 \end{cases}$$
(4.2)

For the uniform-heating, the axial wall temperature boundary condition is shown in Figure 4.6(c) and equals the spatial average value of the wall temperature in the other two cases at any instant of time. Therefore, the wall temperature is only a function of time and the curve-fitted expression is:

$$T_{w}(t)[^{\circ}C] = \begin{cases} -3.82 \times 10^{-10}t^{3} + 6.29 \times 10^{-6}t^{2} - 5.62 \times 10^{-2}t + 200 & t[s] \le 10800 \\ 600 & t[s] > 10800 \end{cases}$$

$$(4.3)$$

The canonical boundary conditions for the three cases are completely controlled and comparable. Therefore, the comparison results could help further understand the significant distinctions among these three charging operations.

Figure 4.7 shows the temperature, streamlines, and velocity contours for the three scenarios. Similar to the experimental conditions, the imposed temperature stratification can be held well in the top-heating scenario, while the hot and cold sulfur are well mixed in the bottom-heating scenario. For the uniform-heating scenario, most convection currents are globalized along the tube, resulting in an accumulation of the hotter sulfur at the top region. For the top-heating scenario, as shown in Figure 4.7(a) and (d), there are approximately three regions within the sulfur during the charging process: the "heated", the "heating", and the "unheated" region. At the "heated" and "unheated" region, the sulfur temperature is $600\,^{\circ}$ C and $200\,^{\circ}$ C, respectively. The "heating" region is in between these two regions and the sulfur is being heated by the wall. At $t = 33\,$ min, the "heating region" is at the top and the natural convection also mainly occurs in this region. At $t = 100\,$ min, the top region has already been

heated to 600 °C and the "heating region" and the main convection cell have propagated to the middle of the tube. Later at t = 150 min, the convection cell and the "heating" region descends to the bottom.

For the bottom-heating scenario, as shown in Figure 4.7(b) and (e) both "heating region" (where the wall temperature is higher than the sulfur temperature) and "cooling region" (where the wall temperature is lower than the sulfur temperature) govern the heat transfer dynamics within sulfur. At t=33 min, the "heating region" is only at the bottom and the convection currents in this region are counterclockwise because the sulfur is heated by the wall and rises along the wall. The "cooling region" occupies the rest of the tube which results in the formation of clockwise convection currents. With the progression of thermal charge, the heating region expands from the bottom to the top while the cooling region shrinks and is restricted to the top region of the tube before gradually vanishing at the end of charge. The axial-velocity of buoyancy-driven flow for the bottom-heating scenario is around two orders of magnitude higher than it for the top-heating scenario, indicating the natural convection in the bottom-heating scenario is much more intense, as discussed in section 4.2.1.

The wall temperature is almost always higher than the sulfur temperature in the uniform-heating scenario. Thus, most of the convection currents are counter-clockwise and globalized within the sulfur during the thermal charge process. Since the sulfur viscosity decreases greatly with the temperature between 250 and 600 °C, the intensity of the natural convection increases from t = 33 to 150 min. Therefore, it can be observed that the global circulation starts to disintegrate into localized vortices at t = 150 min as shown in Figure 4.7(c) and the axial-velocity at t = 150 min is much higher than it at previous time instances from the velocity contours in Figure 4.7(f). In comparison to the top-heating scenario, the natural convection with a uniform wall temperature is of a much larger characteristic length and has a greater axial-velocity magnitude. However, compared with the bottom-heating scenario where the temperature difference between sulfur and tube wall is much higher, charging the tube uniformly results in lower axial velocity and weaker buoyancy-driven flow.

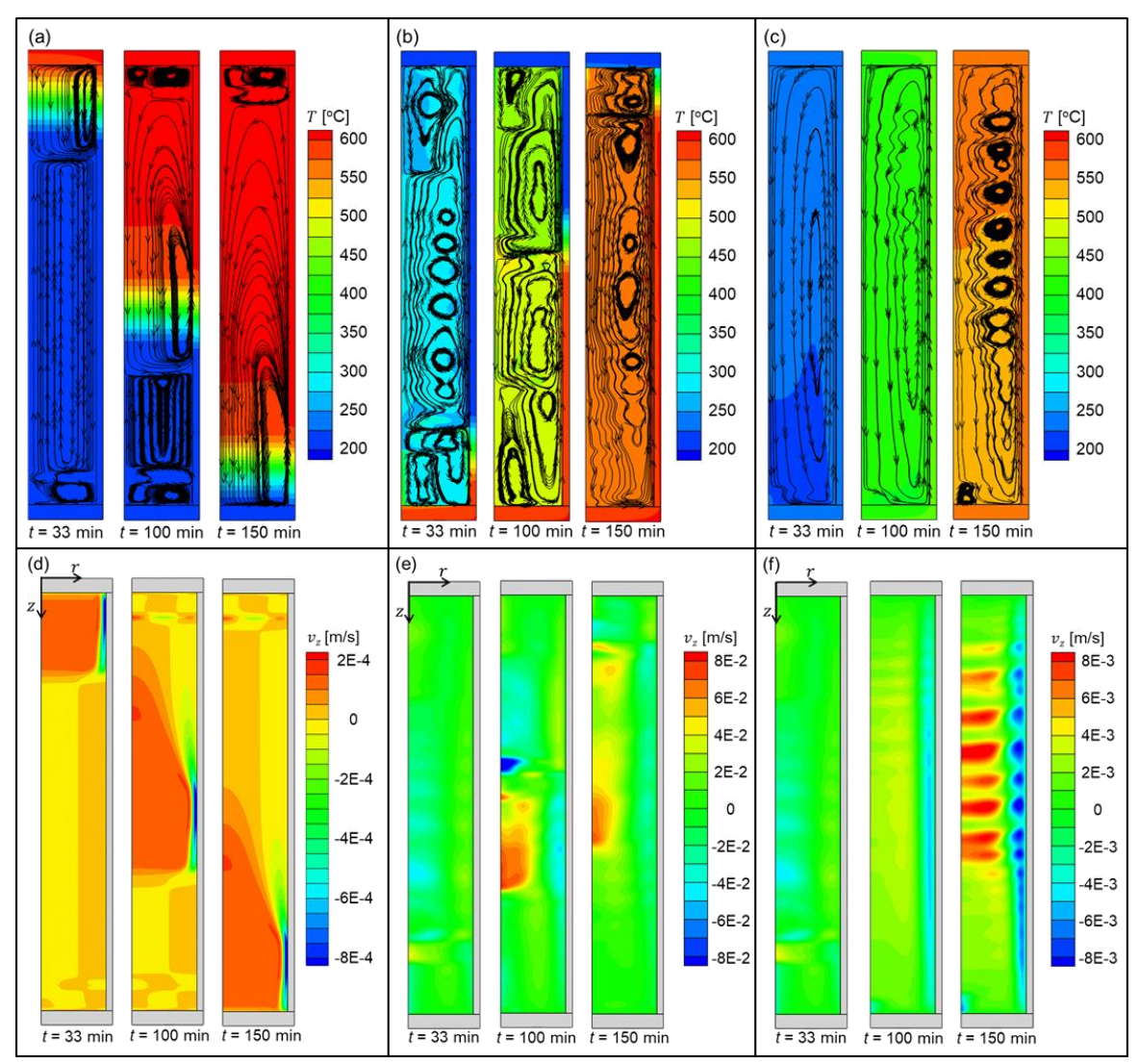


Figure 4.7. Contours of temperature and streamlines in the (a) top-heating, (b) bottom-heating, and (c) uniform-heating scenario; and contours of axial velocity (z-velocity) in the (d) top-heating, (e) bottom-heating, and (f) uniform-heating scenario for canonical charge study.

4.3. Heat transfer performance analysis

4.3.1. Energy and exergy analysis

To further elucidate the thermal performance of sulfur during both nonuniform charge conditions, the comparison of energy, exergy and their derivatives (charge rate) are shown in Figure 4.8. The charged energy is defined as:

$$E = \int_{T_{ref}}^{T_{sulfur}} m_{sulfur} c_{p,sulfur}(T) dT$$
 (4.4)

where the T_{sulfur} is the volumetric mean temperature of sulfur, T_{ref} is 200 °C, m_{sulfur} is 3.37 kg, and $c_{p,sulfur}(T)$ is the specific heat of sulfur, varying with sulfur temperature. In Figure 4.8(a), the energy charged in the bottom-heating scenario case is always higher than the other two cases for t < 150 min. After this time instant, the charge process is nearly complete as the energy stored in sulfur for all the cases asymptotes to the total energy capacity, which is around 1570 kJ. To study the characteristics of the energy variation, we calculate the energy charge rate by defining it as:

$$P_E = \frac{dE}{dt} \tag{4.5}$$

From Figure 4.8(b), in the first 50 minutes, the energy charge rate for the bottom-heating scenario is significantly higher than the other two cases. Afterward, this rate decreases and becomes lower than the other cases because of the temperature difference between the tube wall and sulfur, which drives the natural convection decreases. However, the overall energy charge performance in the bottom-heating scenario is still superior compared to the other two cases. Comparing the top-heating and uniform-heating scenarios, we find no significant difference in the transient evolution of energy stored or the energy charge rate between them. It indicates that the small-scale natural convection currents in the top-heating scenario and the global-scale currents in the uniform-heating scenario have similar impacts on the sulfur heat transfer. The previous study in section 3.3 has analyzed the relation between the heat transfer coefficient and the characteristic length of natural convection cases. Therefore, the effect of characteristic length on the heat transfer coefficient is very likely to be negative but not

very critical. It helps explain the reason that the top-heating scenario, which has a lower characteristic length, has a slightly better heat (energy) transfer rate than the uniform-heating.

In Figure 4.8(c) and (d), the charged exergy and its derivative are presented. The total charged exergy of sulfur is defined as:

$$\varepsilon^* = \int \rho \varepsilon (T) dV \tag{4.6}$$

$$\varepsilon(T) = u(T, p) - u_o(T, p) - T_o[s(T, p) - s_o(T, p)]$$
(4.7)

$$du = c_v(T)dT (4.8)$$

$$ds = c_v(T) \frac{dT}{T} \tag{4.9}$$

$$T_o = 200 \, ^{\circ}\text{C}$$
 (4.10)

For the top-heating scenario, it always has the highest charged exergy during the heating process because it holds the temperature stratification well. In the first 90 minutes, it also has the highest exergy charge rate. Though lower than the top-heating scenario, the exergy charge rate in the bottom-heating scenario is significantly higher than it in the uniform-heating. The convection currents in these two cases are all globalized and no thermal stratification can hold during the charging process. However, the bottom-heating scenario gains the energy faster and always has a higher volumetric mean temperature than the uniform-heating scenario does as shown in Figure 4.8(a).

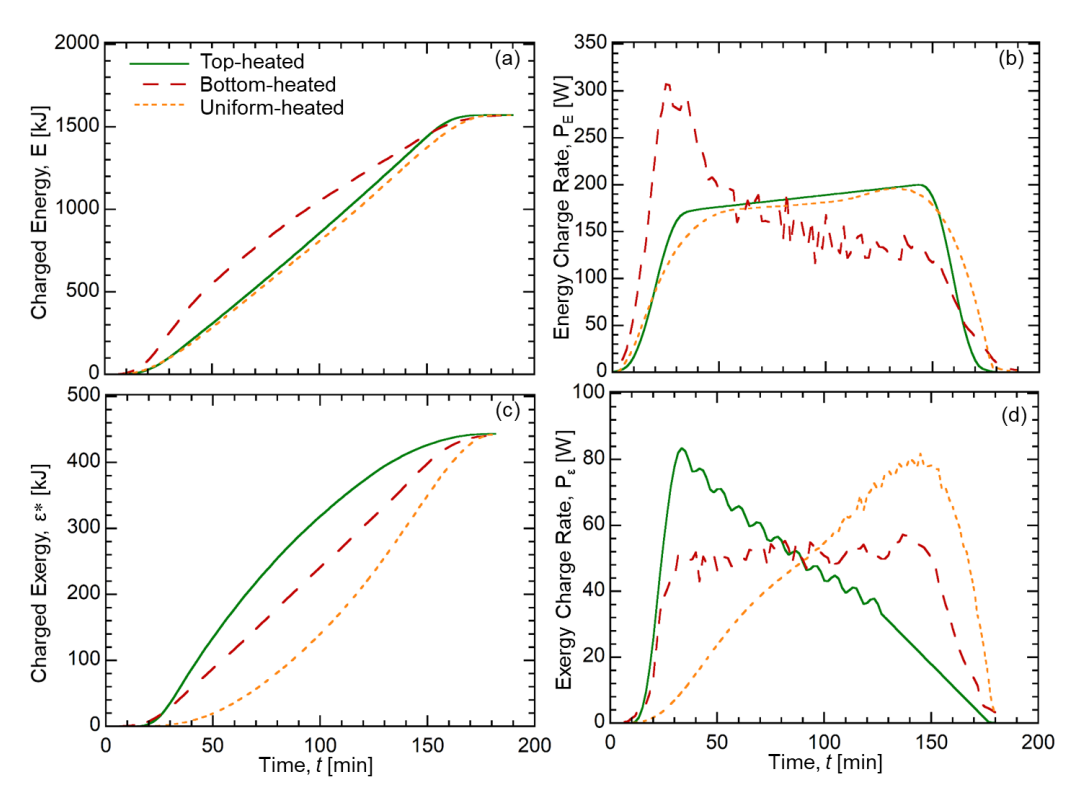


Figure 4.8. Temporal energy and exergy variations in the canonical boundary condition study: (a)energy variation, (b) energy charge rate variation, (c) exergy variation, (d) exergy charge rate variation.

The energy (and exergy) charge time is defined as the time between the moment that the charging process starts and the moment the charged energy (and exergy) reaches 90% of the energy storage capacity (around 1570 kJ) and the exergy storage capacity (around 440 kJ). Figure 4.9 shows the charge time for the top-, the bottom-, and the uniform-heating scenarios. From the energy perspective, the bottom-heating scenario always has the lowest charge time, indicating its energy charge performance is the best among the three cases. On average, the energy charge time of the bottom-heating scenario is 20% lower than the top-heating scenario and 23% lower than the uniform heated case, as shown in Figure 4.9(a).

In Figure 4.9(b), the exergy charge time for the three scenarios are compared and the top-heating scenario has the shortest exergy charge time, which is consistent with the results shown in Figure

4.8(c) and (d). The top-heating scenario showed 19% and 35% lower exergy charge time compared to the bottom-heating and the uniform-heating scenario, respectively. This indicates that charging the sulfur tube from the top can provide remarkable improvement to the exergetic performance of the system.

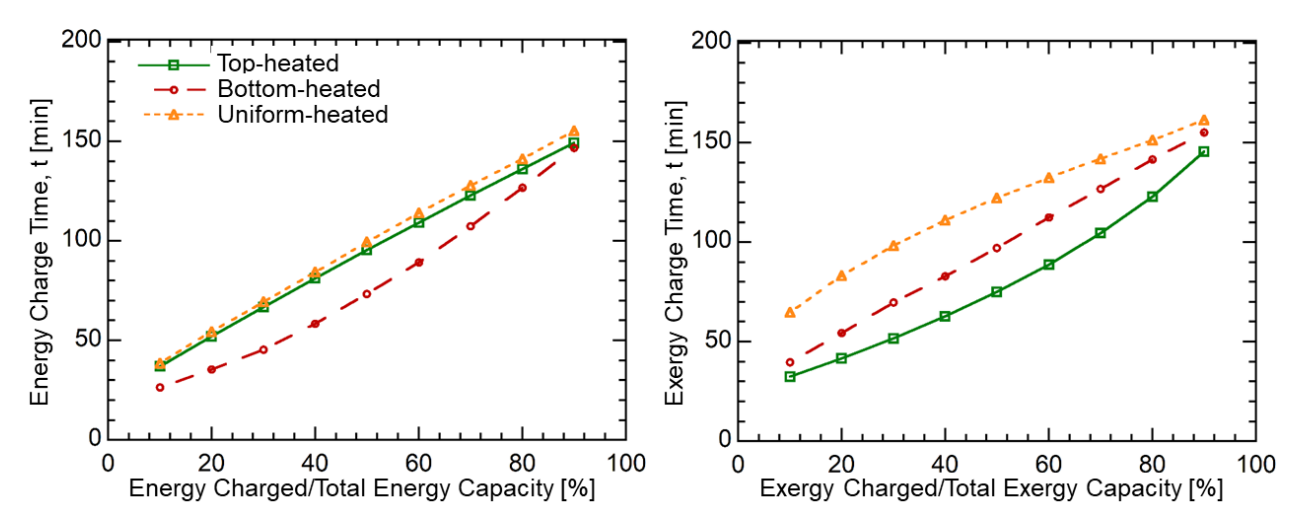


Figure 4.9. Charge time for the top-heating, bottom-heating, and uniform-heating scenarios: (a) energy charge time and (b) exergy charge time

The above results indicate that charging the system from the bottom to top could provide better energy charge performance while charging from top to bottom could provide better exergy charge performance. Compared with the uniform charge scenario, the bottom-heating charge has a 23% lower energy charge time and the top-heating charge has a 35% lower exergy charge time. Both non-uniform charging strategies could bring a significant improvement to the overall heat transfer performance for the SulfurTES system.

4.3.2. Simplified numerical methods

From the above studies, we have understood the main characteristics of top-heating and bottomheating charge cases for vertical sulfur storage tubes. However, the results introduced so far cannot be directly used for the system-level design because the heat transfer behavior of sulfur varies with tube size and the imposed charge and discharge patterns. For example, when a sulfur-filled tube is heated by top-heating, the height of the "heating" region, varying with tube height and wall temperature patterns, dominates the characteristic length of convection cells and thus has a great effect on sulfur energy and exergy charge rate. Therefore, to provide quantitative design bases for SulfurTES systems, we developed two simple analytical procedures (named as TOP and BOT procedure) to estimate the variation of sulfur temperature field, charged energy, and charged exergy for the system with various tube sizes and charge conditions.

TOP procedure

One of the advantages for the top-heating charge strategy is that the temperature stratification could be well held and thus provide a higher exergy storage capacity for SulfurTES storage tube. Therefore, for the system design, it is very critical to solve the transient axial sulfur temperature distribution in vertical tubes during the charge and then obtain the exergy charge rate. Instead of utilizing CFD tools, which is much more time consuming, we developed an analytical procedure named TOP procedure to provide accurate estimations for the transient sulfur temperature profile in different tubes.

In Figure 4.10(a), there are "heated", "heating", and "unheated" regions within the sulfur during the top-heating charge process, as discussed in section 4.2.2. To solve the axial temperature profile, we divide the sulfur domain in the axial direction into n small parts. For one small part located at $z = z_x$, the temperature of sulfur, $T_s(z_x, t)$ is assumed to be uniform and equal to the mass average temperature of this part. This temperature should follow the energy conservation shown in Equation (4.11):

$$\rho V c_p \frac{\partial T_S(z_x, t)}{\partial t} = q_w + q_{top} - q_{btm}$$
(4.11)

where $V = \pi D^2 H/4n$ is the volume of this small part, H is the tube height, and q_w is the heat flow rate from the wall. q_{top} and q_{btm} are the heat flow rate from (to) the adjacent parts. In this case, due to the opposite direction of buoyancy force and temperature gradient, the axial natural convection currents are localized and hence, we can neglect the axial heat flow q_{top} and q_{btm} . The heat flow rate from the wall, q_w , is derived in Equation (4.12).

$$q_{w} = hA_{w}[T_{w}(z_{x}, t) - T_{S}(z_{x}, t)]$$
(4.12)

where $A_w = \pi DH/n$ is the wall surface area of this part and $T_w(z_x, t)$ is the wall temperature, which is controlled as the boundary condition or can be solved together with sulfur temperature by coupling the energy conservation equation of the heat transfer fluid. h is the heat transfer coefficient and can be expressed as:

$$h = k \frac{Nu_{L_c}}{L_c} \tag{4.13}$$

By using the forward difference method, the numerical solution for the sulfur temperature can be derived as shown in Equation (4.14).

$$T_{S}(z_{x}, t + \Delta t) = T_{S}(z_{x}, t) + \frac{kA_{w}Nu_{L_{C}}}{\rho V c_{p}L_{C}} [T_{w}(z_{x}, t) - T_{S}(z_{x}, t)]\Delta t$$
(4.14)

Nusselt number, Nu_{L_C} can be obtained from Equation (4.25) as discussed in section 4.3.3. Characteristic length, L_c , is assumed to be the height of the "heating" region, which varies with imposed wall temperature patterns.

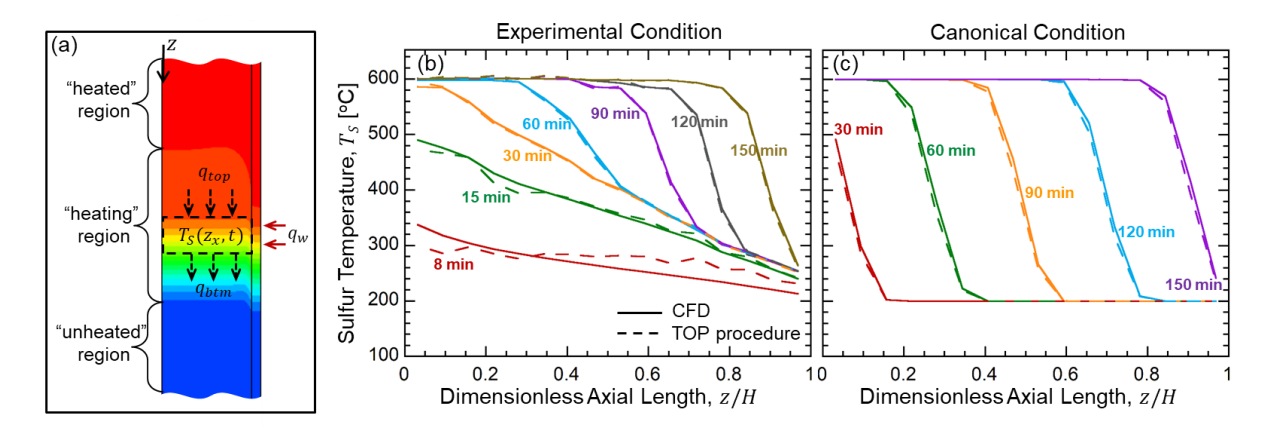


Figure 4.10. (a) Schematic of the sulfur tube under the top-heating condition. Comparison of CFD and TOP procedure results for the (b) experimental and (c) canonical cases.

To validate this solution, we compared it with the CFD results of the transient sulfur temperature profile for both experimental and canonical conditions, introduced in section 4.2.1 and 4.2.2. Figure 4.10(b) and (c) show the comparison results. The total number of the divided parts is n = 16. For the experimental condition, the height of the "heating" region is equal to the tube height (1m) at the first stage and becomes around 0.125 m at the second stage. Therefore, the characteristic length, L_c , also varies in the same manner. For the canonical boundary condition, L_c is 0.2 m during the whole charge process.

The average difference between the CFD and the numerical results is 3.8% and 3.0% for experimental and canonical cases, respectively. The good agreement between the two results provides confidence in the utility of the TOP procedure and relevant results.

BOT procedure

The other analytical procedure named as BOT procedure is developed to estimate the sulfur thermal performance during the bottom-heating charge process. For this charge scenario when the temperature gradient is imposed in the same direction as buoyancy force, the buoyancy-driven currents cause intense mixing of the hot and cold sulfur. Therefore, the temperature field of sulfur is closely

uniform and the axial temperature profile is no longer critical for the exergy analyses. In this procedure, we only solve the mass-average sulfur temperature, i.e. the sulfur temperature is only a function of time. This average sulfur temperature, $T_S(t)$, should satisfy the energy conservation equation:

$$\rho V_{tot} c_p \frac{\partial T_S(t)}{\partial t} = q_w \tag{4.15}$$

where V_{tot} is the total volume of sulfur in the tube. As mentioned in section 4.2.2, the sulfur domain consists of a "heating" and a "cooling" region since the wall temperature is higher than the sulfur temperature at the bottom but is lower than the sulfur temperature at the top. Therefore, we divide the tube wall into n small parts and the wall temperature for each part is assumed to be uniform and equal to the surface average wall temperature for this part, as shown in Figure 4.10(a). The interface between the "heating" and "cooling" region, where wall temperature is equal to average sulfur temperature, is assumed to be at $z = z_k$. During the charge process, this interface moves from the bottom to the top of the tube. Then the heat flux, $q_w''(z,t)$ and the total heat flow rate, $q_w(t)$ from the wall can be expressed as shown in Equation (4.16) and (4.17), respectively:

$$q_{w}^{"}(z,t) = \begin{cases} h_{d}[T_{w}(z_{1},t) - T_{S}(t)] & 0 < z \leq z_{1} \\ h_{d}[T_{w}(z_{2},t) - T_{S}(t)] & z_{1} < z \leq z_{2} \\ \vdots & \vdots & \vdots \\ h_{d}[T_{w}(z_{x},t) - T_{S}(t)] & z_{k-1} < z \leq z_{x} \end{cases} \text{"cooling" region}$$

$$h_{c}[T_{w}(z_{x+1},t) - T_{S}(t)] & z_{k} < z \leq z_{k+1}$$

$$h_{c}[T_{w}(z_{x+2},t) - T_{S}(t)] & z_{k+1} < z \leq z_{k+2} \\ \vdots & \vdots & \vdots \\ h_{c}[T_{w}(z_{n},t) - T_{S}(t)] & z_{n-1} < z \leq z_{n} \end{cases} \text{"heating" region}$$

$$(4.16)$$

$$q_w(t) = \iint q_w''(z,t) \, dA = A_w \sum_{i=1}^n q_w''(z_i,t) \tag{4.17}$$

where A_w is the wall surface area for each part, and h_c and h_d are the charge and discharge heat transfer coefficient and can be derived from Equation (4.18) and (4.19), respectively.

$$h_c = k \frac{Nu_{L_{c,c}}}{L_{c,c}} \tag{4.18}$$

$$h_d = k \frac{N u_{L_{c,d}}}{L_{c,d}} (4.19)$$

Nusselt number, $Nu_{L_{c,c}}$ and $Nu_{L_{c,d}}$, can be found in Equation (4.25) and (4.26) in section 4.3.3. The characteristic lengths in this case should satisfy the following relationship:

$$L_{c,c} + L_{c,d} = H (4.20)$$

where $L_{c,c}$ varies from 0 to H during the charge process. With the forward difference method, the numerical solution for the average sulfur temperature is:

$$T_S(t + \Delta t) = T_S(t) + \frac{q_w(t)}{\rho V_{tot} c_p} \Delta t \tag{4.21}$$

In consideration of the good uniformity of the axial sulfur temperature profile in bottom-heating scenario (due to the intense mixing between the hot and cold sulfur), we assume that the sulfur temperature at any axial location is identical and equivalent to the average sulfur temperature, $T_S(t)$. The comparison of the sulfur temperature profile with the CFD results is shown in Figure 4.11(b) and (c). The average differences between the two results are 7.6% and 5.1% for experimental and canonical boundary conditions, respectively. The prediction accuracy is slightly less than the TOP procedure but still within the desired level of accuracy to use it for the design of SulfurTES systems based on energy and exergy performance analysis.

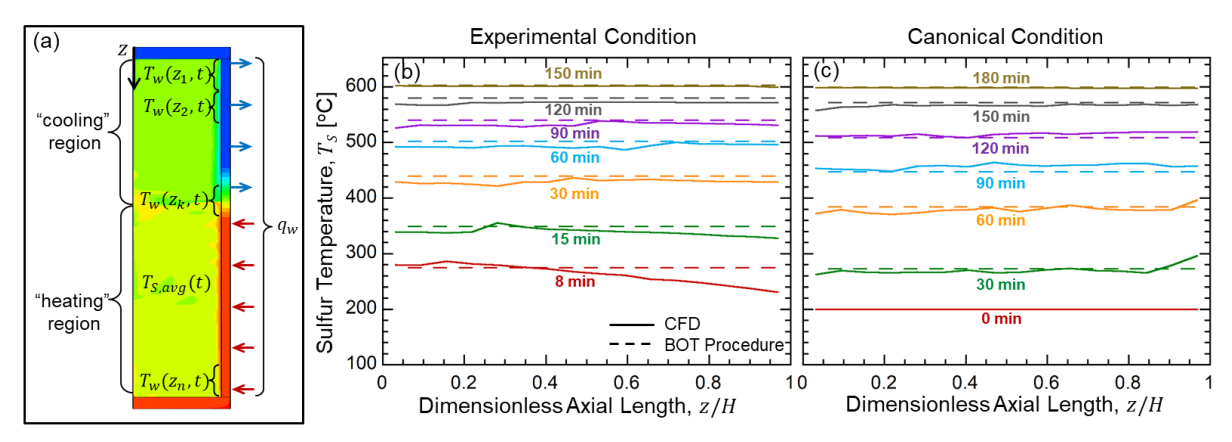


Figure 4.11. (a) Schematic of the sulfur tube under the bottom-heating charge condition.

Comparison of CFD and the BOT procedure results for the (b) experimental and (c) canonical cases.

Energy and exergy analyses

Based on the results of temperature variation, we derived the energy and exergy variation as defined in section 4.3.1 and compared them with the CFD results, as shown in Figure 4.12. The errors from the TOP and the BOT procedure are calculated and shown in Table 4.1, indicating that both procedures work well in predicting the thermal performance of vertical sulfur storage tubes.

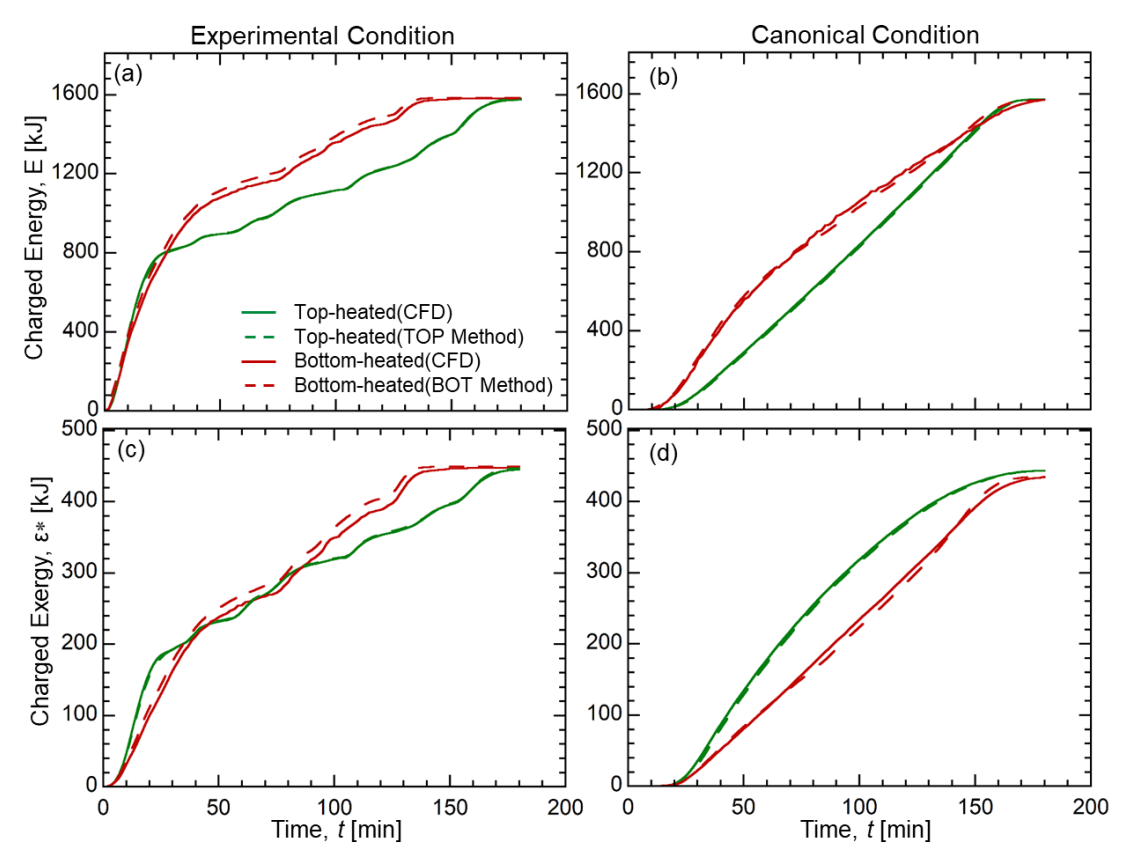


Figure 4.12. Transient variation of (a) charged energy in the experimental cases and (b) the canonical cases; transient variation of (c) charged exergy in the experimental cases and (d) the canonical cases.

Table 4.1. Errors for TOP and BOT procedures on predicting energy and exergy variation

Experimental condition				Canonical condition				
Energy		Exergy		Energy		Exergy		
TOP	ВОТ	TOP	BOT	TOP	ВОТ	TOP	ВОТ	
1.1%	3.8%	0.8%	5.3%	2.2%	2.7%	2.9%	4.3%	

In addition to the energy and exergy analyses for sulfur storage tubes, the TOP and BOT procedures can also be utilized in system-level studies and designs. These two procedures can be readily coupled to system-level numerical models, as introduced in ref. [80-82] to solve for temperature field in the system and estimate the system-level thermal performance (e.g. system energy efficiency, exergetic efficiency, etc.). Moreover, to predict the thermal performance for the discharge process or

for the TES system with other storage fluids, researchers can also follow this section and develop similar analytical procedures.

4.3.3. Nusselt number correlation

In this section, we are going to further discuss how to obtain the Nusselt number in Equation (4.14), (4.18), and (4.19).

From the previous study in Chapter 3, we have discussed that the Nusselt number for sulfur natural convection should satisfy the following forms

$$Nu_{L_c,avg} = C \cdot Ra_{L_c,avg}^m \tag{4.22}$$

Where C and m are the constants varying with system configurations. The average Rayleigh number, $Ra_{L_C,avg}$, is defined as:

$$Ra_{L_c,avg} = \frac{g\beta (T_w - T_S)_{avg} L_c^3}{\sigma v}$$
(4.23)

In addition, we also obtained and validated the value of constants for the vertical tube system in the range of characteristic length, L_c between 0.5 and 3 m in section 3.3.1. For the charge scenarios, C = 0.245 and m = 0.314. For discharge scenarios, C = 0.337 and m = 0.274.

However, for top-heating and bottom-heating scenarios discussed in this study, L_c can be much smaller than 0.5 m (e.g. in the canonical case introduced in section 4.2.2, $L_c = 0.2$ m). Therefore, we conducted another parametric study to obtain the Nusselt number correlations for between 0.1 and 0.5 m under both charge and discharge conditions. The natural convection of sulfur between 200 to 600 °C for the configurations with 15 parameters is studied, with the height of tube (characteristic length) as 0.1, 0.2, ..., 0.5 m and the diameter as 5.5, 10.8, and 21.2 cm. Figure 4.13 shows the average Nusselt number and Rayleigh number for charge and discharge scenarios.

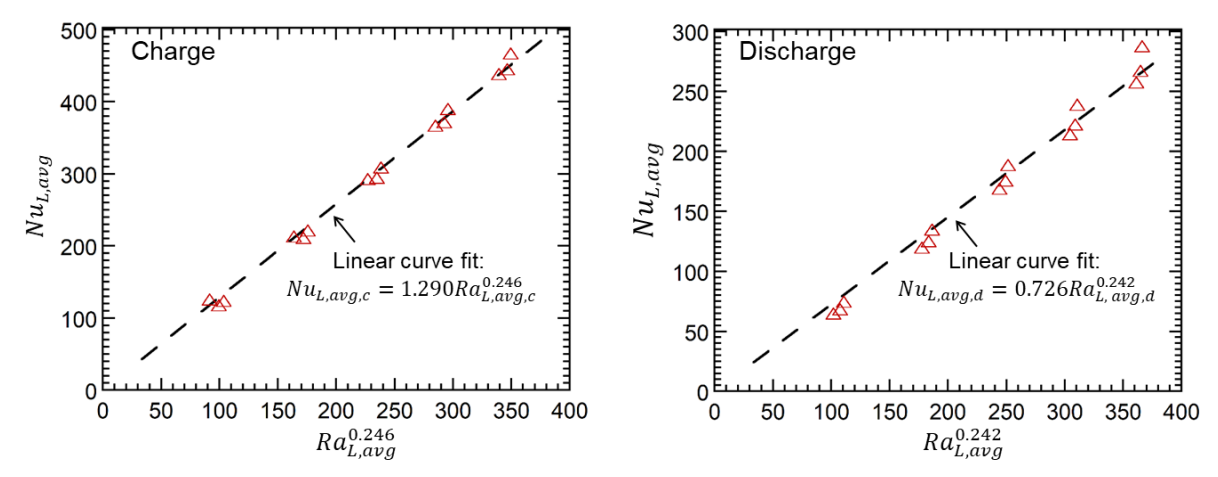


Figure 4.13. Variation of average Nusselt number with average Rayleigh number for (a) charge condition and (b) discharge condition for a tube length between 0.1 and 0.5 m.

For the TOP and BOT procedures, we assume that these correlations are true for the whole charge process and then we can express Rayleigh number as a function of temporal sulfur and wall temperatures:

$$Ra_{L_c} = \frac{g\beta [T_w(t) - T_S(t)]L_c^3}{\alpha \nu}$$
(4.24)

Then the Nusselt number can be obtained from the following equations:

Charge (c):

$$Nu_{L_{c,c}} = \begin{cases} 1.290Ra_{L_{c,c}}^{0.246} & 0.1 < L_{c,c} < 0.5 m\\ 0.245Ra_{L_{c,c}}^{0.314} & 0.5 < L_{c,c} < 3 m \end{cases}$$
(4.25)

Discharge (d):

$$Nu_{L_{c,d}} = \begin{cases} 0.726Ra_{L_{c,d}}^{0.242} & 0.1 < L_{c,d} < 0.5 m\\ 0.337Ra_{L_{c,d}}^{0.274} & 0.5 < L_{c,d} < 3 m \end{cases}$$
(4.26)

4.4. Conclusions

This study investigates the characteristics of sulfur heat transfer in a vertically-orientated container under nonuniform thermal charge conditions (i.e., top-heating and bottom-heating). We developed a

deep understanding of the dominate natural convection phenomena for liquid sulfur with both experimental and validated computational studies. The current study is a first of its kind and provides critical quantitative and qualitative design bases for SulfurTES systems that employ sulfur isochorically contained and nonuniformly heated in vertically-oriented tubes.

For top-heating, there form three distinctive regions (i.e., heated, heating, and unheated regions) during thermal charge. The system can exhibit very attractive exergy charge performance because a thermal stratification forms within the sulfur and is well maintained during the charging process. In contrast, bottom-heating has a heating and a cooling region at bottom and top, respectively and exhibits higher energy charge rate due to a good mixing between the cold and the hot sulfur. In the comparison between top-, bottom-, and uniform-heating for 1-meter long and 5.5-cm diameter sulfur tube, top-heating provides superior exergy charge performance with exergy charge times 19% and 35% lower than the bottom- and uniform-heating, respectively. For energy charge rates, bottom-heating provides superior performance with a minimum energy charge time that is typically 20% lower than the top-heating and 23% lower than uniform-heating. Therefore, compared to uniform-heating, both nonuniform charge strategies (top- and bottom-heating) have unique advantages for SulfurTES systems.

By using N_H number correlations from the numerical results, this article also introduces two simple analytical procedures to estimate the energy and exergy charge performance for top-heating and bottom-heating with various system length scales and charge scenarios. In addition to the SulfurTES system, these procedures are generally applicable to the analysis of buoyancy-induced flow transport for isochoric thermal TES with any liquid-state storage materials. Furthermore, system designers can use these procedures to predict system-level thermal performance and select the appropriate charge/discharge strategies.

Chapter 5

Sulfur heat transfer behavior in bath-configuration TES systems

Inspired by the bottom-heating charge in the SulfurTES with vertical-tube configuration, the system with heat resources from the bottom can potentially provide a superior energy charge rate. Therefore, a new design named as SulfurTES bath system was proposed to pursue further optimizations for the system thermal performance. This system is still analogous to the shell-and-tube heat exchanger, however, the sulfur is stored in the shell and the heat transfer fluid flows through the bottom charge tubes or top discharge tubes, as shown in Figure 5.1. In comparison to the horizontaltube configuration, this design can introduce the bottom-heating effect and help improve system thermal charge rate. Furthermore, unlike the vertical tube-configuration system where a cooling region exists under the bottom-heating charge condition, the sulfur in the bath system will lose less heat and be better charged by the heat transfer fluid. Therefore, this system design can potentially provide higher heat transfer rate or demand fewer tube materials than tube-configuration systems. Affected by multiple geometric parameters, the natural convection physics in the current bath system can be very complex and need to be better understood. The objective of this study is to investigate the sulfur heat transfer behavior in the SulfurTES bath system from 200 to 600 °C and quantify the heat transfer rate. The CFD models similar to it introduced in Chapter 3 and Chapter 4 are developed and used for parametric study.

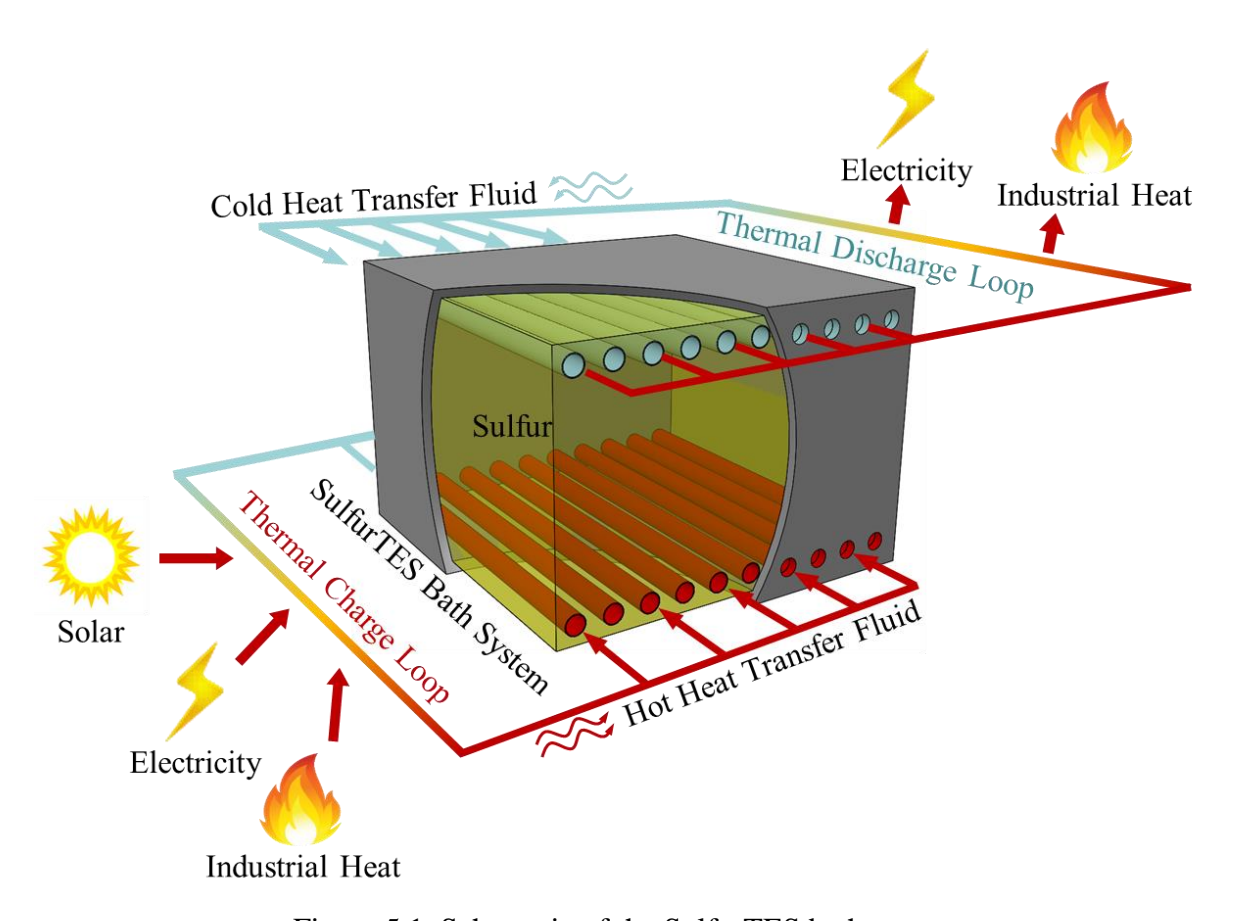


Figure 5.1. Schematic of the SulfurTES bath system.

5.1. CFD study

5.1.1. Model development

In the SulfurTES bath system, as shown in Figure 5.1, the charge tubes are uniformly arranged at the bottom region of the system and the discharge tubes are symmetrically installed at the top. The heat transfer fluid enters the system from one end of the tube to thermally charge and discharge the sulfur. The natural convection in the real bath system can be three-dimensional as shown in the left schematic from Figure 5.2, and the relevant physics are affected by many geometric factors, such as the system dimension and tube sizes. Among these factors, the tube sizes should dominate the natural convection since it serves as the foundation of the thermal boundary layer. Given the tube length (at the magnitude of 1 meter) is usually much higher than the tube diameter (at the magnitude of 1 cm),

the temperature gradient within the thermal boundary layer along the tube axis can be neglect compared to it in the radial direction. Therefore, the phenomenon can be simplified to be the 2-D natural convection over tube arrays, as shown in the right schematic in Figure 5.2.

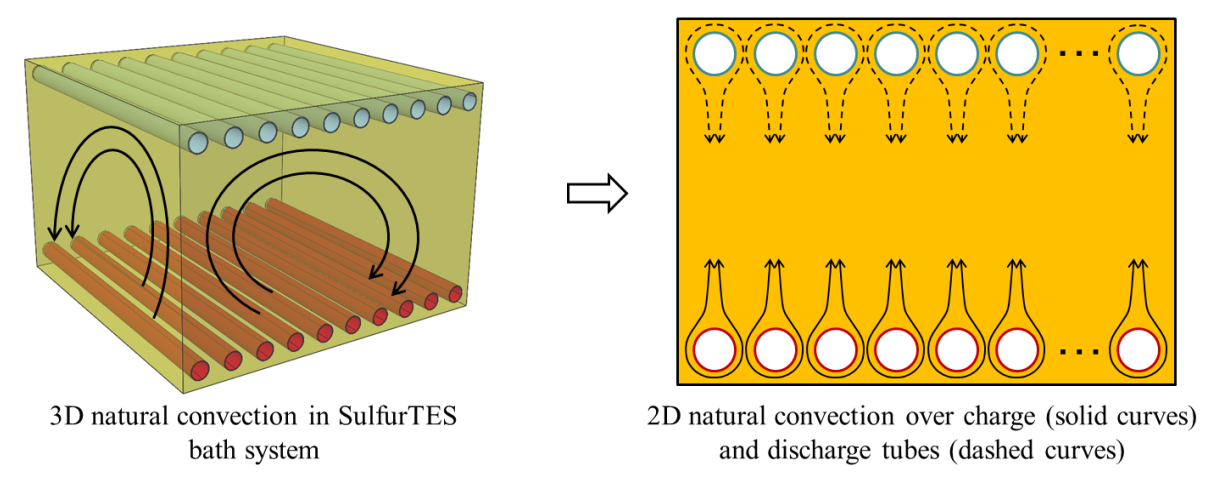


Figure 5.2. Schematic of natural convection in SulfurTES bath system

Governing Parameters

All the geometric parameters including system width, W, system height, H, tube diameter, D, tube pitch ratio, p, the distance between the adjacent tubes, δ , and the distance between the tubes and the bottom wall, d, might affect the heat transfer behavior of the sulfur and are shown in Figure 5.3. W is governed by p, D, and the number of the tubes, N, in fthe orm of: $W = N \cdot pD$. δ is proportional to both p and p and can be expressed as p and p and p and p and p and p and p are assumed that p and p are assumed that p are assumed that p and p are assumed that p and p are assumed that p and p are assumed to the properties p and p are asumed to the properties p and p are asumed to the properties p and p are asumed to t

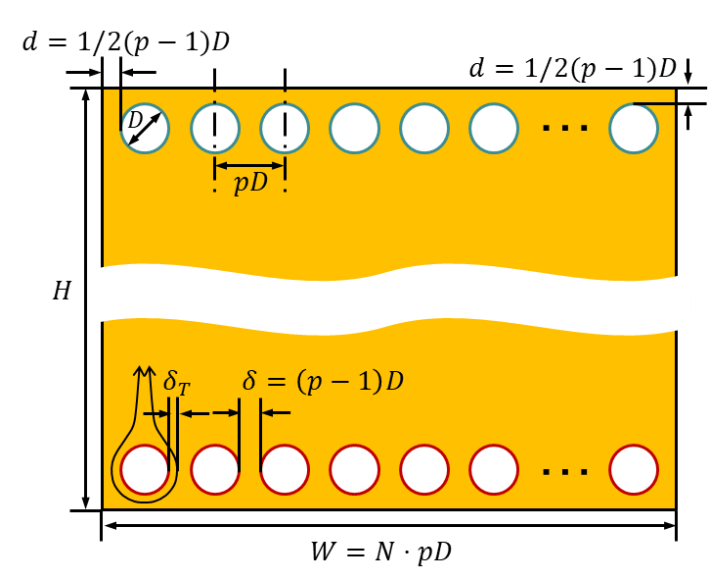


Figure 5.3. 2D computational domain of SulfurTES bath system with primary geometric parameters

During the thermal charge process, the convection currents form from the bottom of each tube and rise along the tube wall to the top of the system. For the discharge scenario, the convection currents form around the top tubes symmetrically. Since the convection currents onsets over the charge or discharge tubes, the tube diameter, D, characterizes the natural convection phenomena and cast a significant impact on the heat transfer behavior for most scenarios in this study. The thickness of thermal boundary layer for the convection phenomenon is set as δ_T and can be expressed as shown in Equation (5.1) based on the scaling analysis in ref [52].

$$\delta_T \sim D \cdot R a_D^{-\frac{1}{4}} \tag{5.1}$$

Apart from D, $\delta = (p-1)D$ can be the secondary dominant parameter affecting the thermal boundary layer formation in comparison to the other geometric parameters. When $\delta \gg \delta_T$, the convection currents of each tube won't interfere with each other and the heat transfer behavior is close to the typical natural convection over horizontal cylinders and the heat transfer rate is only dominated by Ra_D . When $\delta \sim \delta_T$, the buoyancy-driven currents over each tube will be more or less

impeded by the adjacent tubes and the heat transfer rate will also be affected by δ (or more accurately, p), in addition to Ra_D . When $\delta \sim 0$ (or p=1), the boundary layer over each tube will be combined and the natural convection behavior is similar to it in a square enclosure with bottom heating (top cooling). Nevertheless, the bottom half of the tube surface area is ineffective for heat transfer in this extreme condition which will cause that the overall heat transfer rate to be much lower than the large- δ scenarios. In practical, δ will be larger than 0 (or p > 1) and the convection currents form along the entire external surface for each tube to guarantee the effective charge or discharge of the bath system. Other geometric parameters, such as H and $W = N \cdot pD$, which are usually much larger than the characteristic tube diameter, should not significantly but might still cast some effect on the heat transfer behavior. The details will be discussed in later sections.

According to the heat exchange design book [83], the tube diameter in a normal heat exchanger is usually in the range of 5 to 40 mm. For the tube pitch ratio, it is usually smaller than 3 to guarantee a sufficient thermal charge rate. Therefore, we set $5 \text{ } mm \leq D \leq 40 \text{ } mm$ and $1 \leq p \leq 3$ as the design space for the SulfurTES bath system. The maximum value of average Rayleigh number, $Ra_{D,avg}$, with the sulfur temperature varying from 200 to 600 °C, was calculated to be 1.6×10^7 for the sulfur in the system with D = 40 mm. Based on ref. [84], the buoyancy driven flow is at the laminar regime when $Ra_{D,avg} \leq 10^7$. Therefore, the laminar model, same as the study in Chapter 3 and Chapter 4 was used in this study.

Mesh size refinement and time-step study

To ensure the accuracy of the CFD results, a mesh size study was conducted to eliminate the dependency between the grid size and the computational data. In general, the critical mesh size is determined by minimum characteristic sizes for the heat transfer phenomena, such as the boundary layer thickness, δ_T , and the distance between two adjacent tubes, δ , which are proportional to D and

pD, respectively. Therefore, D = 5mm and p = 1.25 (which are close to the minimum values in the design space) are selected for this grid size refinement study. The other geometric parameters are set as H = 25D and N = 2. The charge tube temperature and the initial sulfur temperature is controlled 600 and 200 °C, respectively. The mesh for sulfur domain was controlled to be quadrilateral and was refined near the wall of the charge (and discharge) tubes, as shown in Figure 5.4(a). Five cases with the average mesh size (total domain area divided by the number of grids) of 2.0, 1.0, 0.5, 0.25 and 0.125 mm² were simulated in this study. The variation of average sulfur temperature, $T_{S,avg}$, and heat flux, q_w , from the tube were monitored at each second. The heat transfer coefficient was calculated based on the expression: $h = q_w/(T_{w,c} - T_{S,avg})$. Figure 5.4(b) and (c) shows the variation of average sulfur temperature and the heat transfer coefficient, respectively. The difference for the heat transfer coefficient between the two consecutive mesh sizes (i.e., 2.0 vs. 1.0 mm², 1.0 vs. 0.5 mm², etc.) are 4.0%, 3.2%, 2.4%, and 0.7%, respectively. Since the error converges with the mesh density increasing, the mesh size of 0.25 mm² was selected based on the trade-off between the increase in the accuracy of the numerical simulation results and the increase in computational cost.

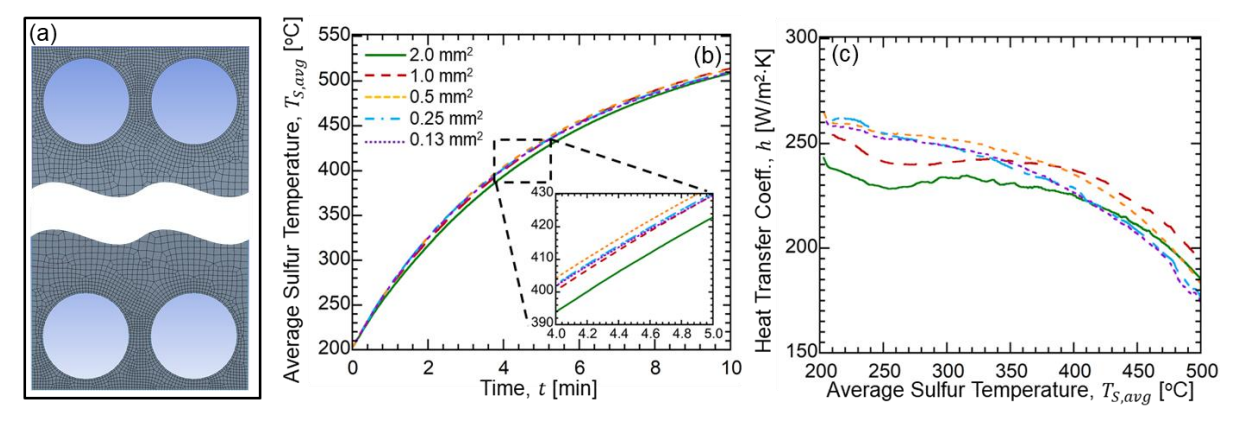


Figure 5.4. (a) Computational mesh for sulfur domain and variation of (b) average sulfur temperature and (c) heat transfer coefficient in grid size refinement study.

In the time-step study, three cases with time steps 0.2 s, 0.1 s, and 0.05 s are investigated and the differences for the variation of both temperature and heat transfer coefficient were much smaller than 0.1%. Finally, the time step of 0.1 s was used for further simulation studies.

Model Validation

From the previous studies in Chapter 3 and Chapter 4, the temperature-dependent properties of sulfur have already been fully validated. In this study, the reliability of the model mainly relies on the accurate prediction of the natural convection in these specific geometries. As the current convection physics is similar to the typical natural convection over a horizontal cylinder from many reported canonical studies, the current CFD model is modified based on the typical physics and the relevant simulation results are compared with the empirical correlations developed by Morgan [84] (Equation 5.1) and Churchill and chu [85] (Equation 5.2) in 1975 to prove its validity.

Morgan:
$$Nu_D = \begin{cases} 0.850Ra_D^{0.188} & 10^2 < Ra_D < 10^4 \\ 0.480Ra_D^{0.250} & 10^4 < Ra_D < 10^7 \end{cases}$$
 (5.1)

Churchill and Chu:
$$Nu_D = \left\{0.60 + \frac{0.387Ra_D^{1/6}}{\left[1 + (0.559/Pr)^{9/16}\right]^{8/27}}\right\}^2$$
 $Ra_D \le 10^{12}$ (5.2)

Both correlations are valid for an isothermal horizontal cylinder within the liquid with an infinite large volume (the increase of average temperature of fluid is negligible). To simulate this phenomenon, the four edges of the sulfur domain was controlled at the initial fluid temperature, T_i , in this model, as shown in Figure 5.5(a). We studied the thermal charge scenarios for air with D=5,20, and 40 mm, H=25D and p=3. The initial temperature was $T_i=77 \, ^{\circ}\text{C}$ and the charge wall temperature was $T_w=177 \, ^{\circ}\text{C}$. During the simulation process, the average liquid temperature, $T_{l,avg}$, and the wall heat flux, q_w , were calculated and monitored until they entered steady-state (variations are smaller than 1% per minute). Nu number was obtained based on the final liquid temperature,

 $T_{l,avg,f}$, and wall heat flux, $q_{w,f}$, in the following equation (all the material properties is interpolated based on the average of $T_{l,avg,f}$ and T_w :

$$Nu_{D} = \frac{hD}{k} = \frac{q_{w,f}D}{k(T_{w} - T_{l,avg,f})}$$
 (5.3)

The comparison results are shown in Figure 5.5(b) and the average errors between the computational (CFD) results and the two correlations from Morgan and Churchill el al. are 6.4% and 2.2%, respectively. The good agreement provides further confidence in the model for later study.

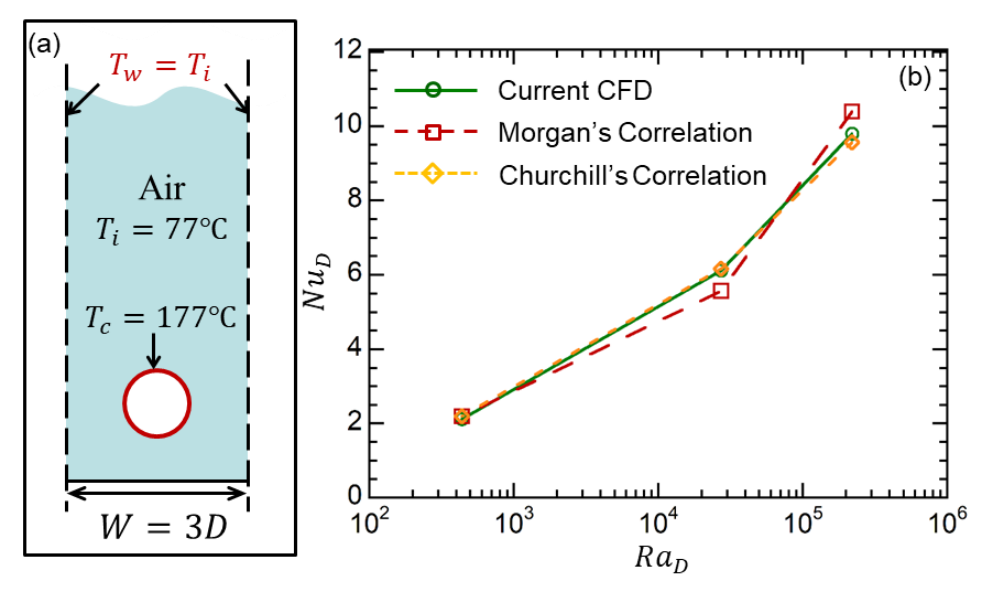


Figure 5.5. (a) Schematic of the CFD model with modified settings and (b) comparison between the results from this CFD model and the previous empirical correlations.

5.1.2. Parametric study

In the current computational domain, as shown in Figure 5.3, there are 4 independent governing parameters including N, H, D, and p, of which the variation might cast influences on the heat transfer coefficient. A number of parametric studies were conducted to understand and quantify the effect of each parameter.

Effect of the number of tubes

In practice, there could be tens or hundreds of tubes in one bath systems and the direct simulation will require an extremely high computational cost. Therefore, the symmetry assumptions are made in this study to significantly decrease the size of the computational domain, as shown in Figure 5.6. We set D = 5 mm, H = 25 D, p = 1.25, and N from 1 to 10. Two cases with different symmetric domains (1Tube-Domain-01 and 1Tube-Domain-02) were simulated for N = 1 cases. The two sidewalls for all the models were symmetric plane and the initial sulfur temperature and the charge wall temperature was 200 °C and 600 °C, respectively. For the domain with large N, it should provide more accurate simulation results because it is closer to the real-world multiple-tube bath systems. However, the computational cost for the CFD model will significantly increase with N increasing. Therefore, in addition to understand the effect of tube numbers, we also need to determine an appropriate N to for sufficient simulation accuracy but low computational cost.

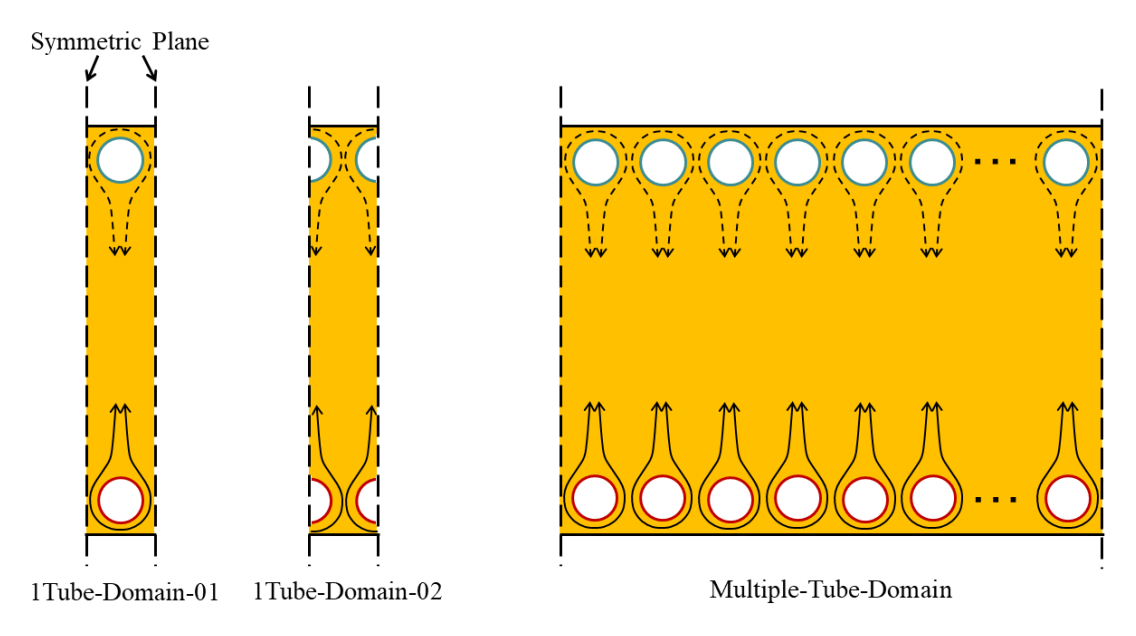


Figure 5.6. Schematic of the computational domains with single and multiple tubes.

Figure 5.7(a) shows the temperature and the streamlines contours for all the domains when the average sulfur temperature reaches around 300 °C for all the cases. For the multiple-tube domains (2-, 5-, and 10-Tube Domains), it can be observed that the flow and temperature fields along each tube are asymmetric due to the effect of the narrow space between the adjacent tubes. Thus, they are different from the contours for both single-tube domains. The variations of average sulfur temperature and heat transfer coefficient, h, shown in Figure 5.7(b) also agree with this observation and indicate that the 1Tube-domain-01 overestimates while the 1Tube-domain-02 underestimates the heat transfer rate in comparison to all the multiple-tube domains. However, among the multiple-tube domains, the curves of h are very close to each other. The first row of data in Table 5.1 shows the average heat transfer coefficient from 200 to 550 °C for all these domains. The difference for h between the 2Tube- and 10Tube-Domain is less than 3%, indicating that the results from the 2Tube domain can be sufficiently accurate to quantify the heat transfer rate of sulfur in the bath system.

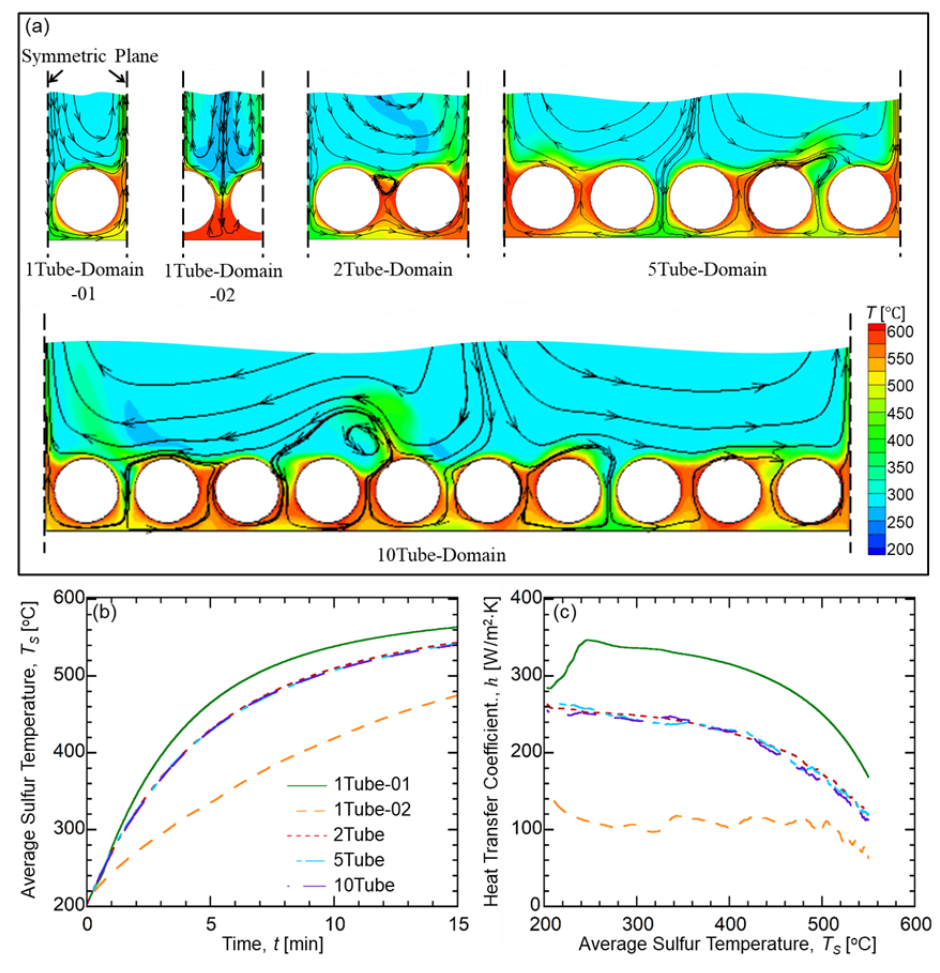


Figure 5.7. (a) Temperature and streamlines contours, (b) variation of the average sulfur temperature, and (c) variation of the heat transfer coefficient in the charge scenarios for the single and multiple-tube domains.

Table 5.1. Average heat transfer coefficient (from 200 to 550 °C) for various computational domains (Unit: W/m²·K)

	1Tube- Domain-01	1Tube- Domain-02	2Tube- Domain	5Tube- Domain	10Tube- Domain
D = 5 mm, p = 1.25	300	168	226	223	221
D = 5 mm, $p = 3$	406	423	413	419	424
D = 20 mm, p = 1.25	260	241	262	256	251

More simulations with D = 5 mm, p = 3, and D = 20 mm, p = 1.25 are conducted to investigate the effect of N and the feasibility of the 2Tube domain for different size systems. From Table 5.1, we found that the differences in the average heat transfer coefficient among all the mentioned domains (two single-tube and all multiple-tube domains) are less significant than the previous case. In the case with D = 5mm, p = 3, for instance, the overall heat transfer coefficients for all the mentioned domains are very close and the relative differences are within 5%. A similar observation is made for D=20 mm, p=1.25 case. Based on Equation 5.1, $\delta/\delta_T \sim (p-1)Ra_D^{1/4}$ which is proportional to D and p, shows that the natural convection over one tube with smaller D and p is more likely to be affected by the adjacent tubes. This effect can result in the nonuniform temperature and flow field and cannot be accurately simulated by the 1Tube-Domains. For the cases with larger D or p, the charge tubes will cast less impact on each other and therefore the convection currents over the charge tubes are steadier and more symmetrical. This could explain why the simulation results from the single- and multiple-tube domains are quite different when D =5 mm, p = 1.25, but very close to each other when D = 5 mm, p = 3, and D = 20 mm, p = 31.25.

Since the cases with small D and p (e.g. D = 5 mm, p = 1.25) belong to the design space for this study, it is not acceptable to conduct the simulations with either of the single-tube domains. But fortunately, the results in the 2Tbue-Domain agree well with the simulations in 5- and 10Tube-Domains for various D and p. Therefore, the 2Tube-Domain will be utilized in later studies to provide accurate CFD results with relatively low computational costs.

Effect of the system height

Since the main potential advantage of the bath configuration system is the less tube cost, the system height is practically much larger than the tube diameters. In this section, we investigate the effect of H on the thermal charge performance for the range from 12.5D to 50D.

The scenario with D = 5mm, p = 1.25 is studied first. As shown in Figure 5.8(a). the temperature and streamlines for the system with H = 12.5, 25, and 50D are contoured at the time instance when sulfur average temperature reaches around 300 °C. For the H = 12.5D case, the sulfur at the bottom region is heated by the charge tubes at bottom and rises up to the top region due to the buoyancy effect. The height of the buoyancy-driven currents is of the same magnitude as the distance between the charge and discharge tubes. The hot and cold sulfur in this region is well mixed and the temperature field in this region is therefore near uniform. For H=25D, the height of the convection currents also increases and there is a split at the top that forms a small convection cell with the opposite spinning direction to the main cell. In the case with H = 50D, since H is way higher than the other two cases and more convection cells are split from the main cell. Despite the sizes and numbers of convection cells are different, the overall heat transfer behavior between the charge tubes and sulfur for the three conditions are quite similar. There are also no obvious distinctions among the streamlines and temperature filed near boundary layer region for these cases. The temporal sulfur temperature variations are plotted in Figure 5.8(b), showing that the shorter system has less thermal charge time due to its lower thermal mass. However, the heat transfer coefficients, h, for the three cases are very close as shown in Figure 5.8(c). The first row of data in Table 5.2 shows that the average h for H =12.5, 25, and 50D are, 231, 227 and 219 W/m²·K, respectively, indicating that increasing H can slightly decreases the heat transfer rate but this effect is relatively insignificant (by increasing H for 4 times, h decreases less than 6%).

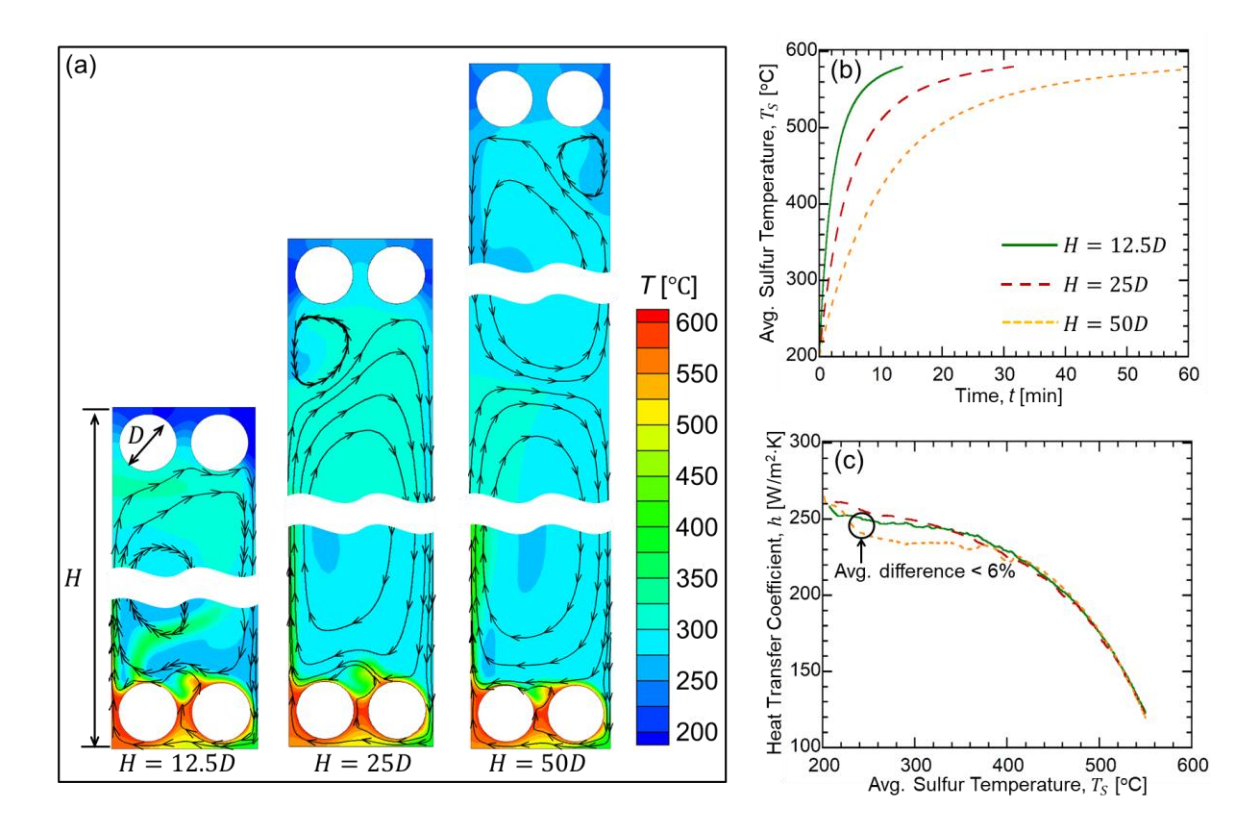


Figure 5.8. (a) Temperature and streamlines contours at $T_S \approx 400$ °C, (b) variation of the average sulfur temperature, and (c) variation of the heat transfer coefficient in the charge scenarios for the bath system with H = 12.5, 25, and 50D.

Table 5.2. Average heat transfer coefficient (from 200 to 550 °C) for various system height, H (Unit: W/m²·K)

		H = 12.5D	H=25D	H=50D
D = 5 mm,	p = 1.25	231	227	219
D = 5 mm,	p = 3	409	413	407
D=20 mm,	p = 1.25	259	262	249

Another two scenarios (where D=5 mm, p=3.0, and D=20 mm, p=1.25, respectively) are simulated to examine whether the heat transfer coefficients vary with H for larger p and D cases. Similarly, the variation of average h is less than 5% by varying H between 12.5 and 50 D. These results

verify that the impact of H is minor for the overall heat transfer performance of sulfur in the bath system and can be neglected in this study. The studies from ref [86] and [87] support this finding by showing that the confining adiabatic wall can affect the heat transfer coefficient of the natural convection over a horizontal cylinder only when the distance between the wall and the tube is 4 times or less of the tube diameter, i.e. H < 4D. This distance is much lower than the practical height for the bath system in this study.

Effect of the tube diameter and pitch ratio

Among all the independent parameters for the bath system, including, we have found that H and N cast an insignificant impact on the heat transfer behavior. Therefore, the natural convection for different bath systems should be characterized based on D and p. In this section, the effect of these two parameters is going to be investigated and a comprehensive correlation for the Nu number will be developed to quantify the heat transfer rate. The range of the parameters is set to be 5 mm < D < 40 mm and 1 , as shown in Figure 5.9, which covers the proposed design space for the SulfurTES system with bath configuration.

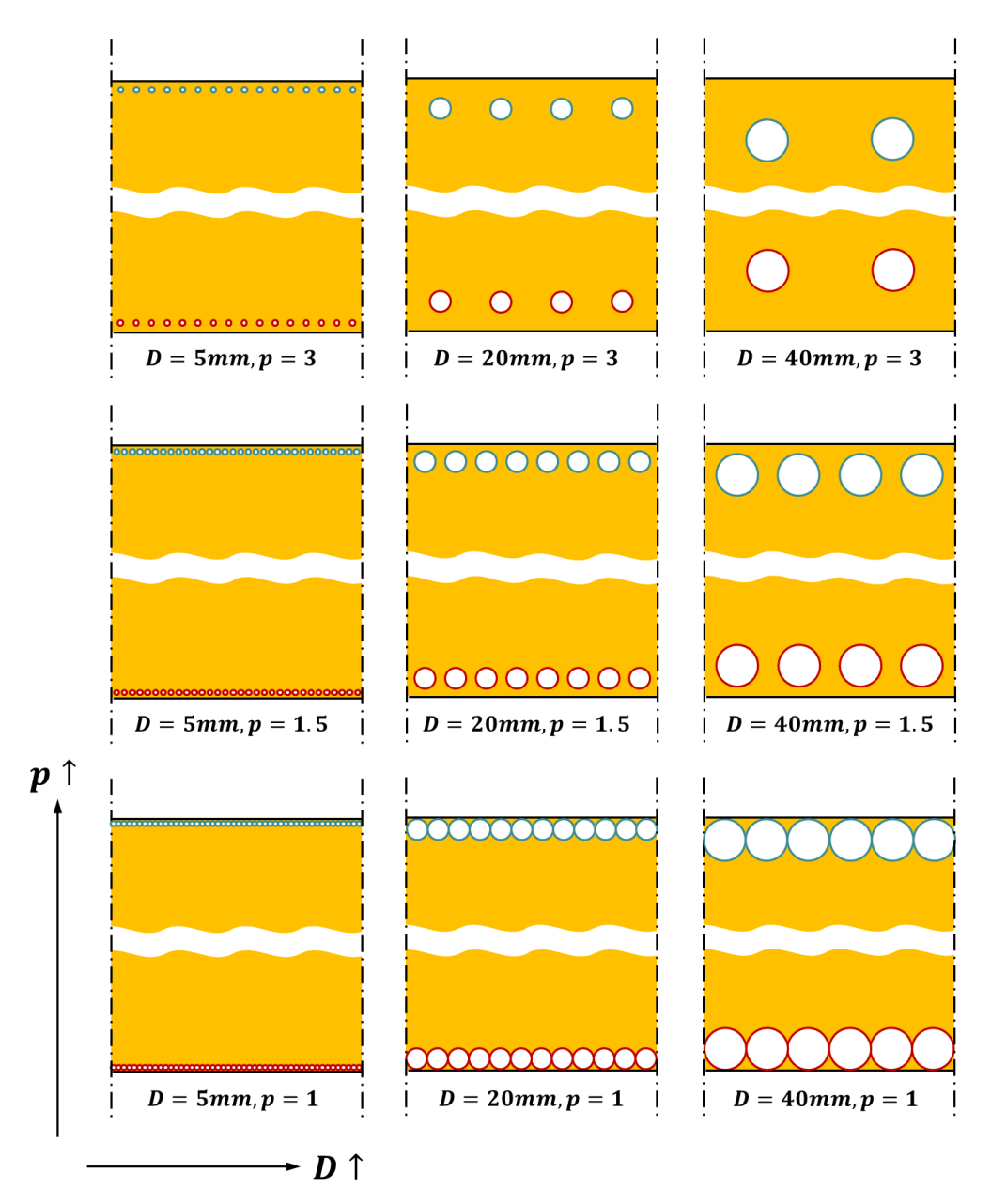


Figure 5.9. Schematics for SulfurTES bath systems with various *D* and *p* in the design space.

Figure 5.10(a) shows the temperature and streamlines contours for the scenarios of at the time instance when the average sulfur temperature is around 300 °C. It can be observed the space between the adjacent charge tubes is much larger than the thickness of the thermal boundary layer over the tubes ($\delta \gg \delta_T$) for all the cases. Therefore, the formation of the boundary layer over each tube is hardly affected by the adjacent tubes and the enclosure for all the diameters, though the flow field is

not steady due to the downstream effect. Figure 5.10 (b) shows the variation of the heat transfer coefficients, h, for p = 3. Without the impact from the adjacent tubes, the heat transfer behavior of sulfur should resemble the typical natural convection over a horizontal cylinder. Based on the scaling analysis of the boundary layer for the heat transfer coefficient, h satisfies $h = Nu \cdot k/D \sim R\alpha^{1/4}/M$ $D \sim D^{-1/4}$, which explains why h decreases with D in Figure 5.10(b). By decreasing p from 3 to 1.5, δ greatly decreases and significantly affects the heat transfer behavior, as shown in Figure 5.10(c). For D = 5mm, δ becomes comparable to δ_T and thus to some degree impede the rise of the hot sulfur around the charge tubes and interfere the heat transfer between them. For larger D, since the ratio between δ and δ_T follows $\delta/\delta_T \sim (p-1)Ra_D^{1/4}$ and increases with D, the impact by decreasing p is still not that obvious on the flow and temperature fields. The comparison of the average heat transfer coefficients in Figure 5.10(b) and (d) also supports this finding, which shows that by decreasing pfrom 3 to 1.5, the heat transfer coefficients for all the diameter decreases but the reduction in D =5mm case is much more significant than the other two scenarios. By continuing to decrease the p to 1.25, shows that the impact on D = 5mm case is still the most significant and the boundary layer on the adjacent tubes mixes up, "trapping" the hot sulfur around the tube from rising. From Figure 5.10 (f), the average h around the tube surface for the three cases decreases as expected and h for D5mm becomes even lower than the other two cases. Figure 5.10 (g) contours the temperature and the flow field for p=1 scenarios, which is an extreme condition for this study. In these cases, the adjacent charge tubes are connected, and the bottom half of the tubes (which is not contoured at) are ineffective for the thermal charge. The heat transfer behavior of sulfur is thus very close to the natural convection within a square enclosure with a flat hot bottom. Apart from the various boundary layer thickness, the temperature and flow fields for different diameters are quite similar and the convection currents are barely characterized by the tube diameter. Figure 5.10(h) shows that the three cases are very similar to each other and close to it for the natural convection in a $0.5 \text{ m} \times 0.5 \text{ m}$ enclosure with a flat bottom at $600 \, ^{\circ}\text{C}$.

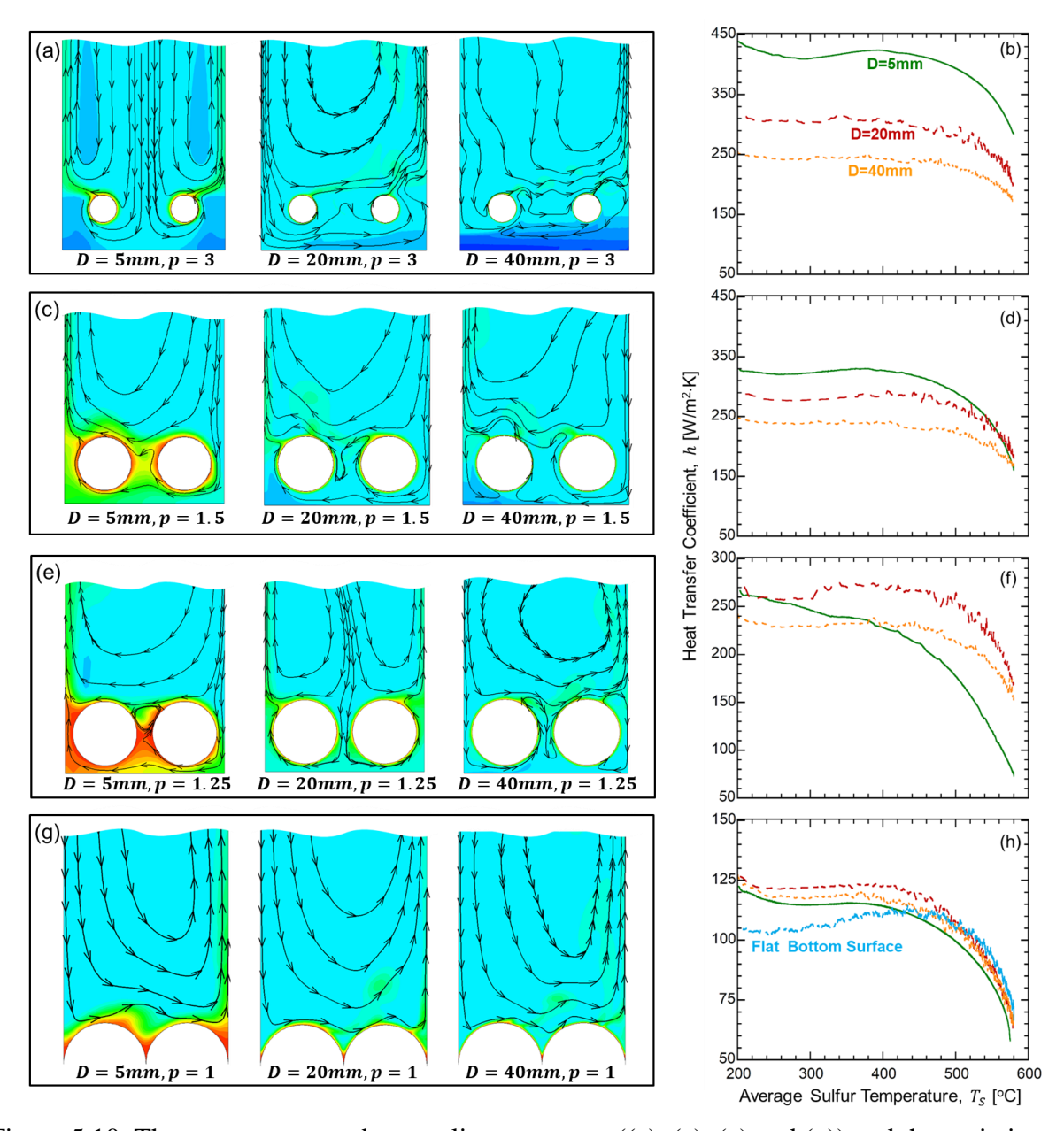


Figure 5.10. The temperature and streamlines contours ((a), (c), (e) and (g)) and the variation of the heat transfer coefficients ((b), (d), (f), and (h)) for the sulfur in bath system with various geometric parameters

Nusselt number correlation

To quantify the heat transfer rate with various, we simulated more cases with various D and p. The average h and average $Nu_D = hD/k$ are calculated from 200 to 600 °C as summarized in Table 5.3.

Table 5.3. Average heat transfer coefficient (from 200 to 580 °C) for various tube diameter, D and pitch ratio, p (Unit: W/m²·K)

						p				
		1	1.06	1.13	1.25	1.5	1.75	2	2.5	3
	5	108	-	-	217	308	347	370	391	406
	10	105	-	-	-	-	-	-	-	340
D [mm]	20	115	-	222	257	273	281	284	-	292
	30	111	-	-	-	-	-	-	-	254
	40	111	181	212	223	230	-	235	-	237

For all the diameters, $Nu_{D,avg}$ is almost maximized at p=3 and hardly changes with p at p>3. In addition, for a fixed D, $Nu_{D,avg}$ monotonically decreases from p=3 (theoretically $p\to\infty$) to p=1. Therefore, we propose to use the following correlation to calculate the average Nu number.

$$Nu_{D,avg} = Nu_{D,avg}|_{p=1} \cdot f(p) + Nu_{D,avg}|_{p=3} \cdot [1 - f(p)]$$
 (5.4)

Where

$$Nu_{D,avg}|_{p=1} = c_1 R a_{D,avg}^{c_2}$$
 (5.5)

$$Nu_{D,avg}|_{p=3} = c_3 R a_{D,avg}^{c_4} (5.6)$$

And f(p) monotonically varies from 1 at p=1 to 0 at $p\to\infty$. Based on the heat transfer physics as we discussed for Figure 5.10, f(p) is set up as a function of δ/δ_T , as shown below:

$$f(p) = \left[c_5 \left(\frac{\delta}{\delta_T}\right)^{c_6} + 1\right]^{-1} = \left[c_5 (p-1)^{c_6} R a_D^{0.25 c_6} + 1\right]^{-1}$$
 (5.7)

Equation 5.5 and 5.6 are proposed based on the typical form for the Nu number correlations in previous studies [76, 84]. We obtained the unknown constants in these two correlations by using the CFD results for D = 5, 10, 20, 30 and 40mm cases at p = 1 and p = 3, respectively (as shown in Table 5.3). Figure 5.11(a) shows the calculated average Ra and Nu number and the linear curve fit for the logarithm of the two dimensionless parameters. Therefore, c_1 to c_4 are obtained and Equation 5.5 and 5.6 can be expressed as:

$$Nu_{D,ava}|_{p=1} = 0.0812Ra_{D,ava}^{0.341}$$
(5.8)

$$Nu_{D,avg}|_{p=3} = 0.821Ra_{D,avg}^{0.247}$$
(5.9)

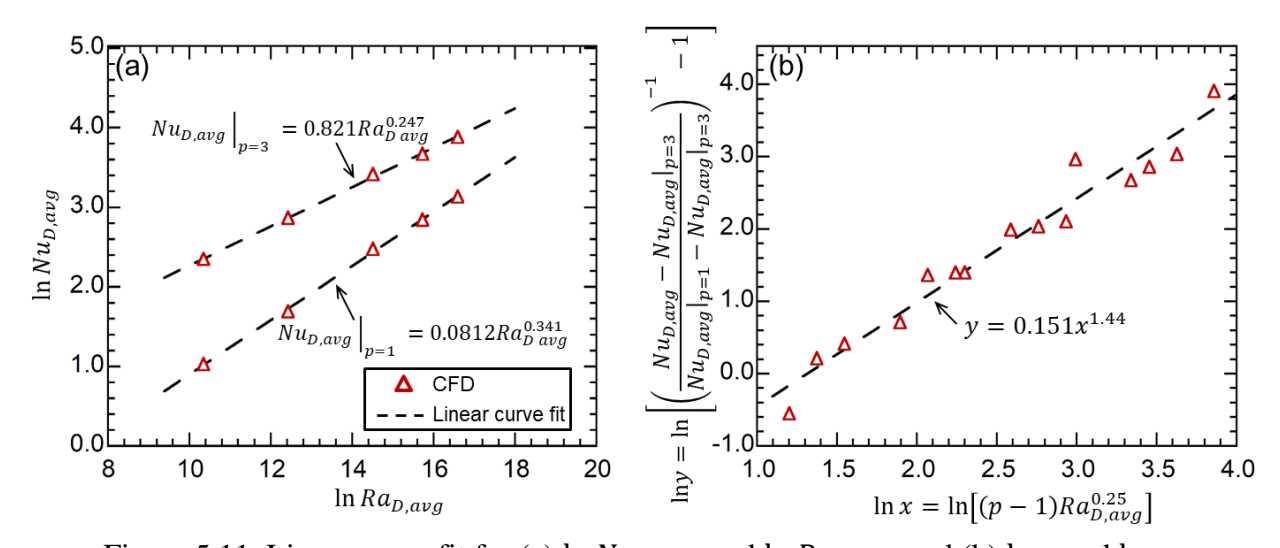


Figure 5.11. Linear curve fit for (a) $\ln Nu_{D,avg}$ and $\ln Ra_{D,avg}$ and (b) $\ln y$ and $\ln x$.

By substituting Equation 5.7 into Equation 5.4, we can obtain the following relationship:

$$c_5(p-1)^{c_6} Ra_{D,avg}^{0.25c_6} = \left(\frac{Nu_{D,avg} - Nu_{D,avg}|_{p=3}}{Nu_{D,avg}|_{p=1} - Nu_{D,avg}|_{p=3}}\right)^{-1} - 1$$
 (5.10)

Which can be reformed by taking the logarithm for both sides:

$$\ln c_5 + c_6 \ln \left[(p-1)Ra_{D,avg}^{0.25} \right] = \ln \left[\left(\frac{Nu_{D,avg} - Nu_{D,avg}|_{p=3}}{Nu_{D,avg}|_{p=1} - Nu_{D,avg}|_{p=3}} \right)^{-1} - 1 \right]$$
 (5.11)

The value of c_5 and c_6 are obtained as 0.151 and 1.44, through the CFD results (in Table 5.3) from 15 simulations with D=5, 20, and 40mm and 1 (5 cases with various <math>p for each D). Therefore, the final correlation of the Nu number is:

$$Nu_{D,avg} = 0.0812Ra_{D,avg}^{0.341}[0.151(p-1)^{1.44}Ra_D^{0.360} + 1]^{-1}$$

$$+ 0.821Ra_{D,avg}^{0.247}\{1 - [0.151(p-1)^{1.44}Ra_D^{0.360} + 1]^{-1}\}$$
(5.12)

The comparison between the Nu number in the CFD simulations and it from Equation (5.12) are plotted in Figure 5.12. The average error is 1.7%, showing a good agreement between the two results. This correlation can be directly utilized to provide the average heat transfer rate in the system-level design with D from 5 to 40mm and p from 1 to 3.

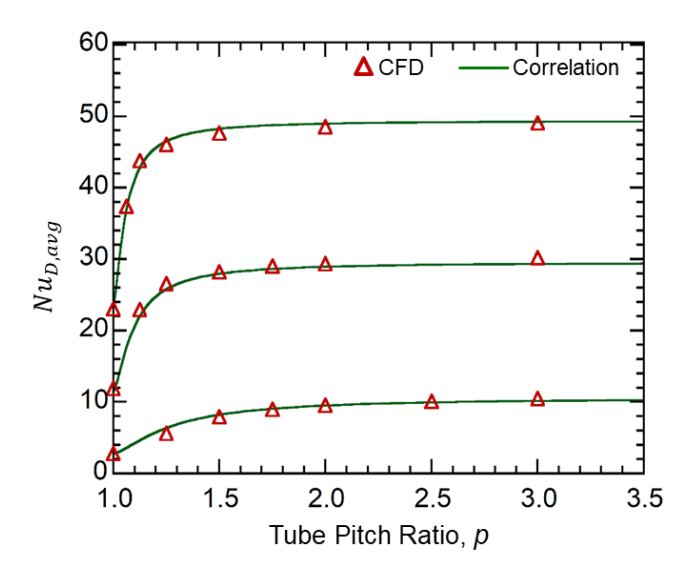


Figure 5.12. Comparison of Nu number from CFD results and the developed correlation in Equation (5.12).

To validate the developed correlation and verify the accuracy of using this correlation to predict the variation of average sulfur temperature. We use the analytical methods similar to it discussed in section 3. (Equation 3.13 and 3.14) to estimate the sulfur temperature variation for D = 5 and 40mm, and p = 1, 1.5 and 3. The numerical solution for volumetric average sulfur temperature with a forward difference scheme is:

$$T_{S,avg}\big|_{t+\Delta t} \approx T_{S,avg}\big|_{t} + \frac{h_{avg}A_{t}N_{t}}{\rho_{S}V_{S}c_{p,S}}(T_{w,avg} - T_{S,avg})\big|_{t}\Delta t$$
 (5.13)

Where the average heat transfer coefficient $h_{avg} = Nu_{D,avg}k_S/D$, N_t is the number of the charge tube, A_t is the surface area of one charge tube, $T_{w,avg}$ is the surface average wall temperature and Δt is the time step for the numerical solution. The comparison between these analytical results and them in CFD simulations is shown in Figure 5.13. The average and maximum difference between the two methodologies are 2.2% and 4.5%, which provides confidence in utilizing the developed correlation (Equation 5.12) for real-world bath system design.

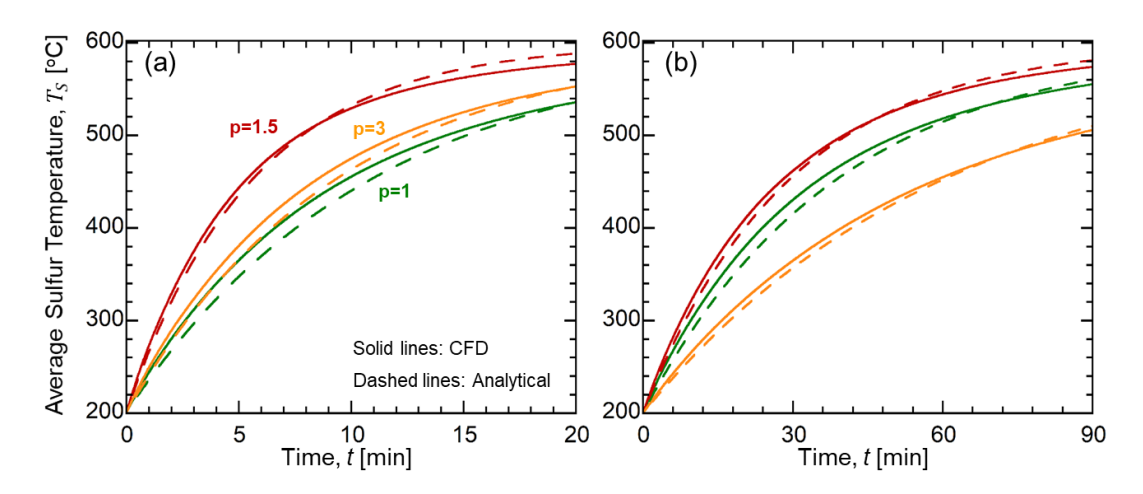


Figure 5.13. Comparison of CFD and analytical solutions for the average sulfur temperature variation in the bath system with (a) D = 5 mm and (b) D = 40 mm

5.2. Thermal performance analysis

Average heat transfer coefficient, $h_{avg} = Nu_{D,avg}k_S/D$, quantifying the average heat flux from charge tubes per unit temperature difference, is an important parameter affecting the thermal performance for the SulfurTES system. With the developed Nusselt number correlation (Equation 5.12), h_{avg} for the bath system with D from and p from can be plotted in a 3D figure, as shown in Figure 5.14(a). The maximum h_{avg} locates at D=5 mm and p=3.0, since it decreases with the characteristic length and increases with the space between two adjacent tubes, as discussed in section 5.1. For a real design scenario, some other factors might constrain the range of and would not be achieved. Therefore, the maximum of h_{avg} for a given D and p has been plotted in Figure 5.14(b) and (c), respectively. The green solid lines show the maximum h_{avg} and the black dashed lines ("p curve" or "p curve") show the value of p or p at which p reaches the maximum. These plots indicate p decreases with p increasing (since the heat transfer coefficient decreases with the characteristic length) and increases with p increasing (since the narrow space between the adjacent tubes can impede boundary layer formation over tube surface).

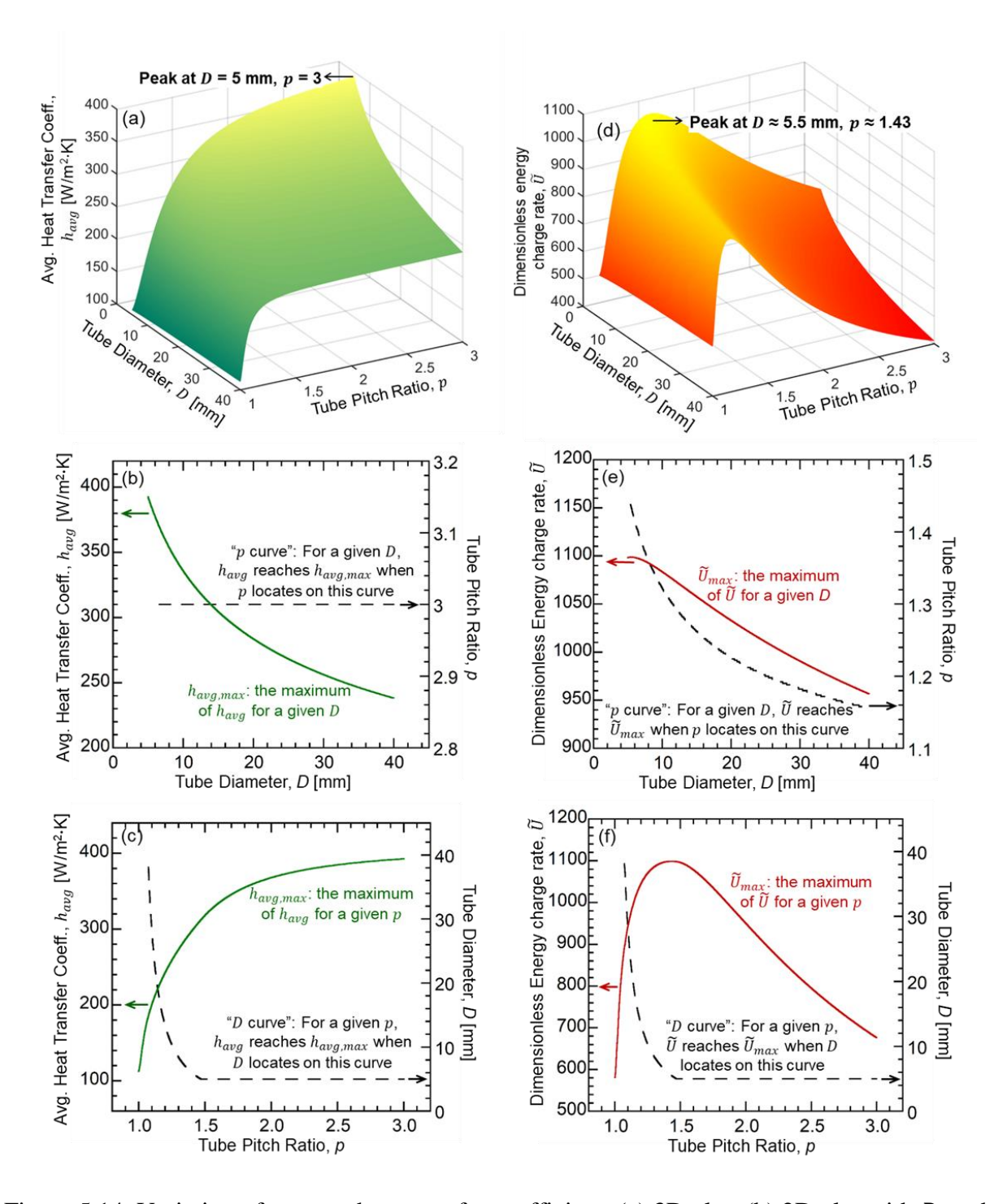


Figure 5.14. Variation of average heat transfer coefficient: (a) 3D plot, (b) 2D plot with *D* as the x-axis, and (c) 2D plot with *p* as the x-axis. Variation of energy charge rate: (a) 3D plot, (b) 2D plot with *D* as the x-axis, and (c) 2D plot with *p* as the x-axis.

On the aspect of system-level performance, the overall thermal performance for a bath system is not only determined by the heat transfer coefficient but also dominated by the total heat transfer area, as shown in Equation 5.13. To quantify this system-level thermal performance, the thermal charge rate, U, can be defined as:

$$U = h_{avg} N_t A_t = \frac{N u_{D,avg} k}{D} \cdot \frac{W}{pD} \cdot \pi DL = \pi W Lk \cdot \frac{N u_{D,avg}}{pD}$$
 (5.14)

Where N_t is the number of the charge tube, A_t is the surface area of one charge tube, L is the tube length, and W is the system width. To analyze the relationship between the thermal charge rate and the geometric parameters, we define the dimensionless thermal charge rate, \widetilde{U} , in Equation (5.15):

$$\widetilde{U} = \frac{Nu_{D,avg}}{pD} \tag{5.15}$$

The calculation of \widetilde{U} by using the correlation (Equation (5.11)) from 1 , and <math>5 mm < D < 40 mm has been shown in the 3D plot Figure 5.14(d) and the maximum of \widetilde{U} is found to locate at p = 1.43, D = 5.5 mm. Similar to Figure 5.14 (b) and (c), the "p" and "D curves" as well as the corresponding maximum \widetilde{U} values have been plotted in Figure 5.14 (e) and (f), respectively. Unlike h_{avg} , \widetilde{U} no longer monotonously increases with p, since the large p can result in high h_{avg} but a limited heat transfer area. For SulfurTES bath system design, the geometric parameters which are at or at least close to p = 1.43, p = 5.5 mm should be selected to guarantee the overall thermal charge rate.

5.3. Comparison with isochoric tube configuration

As mentioned in the first section of this study, the bath system can potentially provide superior heat transfer performance. In this section, the preliminary design for a 1MWh SulfurTES bath system has been proposed and compared with the tube-configuration systems.

Table 5.4 shows the comparing information for the different configuration SulfurTES system. For the horizontal tube system, the characteristic length, which is tube diameter, is set to be 0.168 m (6" NPS) based on the performance and cost analyses by Wang et al [64]. The length of the tube, characterizing the natural convection in the vertical tube system, is selected to be 1 m, which provides the same heat transfer coefficient as it in the horizontal tubes. The number of tubes for the two systems is calculated to be 217 to achieve 1MWh for total storage capacity with 6-hour charge from 200 to 600 °C. Two types of bath system design are developed with the optimized tube diameter and pitch ratio, i.e., D = 5.5 mm, p = 1.43. The tube length is 1 m which is same as it in the tubeconfiguration system. In the first bath system, the height of system is 0.15 m (around 27D) and the total number of tubes is calculated to be 4137. In comparison to the two tube-configuration systems as shown in Table 5.4, this system can provide similar thermal charge rate but use much less heat transfer area because of the much higher heat transfer coefficient. It indicates that the bath system could save the necessary steel materials for charge and discharge tubes and have lower cost than the horizontal- or vertical- tube systems. In the second bath system, the total heat transfer area is same as it for the tube-configuration systems, by setting the height of system to be 0.087 m (around 16D) and the total number of tubes to be around 7200. Due to the higher heat transfer coefficient, it can provide around 72% higher thermal charge rate but requires less amount of tube materials than the tube systems. Therefore, it can be concluded that the bath configuration is a promising SulfurTES system

design since it can either provide a higher thermal charge rate or greatly save the tube material cost compared with the previous systems.

Table 5.4. Comparison among the 1MWh Sulfur TES systems with tube- and bath-configuration

	System capacity [MWh]	Geometric parameters	Total heat transfer area [m²]	Heat transfer coefficient, h [W/m²·K]	Thermal charge rage, U [kW/K]
Horizontal tube system	1	$D_t = 0.168 \text{ m}$ $L_t = 1 \text{ m}$ $N_t = 217$	124	175	21.7
Vertical tube system	1	$D_t = 0.168 \text{ m}$ $L_t = 1 \text{ m}$ $N_t = 217$	124	175	21.8
Bath system I	1	$D_t = 5.5 \text{ mm}$ p = 1.43 $L_t = 1 \text{ m}$ H = 0.15 m $(\approx 27D)$ $N_t = 4137$	71.5	304	21.7
Bath system II	1	$D_t = 5.5 \text{ mm}$ $p = 1.43$ $L_t = 1 \text{ m}$ $H = 0.087 \text{ m}$ $(\approx 16D)$ $N_t = 7200$	124	304	37.6

5.4. Conclusions

This study investigated the heat transfer behavior of sulfur in the bath-configuration system and the results show that the heat transfer rate is dominated by the tube diameter, D, and pitch ratio, p. The heat transfer coefficient decreases with the tube diameter due to the laminar nature of the convection phenomenon, similar to it in the isochoric tubes discussed in Chapter 3. With the pitch ratio decreasing, the heat transfer coefficient will also decrease because the narrow space between the adjacent tubes can significantly slow down the buoyancy-driven currents. The effect of tube pitch ratio is more distinct for the smaller diameter tubes since the space between the adjacent tubes is closer to the boundary layer thickness and therefore affects the heat transfer more significantly.

A Nusselt number correlation, valid for D from 5 to 40 mm and p from 1 to 3, for the thermal charge scenario is developed as a function of the Rayleigh number, Ra, and p. It can be utilized as the critical design bases for the bath-configuration system based on the heat transfer coefficient and the thermal charge rate. The highest heat transfer coefficient was found at D=5 mm and p=3 while the highest thermal charge rate occurs when D=5.5 mm and p=1.43. In comparison to the isochoric-tube system, the bath-configuration can have higher heat transfer coefficients with small diameter tubes. Therefore, this is a promising system design approach for the SulfurTES in that it can achieve a higher thermal charge rate or less tube material cost as desired for the particular application.

Chapter 6

Conclusions and future work

Conclusions for this dissertation

Sulfur is an attractive thermal storage medium for low-cost, high temperature, and high heat transfer rate applications. The results of this study are important since they provide important insight into sulfur heat transfer behavior and performance for several canonical configurations that may be used for sulfur TES applications. In particular, this dissertation investigates both tube- and bath-configuration systems. Major conclusions from this dissertation are as follows:

- Laminar natural convection is the dominant heat transfer mechanism in isochoric SulfurTES
 systems and, as expected, the heat transfer rate decreases with the characteristic length (e.g.
 tube diameter for the horizontal-tube system and bath-configuration system, and tube height
 for the vertical-tube system).
- When uniformly heated, lower aspect ratio tubes (L/D < 7) can provide higher heat transfer coefficients when vertically oriented, as opposed to horizontally oriented. These results are detailed in Figure 3.15.
- In comparison to uniform heating, top-heated vertical tubes provide superior exergy charge performance because of the formation of the thermal stratification; while bottom-heated vertical tubes exhibit a higher energy charge rate due to a strong buoyancy-driven mixing between the cold and the hot sulfur.
- Heat transfer behavior for sulfur bath configuration systems is primarily governed by the tube diameter and pitch ratio. The heat transfer rate rises with decreased tube diameter and increasing pitch ratio. In comparison to the isochoric-tube system, the bath-system can potentially have a higher system-level heat transfer for charging and therefore provide higher thermal charge rate or lower tube material cost.
- Each study has developed the critical analytical tools, such as the Nusselt number correlations (Equation (4.25), Equation (4.26), and Equation (5.11)) and the analytical procedures in

Section 4.3.2, allowing the estimation of the heat transfer performance and providing important qualitative and quantitative design bases for SulfurTES systems.

All the research efforts demonstrate that the SulfurTES has excellent thermal performance and pave the way for the scalability of high-temperature sulfur-based thermal storage for industrial-scale applications.

Future Work

From the current studies, the heat transfer behavior of sulfur in isochoric TES systems has been better understood and the relevant heat transfer rates in various systems have been quantified. Based on these studies, the following future efforts are recommended:

- Investigations of system-level performance for tube- and bath-configuration systems.
- Synthesis system design for SulfurTES in utility-scale systems by implementing the design criteria from this dissertation.
- Feasibility study for using SulfurTES for higher temperatures (e.g., up to 800 °C) thermal storage applications.
- Development of new sulfur-based storage medium with optimized thermal properties and performance.
- Examination of SulfurTES for a wide range of thermal energy storage applications with cost analyses to reveal applications that are enabled by the low cost of sulfur-based TES.

Appendix A: Insulation system study

The insulation system is an important component in high-temperature thermal storage applications to minimize heat loss from the storage system and to provide necessary protection for safe operation. In this appendix chapter, I conducted a literature review and an analytical study for the insulation system design and optimization. The objective is to understand the dominant factor for the insulating effect and provide an effective insulation system design for the high-temperature TES system.

Insulation Materials

The high-temperature insulation materials can be classified [88] as fibrous, refractory, and microporous insulations which can provide effective thermal resistance at the high temperature > 600 °C. The properties and characteristics of these materials have been summarized in Table A-1. Fibrous materials such as glass and ceramic fiber have been widely used for high-temperature insulations, due to its high flexibility and low specific gravity. Refractory materials are usually solid-based and inflexible but can provide high fire resistance for the high-temperature setups. In recent years, microporous media including fumed and pyrogenic silica have gained increasing popularity. These materials have microporous structures with many air paths in micro-scale, which not only decreases the effective thermal conductivity of the material to a similar level of air but blocks the convective heat transfer of air within the insulation layer. Therefore, the microporous insulation can usually provide superior thermal resistance in comparison to the other materials and should be the most appropriate option for the large-scale static thermal storage.

Table A-1. High-temperature Insulation Materials

Туре	Thermal conductivity (600°C) [W/m·K]	Highest operation temperature [°C]	Flexibility	Specific Weight
Fibrous Insulation	> 0.10W/m·K	> 1000	High	Low
Refractories	≈ 0.25 W/m·K	> 1000	Low	Medium
Microporous Insulation	≈ 0.06 W/m·K	> 800	Low	High

Note: The information for the insulation properties are extracted from the technical data sheet by Morgan Advanced Materials: http://www.morganadvancedmaterials.com/en-gb/ and Promat, Inc.: https://www.promat.us/en

Multilayer Insulation System

For high temperature applications, radiative heat transfer dominates the heat loss from the hot surfaces. To impede this type of heat loss, reflective layers (or screens) with high reflectivity are utilized in many insulation systems, named as multilayer insulation system (MLI).

Daryabeigi et al. [89] have designed a fibrous multilayer insulation system for re-entry aerospace vehicle targeting at decreasing the total mass of insulation system but achieve the same insulating effect by using MLI system in place of the original single-layer insulation. The results indicated that the installation of the 16 reflective layers can decrease 22% of mass of the insulation materials. Spinnler, et al. [88] have studied the effect of different types of reflective layers and insulation layers for the high-temperature MLI system. They found that the effective thermal conductivity of insulation system with four gold reflective layers is around 30% lower than it with four stainless-steel layers, and around 40% lower than the original single-layer fibrous insulation. The effect of installing reflective layers is not very distinctive for the microporous insulation, however, the MLI system with

microporous insulation and gold reflective layer still has the lowest effective conductivity and best insulating performance.

In this study, an MLI system with microporous insulation and multiple reflective layers is designed and optimized. An analytical model is developed to quantify the overall insulating effect and is validated by the experimental measurements.

Analytical Model

An analytical model for heat transfer through an MLI system is developed based on the conductive and radiative heat transfer physics for porous media [88-90]. First of all, the effective thermal conductivity is usually defined as the summation of conductive and radiative conductivity, as shown in Equation (A.1) to (A.3).

$$k_{eff} = k_{cond} + k_{rad} \tag{A.1}$$

$$k_{cond} = k_{air} + k_{solid} = \frac{k_{air}^*(T)}{1 + \frac{2\beta K_B T}{Pr\sqrt{2}\pi d^2 L_c P}} + F f^b k_{solid}^*(T)$$
 (A.2)

$$k_{rad} = \frac{16\sigma n^2 T^3}{3\rho e} \tag{A.3}$$

Where * represents the material properties, β is a coefficient dominated by thermal accommodation coefficient and specific heat ratio, k_B is Boltzmann constant, Pr is Prandtl number, d is fiber diameter, L_c is the characteristic length of porous structures, P is pressure, P is an undetermined constant, P is the solid fraction ratio, P is an undetermined constant, P is the Stefan-Boltzmann constant, is the effective index of refraction, is P material density, and P is effective property. From the study of Spinnler, et al, P is an P at high temperatures can be assumed as a constant P and a function of cubic P, P is an interval P is an undetermined constant of the study of Spinnler, et al, P is an undetermined constant, and P is effective property. From the study of Spinnler, et al, P is an undetermined constant, and P is effective property. From the study of Spinnler, et al, P is an undetermined constant, and P is effective property. From the study of Spinnler, et al, P is an undetermined constant, and P is effective property. From the study of Spinnler, et al, P is an undetermined constant, and P is effective property. From the study of Spinnler, et al, P is an undetermined constant, and P is effective property.

the Promat. Inc is plotted versus T^3 to obtain the radiative and conductive thermal conductivity in Figure A-1. The good linearity of the curve helps validate the assumption from Spinnler's study. By fitting this curve, the conductive and radiative thermal conductivity can be quantified as:

$$k_{cond} = 0.0222 \left[\text{W/m} \cdot \text{K} \right] \tag{A.4}$$

$$k_{rad} = 1.131 \times 10^{-11} T^3 [\text{W/m} \cdot \text{K}]$$
 (A.5)

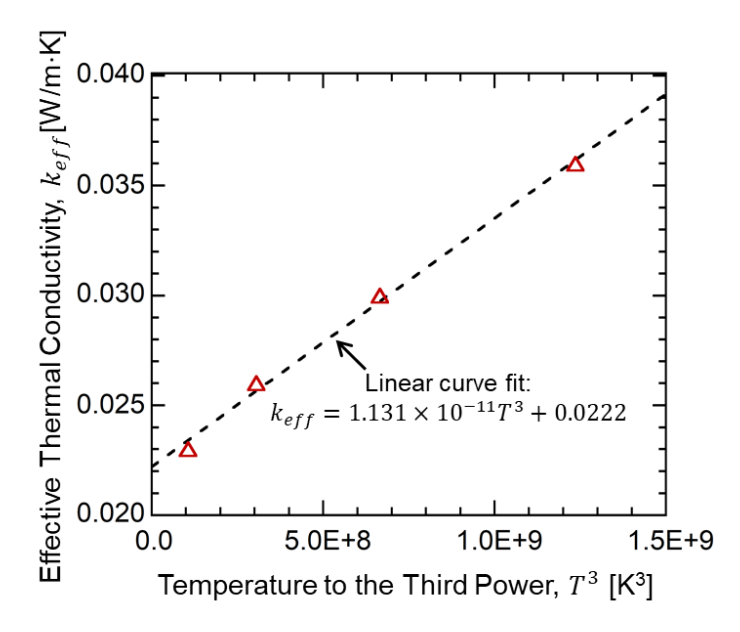


Figure A-1. Thermal conductivity of microporous insulation (as a function of T^3)

The thermal circuit concept [74,91] has been utilized for the 1-D steady-state heat transfer analysis, as shown in Figure A-2 (a) and (b). The temperatures for each reflective layers are $T_{r,1}$, $T_{r,2}$, ..., $T_{r,n}$, and $T_{r,n+1}$ where n is the total number of insulation layers (and n+1 is the total number of reflective layers). The conductive thermal resistance for each insulation layer, $R_{cond,i}$ is defined in Equation (A.6), which dominated by the thermal conductivity of the microporous insulation, R_{cond} , and the thickness of the insulation layer, L_i (effect of the reflective layer can be neglected since the thickness of the reflective layer is usually much smaller than it for the insulation layer). For radiative heat transfer, the thermal resistance is the summation of the insulation and reflective layer resistances, $R_{rad,ins,i}$ and

 $R_{rad,r,i}$, which are defined in Equation (A.7) and (A.8), respectively. $\varepsilon_{r,i}$ is the emissivity of each reflective layer and various with the materials and the surface characteristics. In this section, all the thermal resistances are expressed in form of them in 1-D cartesian system, the expressions for cylindrical or spherical coordinates can be found in ref [74]

$$R_{cond,i} = \frac{L_i}{k_{cond}} \tag{A.6}$$

$$R_{rad,ins,i} = \frac{L_i}{k_{rad}} \tag{A.7}$$

$$R_{rad,r,i} = \frac{\frac{1}{\varepsilon_{r,i}} + \frac{1}{\varepsilon_{r,i+1}} - 1}{\sigma(T_{r,i}^2 + T_{r,i+1}^2)}$$
(A.8)

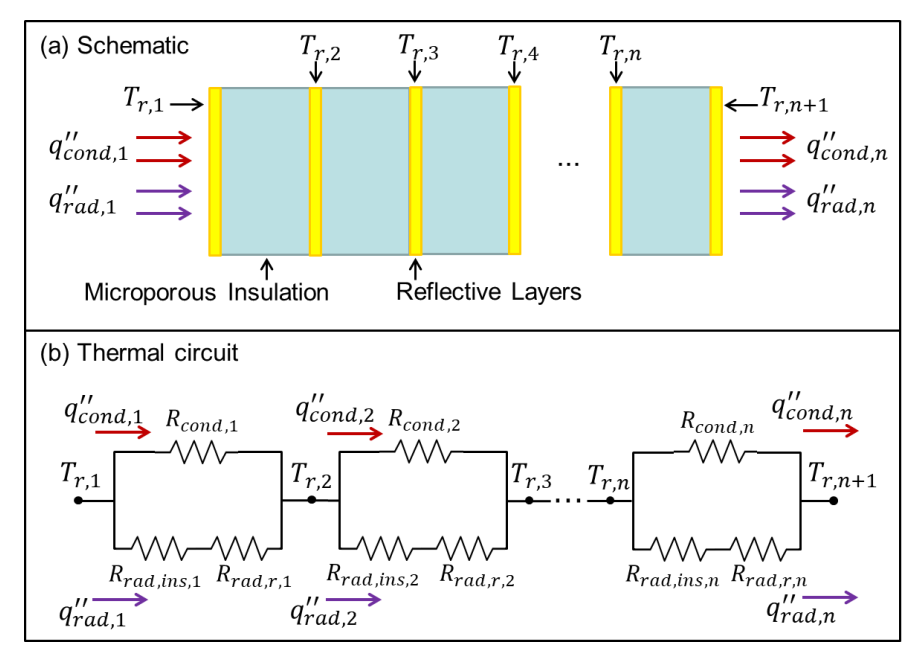


Figure A-2. (a) Schematic and (b) thermal circuit for multilayer insulation system

The total heat flux through the whole insulation system can be classified as the conductive heat flux, $q''_{cond,i}$, and the radiative heat flux, $q''_{rad,i}$. Based on the energy balance in a thermal circuit, the following relationship should be satisfied in the steady-state heat transfer process:

$$q_{cond,i}^{"} = \frac{T_{r,i} + T_{r,i+1}}{R_{cond,i}}$$
 (A.9)

$$q_{rad,i}^{"} = \frac{T_{r,i} + T_{r,i+1}}{R_{rad,ins,i} + R_{rad,r,i}}$$
(A. 10)

$$q_{cond,1}^{"} + q_{rad,1}^{"} = q_{cond,2}^{"} + q_{rad,2}^{"} = \dots = q_{cond,n}^{"} + q_{rad,n}^{"}$$
(A.11)

For the two sides of the insulation system, the boundary condition can be assumed to be constant temperature boundaries where $T_{r,1}$ and $T_{r,n}$ are known constant values or to be convective and radiative boundaries, as shown in the following equations:

$$q_{cond,1}^{"} + q_{rad,1}^{"} = h_{\infty} (T_{r,1} - T_{\infty}) + \varepsilon_{r,1} \sigma (T_{r,1}^{4} - T_{\infty}^{4})$$
(A. 12)

$$q_{cond,n}^{"} + q_{rad,n}^{"} = h_{\infty} (T_{r,n} - T_{\infty}) + \varepsilon_{r,1} \sigma (T_{r,n}^4 - T_{\infty}^4)$$
 (A.13)

From Equation (A.9-13), there are 3n + 1 independent equations with 3n + 1 unknown parameters (n + 1 for reflective layer temperatures, $T_{r,i}$, n for conductive heat flux, $q''_{cond,i}$, and n for radiative heat flux $q''_{rad,i}$). Therefore, the steady-state temperature profile and the heat flux distribution for the insulation system can be solved based on this analysis.

Experimental study

To understand the heat transfer through the insulation system and validate the analytical model introduced in the last section. Two experimental studies with a tube- and a flat-pate configuration system were conducted. The flat-plate experimental system is shown in Figure A-3.

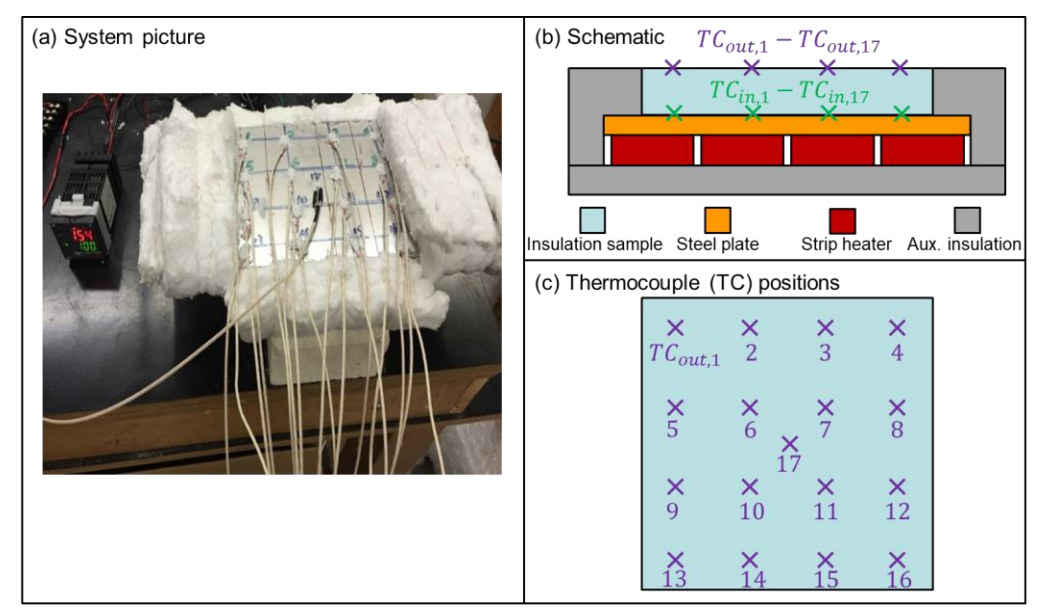


Figure A-3. (a) Picture, (b) schematic, (c) thermocouple position map for the experimental system with flat-plate configuration.

In this system, a flat steel plate with four strip heaters installed underneath is used to uniformly heat the insulation samples from the bottom side. On each side of the insulation sample, there are 17 thermocouples ($TC_{out,17}$ to $TC_{out,17}$ and $TC_{in,17}$ to $TC_{in,17}$) uniformly attached to measure the temperature distribution of the insulation surfaces. $TC_{in,17}$ is utilized as the feedback temperature for the PID controller to control the heat flux provided by the strip heaters and achieve the stepwise heating for the insulation sample. The auxiliary (aux.) insulation is installed to minimize the heat loss from the test system.

During the test, the steady-state temperature distributions for each side of the insulation sample are obtained in the 6 stages in which the set temperature in PID controller is set as and held at 100, 200, ..., 600 °C, respectively. Because of the heat loss from the auxiliary insulation, the temperature near the edge of the sample (such as location 1-4 in Figure A-3 (c)) was found to be much lower than it at the center (location 17 in Figure A-3 (c)). In the central part of the insulation simple (the area covering location 6, 7, 10, 11 and 17, for both TC_{out} and TC_{in}), however, the temperature

measurements for these 5 spots on each side are close (differences less than 10 °C). Therefore, the heat transfer in this area is assumed to be one-dimensional and the average temperature for these 5 locations on each side of the insulation sample is calculated and compared with the 1-D analytical results solved through the proposed analytical model, as shown in Figure A-4. The good agreement between the two results provides the preliminary validation for the analytical model.

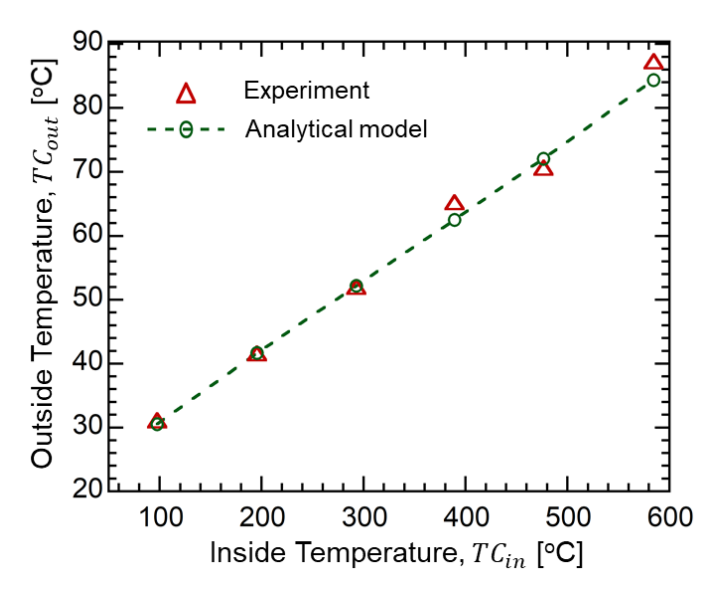


Figure A-4. Comparison of the average central outside temperature for the insulation sample between the experimental and analytical results.

The second experimental study is conducted in a tube-configuration system, as shown in Figure A-5. A 5-cm (2") OD and 30-cm long sulfur storage tube wrapped with the PID controlled insulation tapes were used as the heat sources for the insulation sample in a pipe shape. The temperature distribution for each side of the sample was measured by 7 thermocouples. Two scenarios (with and without reflective layer on top of the insulation sample) were studied with this setup, as shown in Figure A-5 (a) and (b). The reflective layer is polished aluminum foil, of which the emissivity is around 0.04 at the temperature below 100 °C, theoretically. The outside thermocouples are attached on top

of the insulation sample and reflective layer for the scenarios with and without reflective layer, respectively.

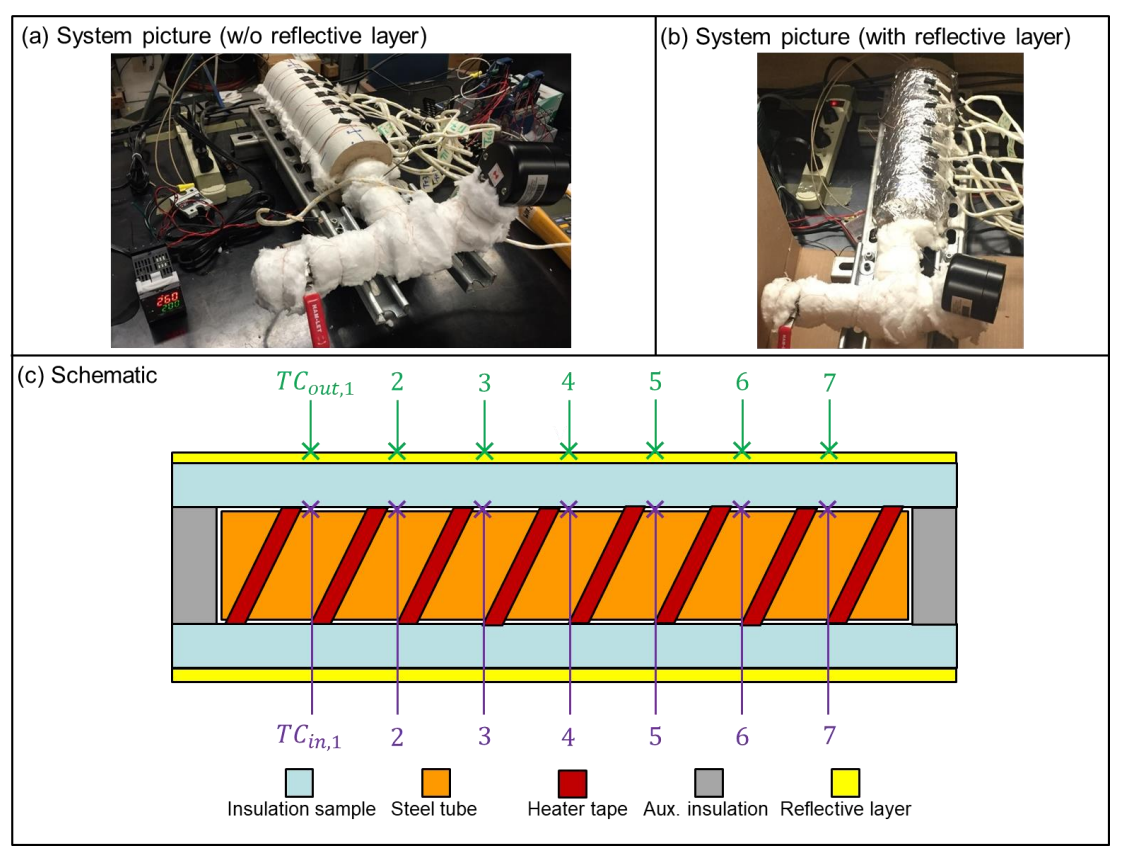


Figure A-5. Pictures ((a) without reflective layer, (b) with reflective layer)) and (c) schematic of the experimental system in tube-configuration.

There are also 6 stages (100, 200, ..., 600 °C) in the experiments, and the steady-state temperature distributions for both sides of the insulation sample are monitored. The average temperature of the central part covering the location 3,4, and 5 is calculated and the outside surface temperature (average of $TC_{out,3}$ to $TC_{out,3}$) is compared with the one-dimensional analytical results for both scenarios (with and without reflective layers), as shown in Figure A-6. The mismatch between the experimental and analytical results is still acceptable, given the maximum differences between them for all heating stages (100 to 600 °C) is around 8.4%.

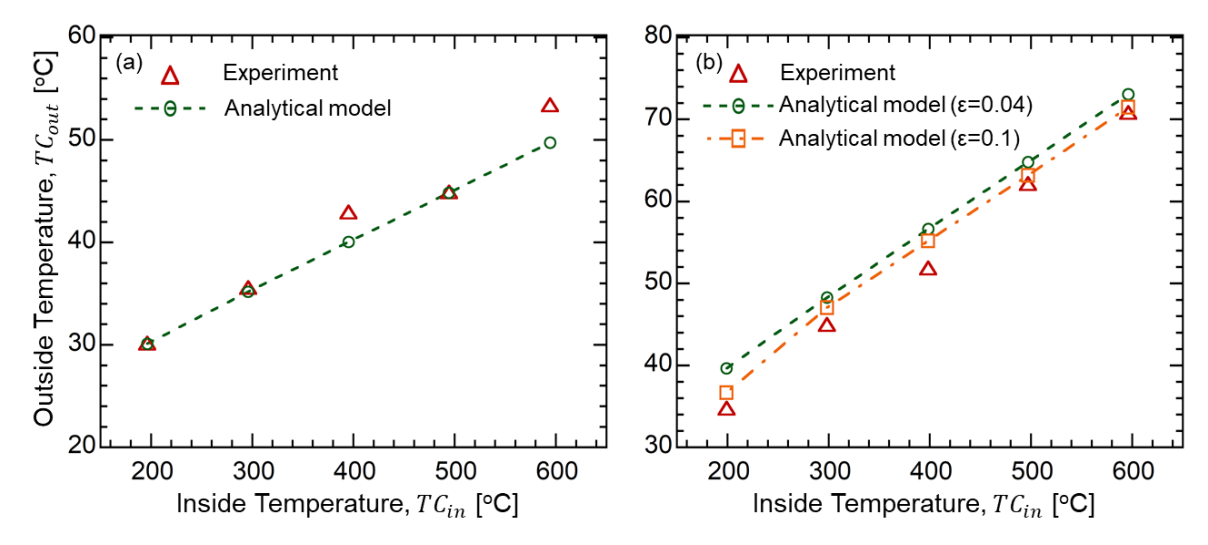


Figure A-6. Comparison of the average central outside temperature for the insulation sample (a) without any reflective layer and (b) with reflective layers in the tube-configuration experimental system.

This mismatch might be dominated by the uncertainty of the emissivity of the aluminum foil and the insulation outside surface since the aluminum foil was inevitably cramped when being wrapped around the insulation sample. This might significantly increase the emissivity of the reflective layer. To verify the effect of the emissivity variation for the reflective layer, the input emissivity of reflective layer is changed from 0.04 (for flat aluminum foil) to 0.1. The relevant result (orange curves and markers in Figure A-6(b)) is found to agree better with the test data. Therefore, the insulating effect of the MLI system can be significantly affected by the emissivity of the reflective layer and maintaining the smoothness of the reflective surface during the operation can be a challenge for the real applications. Nevertheless, the overall agreement of the experimental and analytical results is still good and validates the analytical model for being utilized for further studies.

Multilayer insulation system design

With the validated model, the optimized design of the multiplayer insulation system has been designed in this section. Since the radiative heat loss is dominant at high temperatures, therefore, the

reflective layers locate near the high-temperature side (at $T_H = 600$ °C) to decrease the heat loss more efficiently, as shown in the schematic in Figure A-7 (a). The temperature of the other side is assumed to be at $T_C = 20$ °C). The total thickness of the insulation system is set to be $L_C = 90$ mm, and the thermal conductivity for microporous insulation layer is still used as shown in Figure A-1. The space between the adjacent reflective layers, L, can affect the insulating effect and has been investigated first, with 5 reflective layers in the insulation system. From Figure A-7 (a), the critical value of L is around 4mm, which provides the lowest heat loss through the insulation system. Afterward, the effect of the number, N, and emissivity, ε of the reflective layers on the heat loss has been studied as shown in Figure A-7(b). It can be observed that by increasing N or decreasing ε of the reflective layers, the overall heat loss can be significantly decreased. The maximum decrease brought by the reflective layers can be equal to all the radiative heat loss when N is reaching infinity or ε is reaching 0. However, with increasing number of the reflective layers, the decreasing rate of the heat loss is actually decreasing and all the curves are flattened at large numbers of the reflective layers. In addition, the cost of the reflective layer will be unaffordable for large N and small ε . Therefore, the tradeoff between the insulating effect and the reflective layer cost will dominate the final design for the multilayer insulation system.

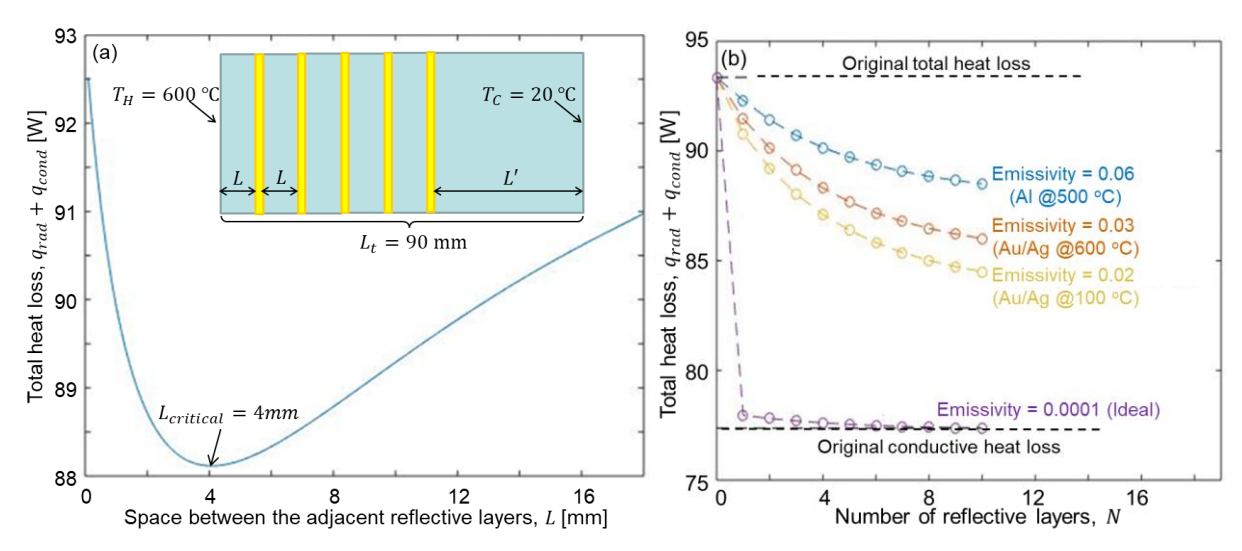


Figure A-7. Variation of total heat loss with (a) various space between adjacent reflective layers, and (b) number and emissivity of the reflective layers.

From this study, it can be concluded that by using 10 Aluminum reflective layers, the overall heat loss can be decreased for 4.2%, while by using 10 gold reflective layers, the overall heat loss can be decreased for 8.4%, in comparison with the scenario without any reflective layer. Developing a cost-effective reflective layer with ultra-low surface emissivity can be the focus for the future insulation studies. Form the other hand, given the radiative heat loss through the microporous insulation without reflective layer is only around 17% of the total heat loss, the thermal resistance provided by one single layer of microporous insulation might be sufficient for many high-temperature applications.

Appendix B: Demonstrations of SulfurTES thermal battery system

In addition to the heat transfer study for a single sulfur storage tube (element-level study) as discussed in Chapter 3 and Chapter 4, the author also participated in the design and fabrication of two SulfurTES thermal battery demonstrations.

The first system named lab-scale SulfurTES was demonstrated to prove the feasibility of using element sulfur to storage the thermal energy at high temperatures (200 to 600 °C). The system is analogous to the shell-and-tube heat exchanger system as shown in Figure B-1. Ten sulfur storage tubes, with 1-m length, 5.5-cm OD, and Sch. 40 thickness, are assembled in a steel heat exchanger shell with multiple crossflow baffles. The heated air flows from the inlet port as the heat transfer fluid to thermally charge the system and leaves the system form the outlet port. For the thermal discharge loop, the cold air enters the system from the outlet port to discharge the sulfur tubes and in the meantime maintain the thermocline. A cartridge heater is installed though the thermal well in each storage tube from the cold end (near the outlet port) to as auxiliary heat sources.

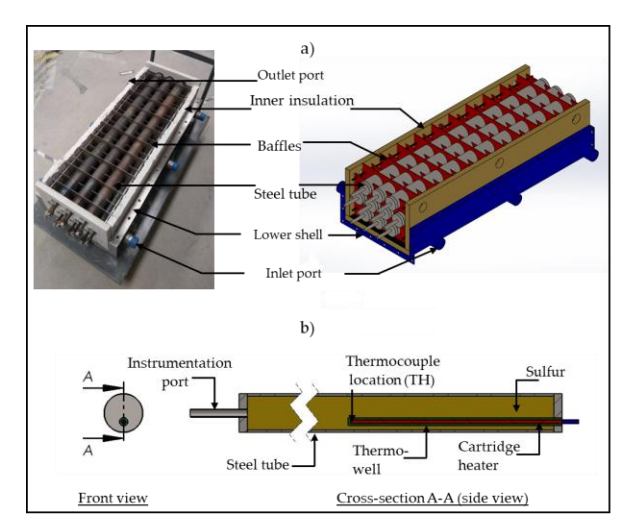


Figure B-1. (a) The picture and the design schematic for the lab-scale SulfurTES and (b) schematic for the sulfur storage tube in the lab-scale SulfurTES.

The installation process of the whole system is shown in Figure B-2. The storage tubes are filled with the molten sulfur and conditioned by multiple thermal cycles and argon flushing. These tubes are installed in the bottom half steel shell with two layers of microporous insulation attached on the inner and outer sides of the shell. For each tube, there are two thermocouples measuring the inner sulfur temperature from the instrumentation tube and the thermal well, respectively. For the tube surface temperature distribution, it is measured by 12 thermocouples from the instrumentation port in the bottom shell and 8 thermocouples from the instrumentation ports in the top shell are installed.

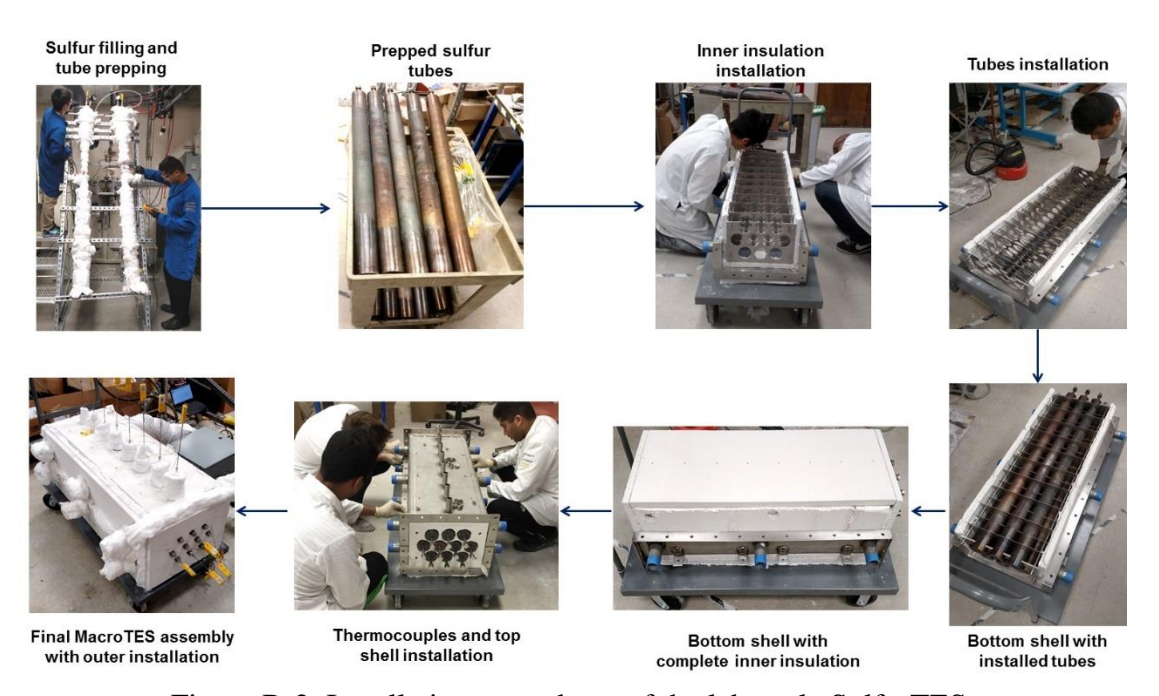


Figure B-2. Installation procedures of the lab-scale SulfurTES.

A 10-kW air heater with the PID controlled system is utilized to provide the hot air as the heat transfer fluid for the SulfurTES system, as shown in Figure B-3. At the other end of the system, the exhaust air flows to an air-water heat exchanger and gets cooled down to the room temperature.

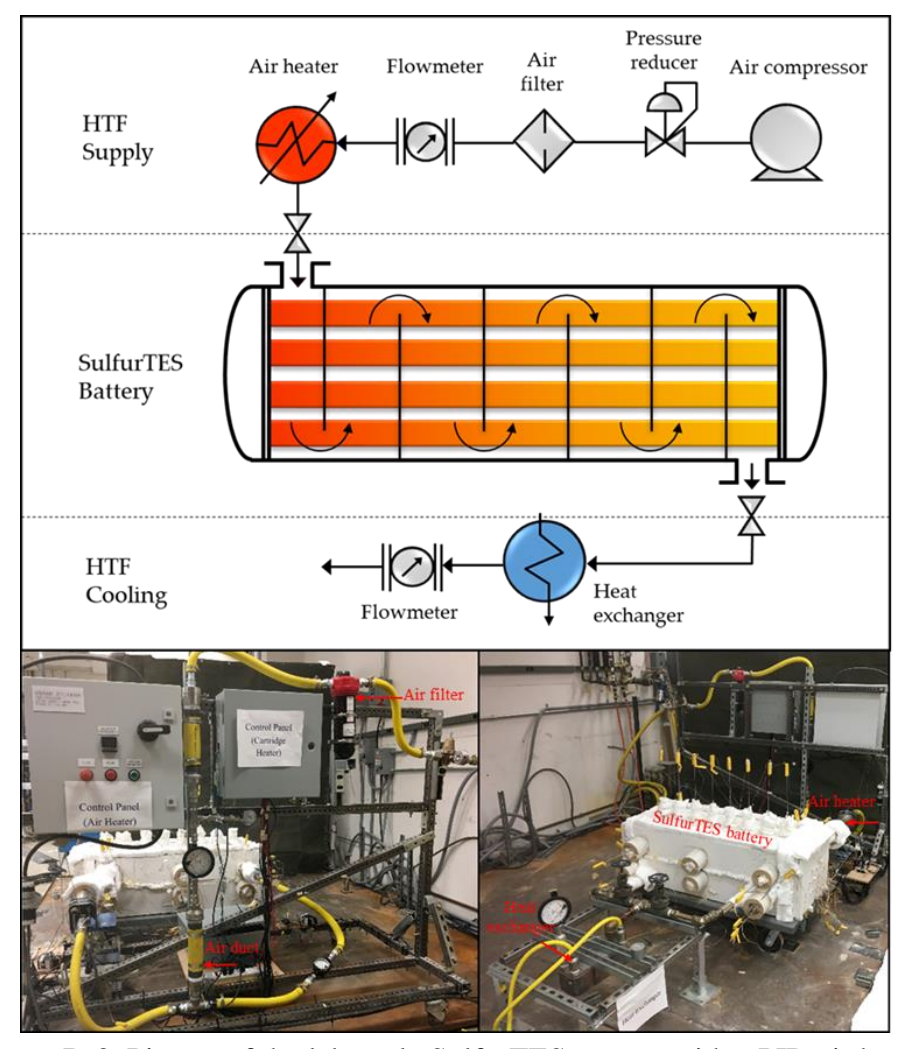


Figure B-3. Picture of the lab-scale SulfurTES system with a PID air heater.

Multiple thermal tests have been conducted to thermally charge and discharge the system from 200 to 600 °C and the inlet air temperature is shown in Figure B-4(a). From Figure B-4(b), the maximum stored thermal energy in around 10 thermal cycles has achieved the 7-kW target, about 50% of which are stored within the sulfur. In this system, 5.5-cm (2") OD and Sch. 40 stainless steel tubes are used to guarantee the operation safety of the system. However, for the SulfurTES with 22-cm (8") OD and Sch. 10 storage tubes (which have been proved to be safely operated with molten sulfur for over 40 years [63]), over 84% thermal energy can be stored in the molten sulfur. This lab-scale system can also achieve a significant high volumetric energy density of 255 kWh/m³. In conclusion, this

demonstration proves that the SulfurTES thermal battery is feasible for high-temperature and low-cost thermal storage applications.

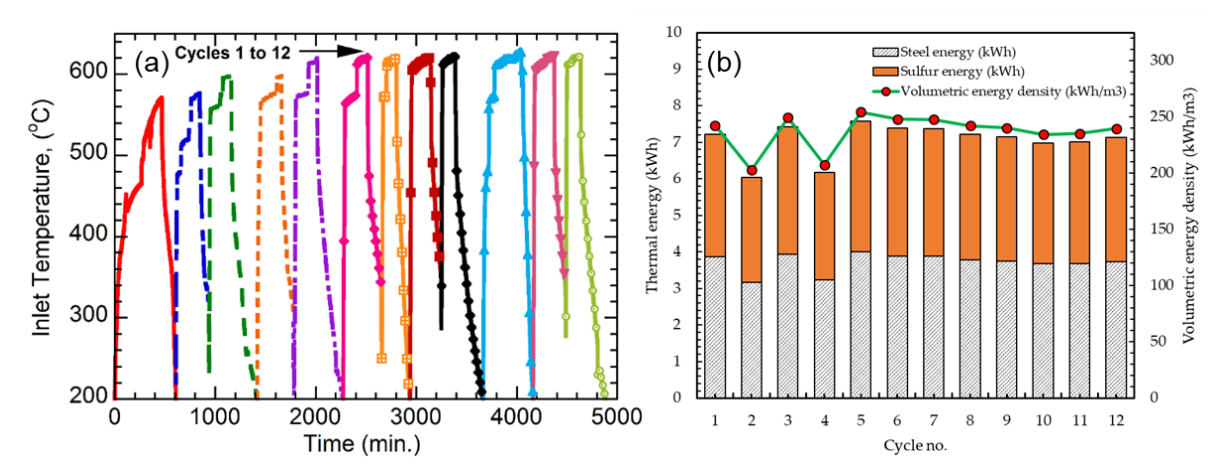


Figure B-4. (a) Inlet temperature for continuous 12 thermal cycles for the lab-scale SulfurTES system with a PID air heater.

The other SulfurTES demonstration is the pilot-scale thermal battery integrated with an on-sun concentrated solar power (CSP) system. This system is analogous to the lab-scale system and consists of twelve 11-cm (4") OD and Sch. 10 sulfur storage tubes as shown in Figure B-5(a) and (b). The temperature fields for the sulfur storage tubes can be measured by the equipped thermocouples shown in Figure B-5(c). The pilot-scale thermal battery is divided into 4 sections and each section consists of 3 tubes. Three thermocouples are attached on one tube (shown with a hatched cross-section in Figure B-5(c)) in each section while the rest of the tubes have 1 thermocouple each. Based on these measurements during the thermal test, the overall storage capacity of the system can be calculated.

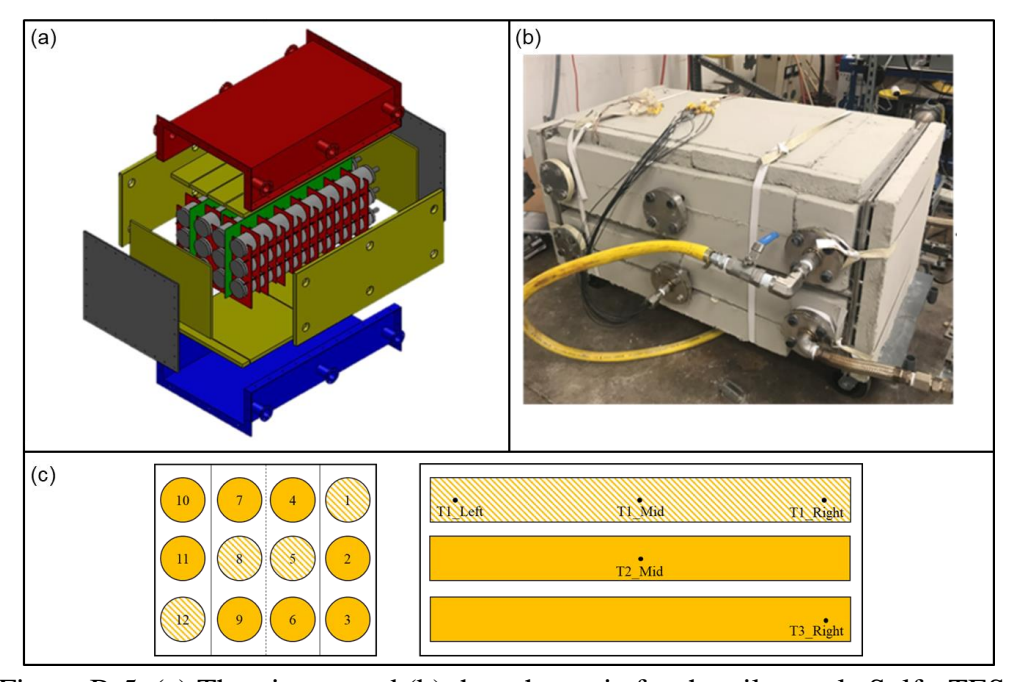


Figure B-5. (a) The picture and (b) the schematic for the pilot-scale SulfurTES.

The on-sun CSP system is developed by the Thermal Storage System, Inc. This CSP dish comprises of 4 pieces of parabolic mirrors that concentrate the solar energy at the focal point, as shown in Figure B-6(a) and (b). These mirrors are installed on a frame which can rotate in horizontal and vertical planes. A photosensor (Figure B-6(c)) is equipped in the system to detect the shift of the sun position and provide the feedback signal for the vertical and horizontal drives (Figure B-6(d) and (e)) to adjust the orientation of the CSP dish to maximum the solar irradiation captured by the system.



Figure B-6. Key components of the on-sun CSP system: (a) parabolic mirrors, (b) concentration of solar energy at the receiver, (c)photosensor, (d) vertical drive, and (e) horizontal drive.

The captured solar energy is collected by a tin-based solar receiver in a cuboid shape. This receiver consists of 5 panels assembled as the 5 surfaces. Figure B-7(a)-(c) show the components for one receiver panel. Each panel is composed of 4 steel tubes immersed in a bulk of liquid tin, though which the air flows as the heat transfer fluid to transfer the solar thermal energy to the SulfurTES system. As shown in Figure B-7(f), the cold air enters the solar receiver from the black hoses on the right-hand side, gets heated in the 5 panels by the concentrated solar thermal energy, and flows to the SulfurTES system thought the conduit on the left hand side (covered with the while ceramic insulation).

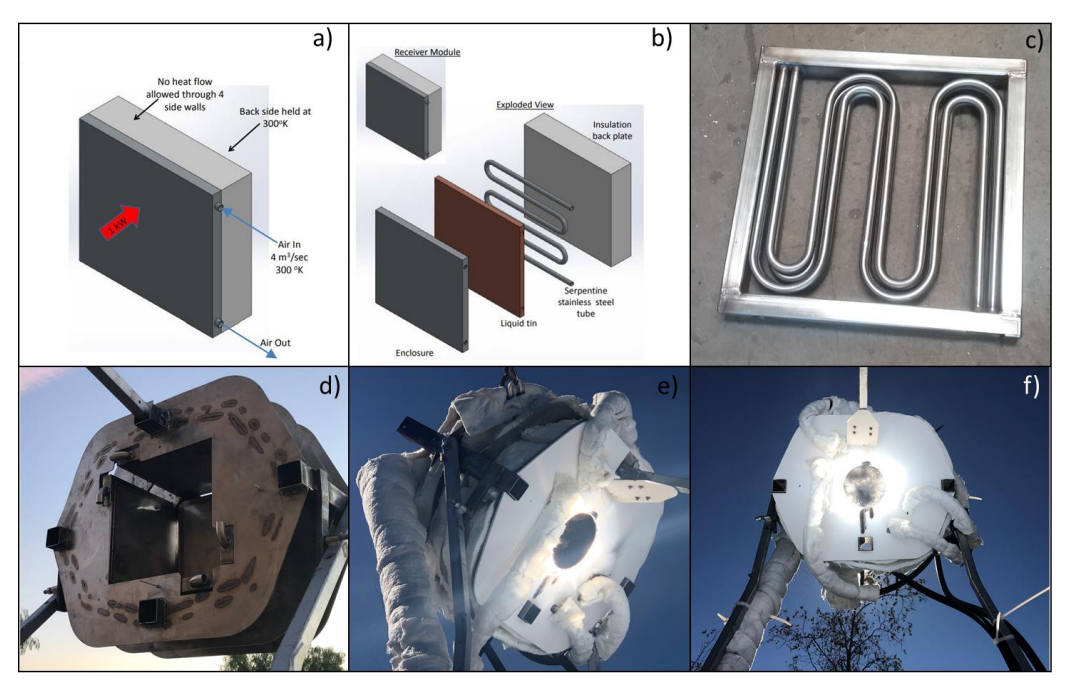


Figure B-7. Schematics and pictures of the solar receiver.

The critical components for this pilot-scale system, including the SulfurTES thermal battery, solar receiver, air (heat transfer fluid) conduit, and relevant instrumentations were carefully installed and assembled as shown in Figure B-8.



Figure B-8. Pictures of the key components for the pilot-scale SulfurTES.

Four cycles of thermal tests were conducted and the temperature field for the 12 storage tubes for one charge process is shown in Figure B-8(a). It can be observed that the thermal battery established a thermal stratification through its flow path and the maximum storage temperature is above 500 °C. Based on the temperature distribution, the stored thermal energy in the system is calculated and plotted in Figure B-9(b). The storage target of 30kWh, proposed by the CEC project, has been achieved in continuous three thermal cycles.

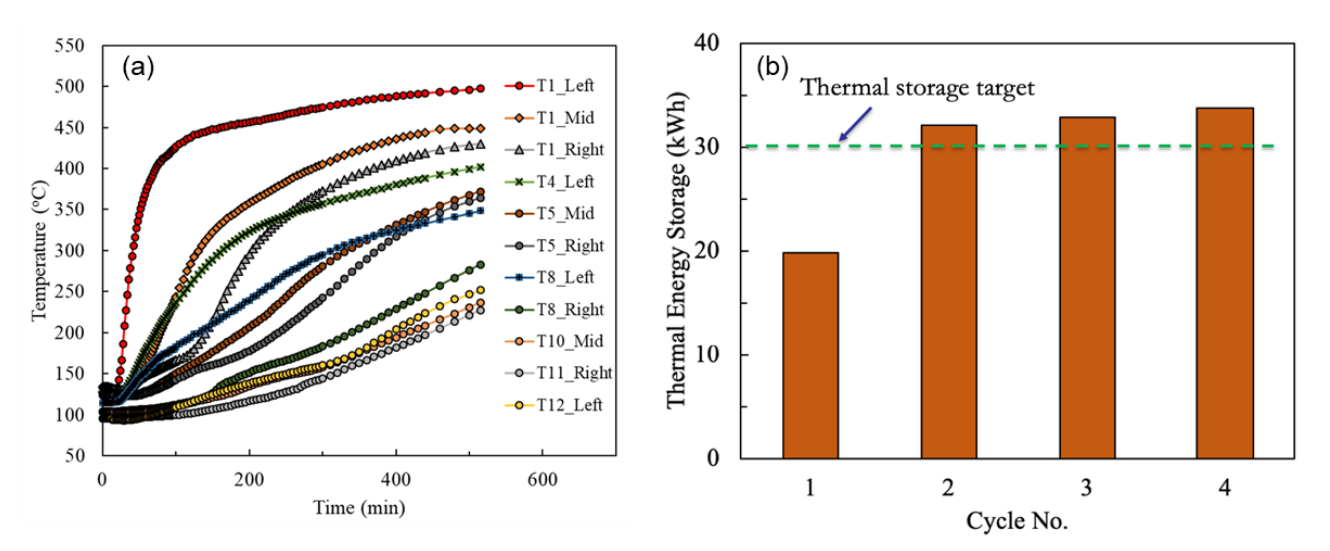


Figure B-9. (a) The temperature distribution of sulfur storage tubes and (b) thermal storage capacity in SulfurTES thermal battery during the thermal charge process.

The pilot-scale SulfurTES system integrated with a CSP system has been successfully demonstrated by the author's team. The study shows the SulfurTES thermal battery system is capable to stably capture and store solar thermal energy at high temperatures. The framework for developing the system provides reliable design bases for the utility-scale SulfurTES system in renewable power generation applications.

Appendix C: Performance analysis for the heat transfer fluid (HTF) side in SulfurTES bath systems

In Chapter 5, the heat transfer behavior in the sulfur side (outside the charge and discharge tubes) has been carefully investigated and quantified. However, the overall system-level performance is also significantly affected by the HTF side (inside the charge and discharge tubes) behavior, such as the pressure drop and heat transfer rate. This analysis is going to compare the HTF side performance in SulfurTES system with tube- and bath configuration and further test the feasibility for the bath system design for low-cost and high-temperature thermal storage.

Heat transfer performance

For the system analogous to a shell-and-tube heat exchanger, the overall heat transfer performance is dominated by both shell side (HTF for the tube-configuration and sulfur for the bath-configuration) and tube side (sulfur for the tube-configuration and HTF for the bath-configuration) heat transfer rates. The overall heat transfer coefficient for both tube- and bath- systems can be expressed as [74]:

$$\frac{1}{h_o} = \frac{1}{h_{sulfur}} + \frac{1}{h_{HTF}} \tag{C.1}$$

Therefore, the HTF side coefficient can also cast a critical effect on the overall heat transfer rate and must be appropriately estimated. Similar to section 5.3, the total system storage capacity, E_t , is assumed to be 1MWh and the system is charged from T_D =200 to T_C = 600 °C in 6 hours (as the charge time, t_{charge}). Assume the air is used as the HTF (all the HTF properties can be estimated as them for air at 400 °C), then the total mass flow rate of HTF is calculated to be:

$$\dot{m}_{HTF} = \frac{E_t}{c_{p_{HTF}}(T_C - T_D)t_{charge}} \approx 0.93 \text{ kg/s}$$
 (C.2)

For the tube-configuration system, the tube diameter, $D_{t,t}$ is selected to be 0.168 m based on the tradeoff between the performance and cost from the study by Wang et al. [64]. In this study, the minimum cross-section area, $A_{cross,t}$, for the external HTF is found to be around 0.045 m², based on the minimum tube pitch ratio of 1.2 in the normal shell-and-tube heat exchangers. With known mass flow rate, \dot{m}_{HTF} , and cross-section area, $A_{cross,t}$, the velocity, u_{HTF} and the Reynolds number, Re_{HTF} , for the HTF in the tube-configuration system can be calculated as:

$$u_{HTF,t} = \frac{\dot{m}_{HTF}}{\rho_{HTF} A_{cross,t}} \approx 40.0 \text{ m/s}$$
 (C.3)

$$Re_{HTF,t} = \frac{\rho_{HTF} u_{HTF,t} D_{t,t}}{\mu_{HTF}} \approx 1.05 \times 10^5$$
 (C.4)

The HTF heat transfer behavior in the tube-configuration system is dominated by the external forced convection over a tube bank, and the heat transfer coefficient, $h_{HTF,t}$, can be estimated through the empirical correlation provided in ref [74]:

$$h_{HTF,t} = \frac{Nu_{HTF,t}k_{HTF}}{D_{t,t}} = \frac{0.35Re_{HTF,t}^{0.6}Pr_{HTF}^{0.36}k_{HTF}}{D_{t,t}} \approx 93.9 \text{ W/m}^2 \cdot \text{K}$$
 (C.5)

For the bath-configuration system, the total mass flow rate of the HTF is the same as it for the tube-configuration system, which is $\dot{m}_{HTF}=0.93$ kg/s. All the geometric parameters, such as $D_{t,b}=5.5$ mm, p=1.43, etc. listed in Table 5.4 are used in this analysis. Assume the 1MWh system consists of multiple shells connected in series, and each of these shells has around $n_t=600$ charge tubes connected in parallel. Then the total cross-section area, $A_{cross,b}$, and the average velocity, $u_{HTF,b}$ can be calculated:

$$A_{cross,b} = 0.25\pi D_{t,b}^2 n_t \approx 0.014 \text{ m}^2$$
 (C.6)

$$u_{HTF,b} = \frac{\dot{m}_{HTF}}{\rho_{HTF} A_{cross,b}} \approx 126 \text{ m/s}$$
 (C.7)

It is worth noting that u_{HTF} for the bath system can be much higher than it in the tube system, since $A_{cross,b}$ is only around 1/3 of $A_{cross,t}$. In opposite to the tube-configuration, the heat transfer mechanism for the HTF in the bath-configuration system is the internal forced convection. The Reynolds number and the relevant heat transfer coefficient, $h_{HTF,b}$, is derived [74] in Equation (C.8) and (C.9).

$$Re_{HTF,b} = \frac{\rho_{HTF} u_{HTF,b} D_{t,b}}{\mu_{HTF}} \approx 1.09 \times 10^4$$
 (C.8)

$$h_{HTF,b} = \frac{Nu_{HTF,b}k_{HTF}}{D_{t,b}} = \frac{0.023Re_{HTF}^{0.8}Pr_{HTF}^{0.4}k_{HTF}}{D_{t,b}} \approx 312 \text{ W/m}^2 \cdot \text{K}$$
 (C.9)

Comparing Equation (C.5) and (C.9), it is observed that the bath-system could have a much higher HTF side heat transfer coefficient due to the less cross-section area for HTF and potentially provide a higher overall heat transfer rate than the SulfurTES with tube-configuration.

Pressure drop analysis

Though benefiting from a higher heat transfer coefficient in the HTF side, the bath-configuration with much smaller HTF cross-section area can have a significantly higher pressure drop than tube-configuration system does. Following equation [74] is used to estimate the total pressure drop, Δp_b , through the SulfurTES bath system:

$$\Delta p_b = \frac{1}{2} f_{HTF,b} \rho u_{HTF,b}^2 \frac{N_t}{n_t} \frac{L_t}{D_{t,b}}$$
 (C.10)

where $f_{HTF,b}$ is the friction factor and for the $3000 < Re_{HTF,b} < 5 \times 10^6$, it can be expressed as:

$$f_D = (0.790 \ln Re_{HTF,b} - 1.64)^{-2}$$
 (C.11)

 $u_{HTF,b}$, $Re_{HTF,b}$, and n_t are shown in Equation (C.7) and (C.8). $N_t = 4137$ and 7200 for two proposed bath systems, respectively, $L_t = 1$ m is the length of one charge tube, and $D_t = 5.5$ mm

which are used in Table 5.4. With these parameters, the system pressure drop Δp_b can be calculated as 1.6 and 2.6 atm for the two bath systems, respectively. Given the maximum pressure for the commercial air compressor is usually larger than 5 atm, the pressure drop through the SulfurTES bath system is acceptable for practical applications. For the SulfurTES with isochoric-tube configuration, since the cross-section area for the HFT is larger than it in the bath system, the pressure drop is found to be smaller than 10^4 Pa, or 0.1 atm for a 1MWh system [64], which is negligible for the industrial-scale systems. Similar to Table 5.4, the comparison for the HTF performance among the tube- and the bath-configuration systems are shown in Table C-1.

Table C-1. HTF-side heat transfer coefficients and system pressure drop for SulfurTES with tube- and bath configurations.

	System capacity [MWh]	Geometric parameters	Total heat transfer area [m²]	HTF-side heat transfer coefficient, h _{HTF} [W/m ² ·K]	System pressure drop, Δp [atm]
Tube system	1	$D_t = 0.168 \text{ m}$	124	93.9	<0.1
		$L_t = 1 \text{ m}$			
		$N_t = 217$			
Bath system I	1	$D_t = 5.5 \text{ mm}$	71.5	312	1.6
		p = 1.43			
		$L_t = 1 \text{ m}$			
		$H = 0.15 \text{ m}$ $(\approx 27D)$			
		$N_t = 4137$			
Bath system II	1	$D_t = 5.5 \text{ mm}$	124	312	2.6
		p = 1.43			
		$L_t = 1 \text{ m}$			
		$H = 0.087 \text{ m}$ $(\approx 16D)$			
		$N_t = 7200$			

In conclusion, for HTF-side performance, the SulfurTES bath system can have a superior heat transfer coefficient due to the less cross-section area for HTF, in comparison to the tube-configuration system. Though the pressure drop for HTF significantly increases with the cross-section area decreasing, the total system pressure drop for the two proposed bath-configuration system is still found to be acceptable for the industrial-scale applications. Furthermore, given advantages on the sulfur-side heat transfer rate as discussed in section 5.3, the SulfurTES bath system can be a promising thermal storage system design with excellent system thermal performance and cost effectiveness.

References

- 1. SolarReserve, "CSP Project Overview," [Online]. Available: https://www.solarreserve.com/en/global-projects/csp/likana.html
- 2. Business Wire, "SolarReserve Receives Environmental Approval for 390 Megawatt Solar Thermal Facility with Storage in Chile," [Online]. Available: https://www.solarreserve.com/en/global-projects/csp/likana.html
- 3. Nuytten, Thomas, Bert Claessens, Kristof Paredis, Johan Van Bael, and Daan Six. "Flexibility of a combined heat and power system with thermal energy storage for district heating." *Applied Energy* 104 (2013): 583-591
- 4. Wells, Parker. Technology-to-Market Analysis of Integrated Combined Heat and Power Plants with Thermal Energy Storage in Commercial Facilities. Diss. UCLA, 2017.
- 5. U.S. Geological Survey, "USGS Minerals Information, Mineral Commodity Summaries: Sulfur," 2019.
- 6. Clark, Peter D., and Norman I. Dowling. "Capture of solar energy using elemental sulfur." *Journal of Sulfur Chemistry*25.1 (2004): 7-11.
- 7. Wirz, Richard E., Antoine Philippe Pierre Stopin, A. Tse Louis, Adrienne G. Lavine, Hossein Pirouz Kavehpour, Reza Baghaei Lakeh, Benjamin I. Furst, Gabriela Bran, and Miguel A. Garcia-Garibay. "High-density, high-temperature thermal energy storage and retrieval." U.S. Patent Application 14/475,479, filed March 5, 2015.
- 8. R. E. Wirz, "Thermal energy storage with supercritical fluids: Final Technical Report (No. DOE-UCLA-AR000140)," University of California at Los Angeles, Los Angeles, CA, 2016.
- 9. R. E. Wirz, "Low-cost thermal energy storage for dispatchable CSP: Critical Project Review Report (No. EPC-14-003)," University of California at Los Angeles, Los Angeles, CA. (Publicly Available by Request to California Energy Commission), 2017.
- 10. Sharma, Atul, V. Veer Tyagi, C. R. Chen, and Dharam Buddhi. "Review on thermal energy storage with phase change materials and applications." *Renewable and Sustainable energy reviews* 13, no. 2 (2009): 318-345.
- 11. Gil, Antoni, Marc Medrano, Ingrid Martorell, Ana Lázaro, Pablo Dolado, Belén Zalba, and Luisa F. Cabeza. "State of the art on high temperature thermal energy storage for power generation.

- Part 1—Concepts, materials and modellization." Renewable and Sustainable Energy Reviews 14, no. 1 (2010): 31-55.
- 12. Herrmann, Ulf, and David W. Kearney. "Survey of thermal energy storage for parabolic trough power plants." *Journal of solar energy engineering* 124.2 (2002): 145-152.
- 13. Hasnain, S. M. "Review on sustainable thermal energy storage technologies, Part I: heat storage materials and techniques." *Energy conversion and management* 39.11 (1998): 1127-1138.
- 14. Stekli, Joseph, Levi Irwin, and Ranga Pitchumani. "Technical challenges and opportunities for concentrating solar power with thermal energy storage." *Journal of Thermal Science and Engineering Applications* 5.2 (2013): 021011.
- 15. Fath, Hassan ES. "Technical assessment of solar thermal energy storage technologies." *Renewable Energy* 14.1-4 (1998): 35-40.
- 16. Dunn, Rebecca I., Patrick J. Hearps, and Matthew N. Wright. "Molten-salt power towers: newly commercial concentrating solar storage." *Proceedings of the IEEE* 100.2 (2012): 504-515.
- 17. Pacheco, James E., Steven K. Showalter, and William J. Kolb. "Development of a molten-salt thermocline thermal storage system for parabolic trough plants." *Journal of solar energy engineering* 124.2 (2002): 153-159.
- 18. Herrmann, Ulf, Bruce Kelly, and Henry Price. "Two-tank molten salt storage for parabolic trough solar power plants." *Energy* 29.5-6 (2004): 883-893.
- 19. Kearney, David, Ulf Herrmann, Paul Nava, B. Kelly, Rod Mahoney, J. Pacheco, Robert Cable, N. Potrovitza, Daniel Blake, and Henry Price. "Assessment of a molten salt heat transfer fluid in a parabolic trough solar field." *Journal of solar energy engineering* 125, no. 2 (2003): 170-176.
- 20. Farid, Mohammed M., Amar M. Khudhair, Siddique Ali K. Razack, and Said Al-Hallaj. "A review on phase change energy storage: materials and applications." *Energy conversion and management* 45, no. 9-10 (2004): 1597-1615.
- 21. Kenisarin, Murat M. "High-temperature phase change materials for thermal energy storage." Renewable and Sustainable energy reviews 14, no. 3 (2010): 955-970.
- 22. Liu, Ming, Wasim Saman, and Frank Bruno. "Review on storage materials and thermal performance enhancement techniques for high temperature phase change thermal storage systems." Renewable and Sustainable Energy Reviews 16.4 (2012): 2118-2132.

- 23. Ge, Haoshan, Haiyan Li, Shengfu Mei, and Jing Liu. "Low melting point liquid metal as a new class of phase change material: An emerging frontier in energy area." *Renewable and Sustainable Energy Reviews* 21 (2013): 331-346.
- 24. Hoshi, Akira, David R. Mills, Antoine Bittar, and Takeo S. Saitoh. "Screening of high melting point phase change materials (PCM) in solar thermal concentrating technology based on CLFR." *Solar Energy* 79, no. 3 (2005): 332-339.
- 25. Wang, Jian-Ping, Xing-Xiang Zhang, and Xue-Chen Wang. "Preparation, characterization and permeation kinetics description of calcium alginate macro-capsules containing shape-stabilize phase change materials." *Renewable Energy* 36.11 (2011): 2984-2991.
- 26. Zalba, Belen, Jose Ma Marin, Luisa F. Cabeza, and Harald Mehling. "Review on thermal energy storage with phase change: materials, heat transfer analysis and applications." *Applied thermal engineering* 23, no. 3 (2003): 251-283.
- 27. Nithyanandam, K., and R. Pitchumani. "Computational studies on a latent thermal energy storage system with integral heat pipes for concentrating solar power." *Applied Energy* 103 (2013): 400-415.
- 28. Kim, Taeil, David M. France, Wenhua Yu, Weihuan Zhao, and Dileep Singh. "Heat transfer analysis of a latent heat thermal energy storage system using graphite foam for concentrated solar power." *Solar Energy* 103 (2014): 438-447.
- 29. Cot-Gores, Jaume, Albert Castell, and Luisa F. Cabeza. "Thermochemical energy storage and conversion: A-state-of-the-art review of the experimental research under practical conditions." Renewable and Sustainable Energy Reviews 16.7 (2012): 5207-5224.
- 30. Pardo, Pedro, Alexandre Deydier, Zoé Anxionnaz-Minvielle, Sylvie Rougé, Michel Cabassud, and Patrick Cognet. "A review on high temperature thermochemical heat energy storage." Renewable and Sustainable Energy Reviews 32 (2014): 591-610.
- 31. Chen, Chen, Hamarz Aryafar, Keith M. Lovegrove, and Adrienne S. Lavine. "Modeling of ammonia synthesis to produce supercritical steam for solar thermochemical energy storage." *Solar Energy* 155 (2017): 363-371.
- 32. Lovegrove, Keith, Andreas Luzzi, I. Soldiani, and Holger Kreetz. "Developing ammonia based thermochemical energy storage for dish power plants." *Solar Energy* 76, no. 1-3 (2004): 331-337.

- 33. Schmidt, Matthias, Christoph Szczukowski, Christian Roßkopf, Marc Linder, and Antje Wörner. "Experimental results of a 10 kW high temperature thermochemical storage reactor based on calcium hydroxide." *Applied Thermal Engineering* 62, no. 2 (2014): 553-559.
- 34. Azpiazu, M. N., J. M. Morquillas, and A. Vazquez. "Heat recovery from a thermal energy storage based on the Ca (OH) 2/CaO cycle." *Applied Thermal Engineering* 23.6 (2003): 733-741.
- 35. H Abedin, Ali, and Marc A Rosen. "A critical review of thermochemical energy storage systems." *The open renewable energy journal* 4, no. 1 (2011).
- 36. Medrano, Marc, Antoni Gil, Ingrid Martorell, Xavi Potau, and Luisa F. Cabeza. "State of the art on high-temperature thermal energy storage for power generation. Part 2—Case studies." *Renewable and Sustainable Energy Reviews* 14, no. 1 (2010): 56-72.
- 37. Flueckiger, Scott, Zhen Yang, and Suresh V. Garimella. "An integrated thermal and mechanical investigation of molten-salt thermocline energy storage." *Applied Energy* 88.6 (2011): 2098-2105.
- 38. Xu, Chao, Zhifeng Wang, Yaling He, Xin Li, and Fengwu Bai. "Sensitivity analysis of the numerical study on the thermal performance of a packed-bed molten salt thermocline thermal storage system." *Applied Energy* 92 (2012): 65-75.
- 39. Yang, Zhen, and Suresh V. Garimella. "Thermal analysis of solar thermal energy storage in a molten-salt thermocline." *Solar energy* 84, no. 6 (2010): 974-985.
- 40. Turchi, Craig S., Judith Vidal, and Matthew Bauer. "Molten salt power towers operating at 600–650° C: Salt selection and cost benefits." *Solar Energy* 164 (2018): 38-46.
- 41. Mehos, Mark, Craig Turchi, Jennie Jorgenson, Paul Denholm, Clifford Ho, and Kenneth Armijo. On the Path to SunShot-Advancing Concentrating Solar Power Technology, Performance, and Dispatchability. No. NREL/TP-5500-65688 SAND-2016-2237 R. EERE Publication and Product Library, 2016.
- 42. Garg, Pardeep, Pramod Kumar, and Kandadai Srinivasan. "Supercritical carbon dioxide Brayton cycle for concentrated solar power." *The Journal of Supercritical Fluids* 76 (2013): 54-60.
- 43. Laing, Doerte, Dorothea Lehmann, Michael Fiß, and Carsten Bahl. "Test results of concrete thermal energy storage for parabolic trough power plants." *Journal of Solar Energy Engineering* 131, no. 4 (2009): 041007.
- 44. Meier, Anton, Christian Winkler, and Daniel Wuillemin. "Experiment for modelling high temperature rock bed storage." *Solar energy materials* 24.1-4 (1991): 255-264.

- 45. Zanganeh, Giw, Andrea Pedretti, Simone Zavattoni, Maurizio Barbato, and Aldo Steinfeld. "Packed-bed thermal storage for concentrated solar power—Pilot-scale demonstration and industrial-scale design." *Solar Energy* 86, no. 10 (2012): 3084-3098.
- 46. Nithyanandam, K., R. Pitchumani, and A. Mathur. "Analysis of a latent thermocline storage system with encapsulated phase change materials for concentrating solar power." *Applied energy* 113 (2014): 1446-1460.
- 47. Nithyanandam, K., and R. Pitchumani. "Cost and performance analysis of concentrating solar power systems with integrated latent thermal energy storage." *Energy* 64 (2014): 793-810.
- 48. Singh, Dileep, Weihuan Zhao, Wenhua Yu, David M. France, and Taeil Kim. "Analysis of a graphite foam—NaCl latent heat storage system for supercritical CO2 power cycles for concentrated solar power." *Solar Energy* 118 (2015): 232-242.
- 49. Zhao, Weihuan, David M. France, Wenhua Yu, Taeil Kim, and Dileep Singh. "Phase change material with graphite foam for applications in high-temperature latent heat storage systems of concentrated solar power plants." *Renewable Energy* 69 (2014): 134-146.
- 50. Aydin, Devrim, Sean P. Casey, and Saffa Riffat. "The latest advancements on thermochemical heat storage systems." *Renewable and Sustainable Energy Reviews* 41 (2015): 356-367.
- 51. Lavine, Adrienne S., Keith M. Lovegrove, Joshua Jordan, Gabriela Bran Anleu, Chen Chen, Hamarz Aryafar, and Abdon Sepulveda. "Thermochemical energy storage with ammonia: Aiming for the sunshot cost target." In *AIP Conference Proceedings*, vol. 1734, no. 1, p. 050028. AIP Publishing, 2016.
- 52. Lavine, Adrienne. Final Report UCLA-Thermochemical Storage with Anhydrous Ammonia. United States: N. p., 2018. Web. doi:10.2172/1425351.
- 53. Chen, Chen, Keith M. Lovegrove, Abdon Sepulveda, and Adrienne S. Lavine. "Design and optimization of an ammonia synthesis system for ammonia-based solar thermochemical energy storage." *Solar Energy* 159 (2018): 992-1002.
- 54. Tuller, William N. "The sulphur data book." *The sulphur data book.* (1954).
- 55. Meyer, Beat. "Elemental sulfur." Chemical Reviews 76.3 (1976): 367-388.
- 56. Powell, Richard E., and Henry Eyring. "The properties of liquid sulfur." *Journal of the American Chemical Society* 65.4 (1943): 648-654.

- 57. Bacon, Raymond F., and Rocco Fanelli. "The Viscosity of Sulfur." *Journal of the American Chemical Society* 65.4 (1943): 639-648.
- 58. Fanelli, Rocco. "Modifying the viscosity of sulfur." *Industrial & Engineering Chemistry* 38.1 (1946): 39-43.
- 59. Rubero, P. A. "Effect of Hydrogen Sulfide on the Viscosity of Sulfur." *Journal of Chemical & Engineering Data* 9.4 (1964): 481-484.
- 60. West, James R. "Thermodynamic properties of sulfur." *Industrial & Engineering Chemistry* 42.4 (1950): 713-718.
- 61. Lewis, Gilbert N., and Merle Randall. "THE HEAT CONTENT OF THE VARIOUS FORMS OF SULFUR." *Journal of the American Chemical Society* 33.4 (1911): 476-488.
- 62. El-Sharkawy, A. A., and M. T. Dessouky. "Measurement of thermal conductivity, heat capacity, and thermal diffusivity of sulfur and selenium in the liquid state." *International journal of thermophysics* 4.2 (1983): 115-125.
- 63. Naik, Siddhesh Sunil. A Parametric Study and Structural Analysis of Isochorically Stored Sulfur Thermal Batteries. Diss. UCLA, 2018.
- 64. Wang, Yide. Performance and Cost Analysis of Sulfur-based Thermal Energy Storage System. Diss. UCLA, 2019.
- 65. Lavine, Adrienne. Final Report UCLA-Thermochemical Storage with Anhydrous Ammonia. No. DE-EE0006536. Univ. of California, Los Angeles, CA (United States), 2018.
- 66. Nithyanandam, K., A. Barde, R. Baghaei Lakeh, and R. E. Wirz. "Charge and discharge behavior of elemental sulfur in isochoric high temperature thermal energy storage systems." *Applied Energy* 214 (2018): 166-177.
- 67. Nithyanandam, Karthik, Amey Barde, Reza Baghaei Lakeh, and Richard Wirz. "Design and analysis of low-cost thermal storage system for high efficiency concentrating solar power plants." In ASME 2016 10th International Conference on Energy Sustainability collocated with the ASME 2016 Power Conference and the ASME 2016 14th International Conference on Fuel Cell Science, Engineering and Technology, pp. V001T05A007-V001T05A007. American Society of Mechanical Engineers, 2016.
- 68. Nithyanandam, Karthik, Amey Barde, Louis Tse, Reza Baghaei Lakeh, and Richard Wirz. "Heat transfer behavior of sulfur for thermal storage applications." In ASME 2016 10th International Conference on Energy Sustainability collocated with the ASME 2016 Power Conference and the ASME 2016

- 14th International Conference on Fuel Cell Science, Engineering and Technology, pp. V001T05A008-V001T05A008. American Society of Mechanical Engineers, 2016.
- 69. Barde, Amey, Karthik Nithyanandam, Mitchell Shinn, and Richard E. Wirz. "Sulfur heat transfer behavior for uniform and non-uniform thermal charging of horizontally-oriented isochoric thermal energy storage systems" *International Journal of Heat and Mass Transfer*, under revision.
- 70. Barde, Amey, Kaiyuan Jin, Mitchell Shinn, Karthik Nithyanandam, and Richard E. Wirz. "Demonstration of a low cost, high temperature elemental sulfur thermal battery." *Applied Thermal Engineering* 137 (2018): 259-267.
- 71. Lakeh, Reza Baghaei, H. Pirouz Kavehpour, Adrienne S. Lavine, Gani B. Ganapathi, and Richard E. Wirz. "Study of Turbulent Natural Convection in Vertical Storage Tubes for Supercritical Thermal Storage System." In ASME 2013 International Mechanical Engineering Congress and Exposition, pp. V06BT07A030-V06BT07A030. American Society of Mechanical Engineers, 2013.
- 72. Rosen, M. A., Raymond Tang, and Ibrahim Dincer. "Effect of stratification on energy and exergy capacities in thermal storage systems." *International Journal of Energy Research*28.2 (2004): 177-193.
- 73. Rosen, M. A., and I. Dincer. "Exergy methods for assessing and comparing thermal storage systems." *International Journal of Energy Research* 27.4 (2003): 415-430.
- 74. Bergman, Theodore L., Frank P. Incropera, David P. DeWitt, and Adrienne S. Lavine. *Fundamentals of heat and mass transfer*. John Wiley & Sons, 2011.
- 75. Evans, L. B., R. C. Reid, and E. M. Drake. "Transient natural convection in a vertical cylinder." *AIChE Journal* 14.2 (1968): 251-259.
- 76. Churchill, Stuart W., and Humbert HS Chu. "Correlating equations for laminar and turbulent free convection from a vertical plate." *International journal of heat and mass transfer*18.11 (1975): 1323-1329.
- 77. Lakeh, Reza Baghaei, Adrienne S. Lavine, H. Pirouz Kavehpour, and Richard E. Wirz. "Study of turbulent natural convection in vertical storage tubes for supercritical thermal energy storage." *Numerical Heat Transfer, Part A: Applications* 67, no. 2 (2015): 119-139.
- 78. MacGregor, R. K., and Ashley Francis Emery. "Free convection through vertical plane layers—moderate and high Prandtl number fluids." *Journal of Heat Transfer* 91.3 (1969): 391-401.

- 79. Markatos, Nikos C., and K. A. Pericleous. "Laminar and turbulent natural convection in an enclosed cavity." *International Journal of Heat and Mass Transfer* 27.5 (1984): 755-772.
- 80. Shinn, M., K. Nithyanandam, A. Barde, and R. E. Wirz. "Sulfur-based thermal energy storage system using intermodal containment: Design and performance analysis." *Applied Thermal Engineering* 128 (2018): 1009-1021.
- 81. Louis, A. Tse, Gani B. Ganapathi, Richard E. Wirz, and Adrienne S. Lavine. "Spatial and temporal modeling of sub-and supercritical thermal energy storage." *Solar Energy* 103 (2014): 402-410
- 82. Louis, A. Tse, Adrienne S. Lavine, Reza Baghaei Lakeh, and Richard E. Wirz. "Exergetic optimization and performance evaluation of multi-phase thermal energy storage systems." *Solar Energy* 122 (2015): 396-408.
- 83. Schlunder, Ernst U. "Heat exchanger design handbook." (1983).
- 84. Morgan, Vincent T. "The overall convective heat transfer from smooth circular cylinders." *Advances in heat transfer*. Vol. 11. Elsevier, 1975. 199-264.
- 85. Churchill, Stuart W., and Humbert HS Chu. "Correlating equations for laminar and turbulent free convection from a horizontal cylinder." *International journal of heat and mass transfer* 18.9 (1975): 1049-1053.
- 86. Sebastian, Geo, and S. R. Shine. "Natural convection from horizontal heated cylinder with and without horizontal confinement." *International Journal of Heat and Mass Transfer* 82 (2015): 325-334.
- 87. Karim, Farid, B. Farouk, and I. Namer. "Natural convection heat transfer from a horizontal cylinder between vertical confining adiabatic walls." *Journal of heat transfer* 108.2 (1986): 291-298.
- 88. Spinnler, Markus, Edgar RF Winter, and Raymond Viskanta. "Studies on high-temperature multilayer thermal insulations." *International Journal of Heat and Mass Transfer* 47.6-7 (2004): 1305-1312.
- 89. Daryabeigi, Kamran, George R. Cunnington, and Jeffrey R. Knutson. "Combined heat transfer in high-porosity high-temperature fibrous insulation: Theory and experimental validation." *Journal of thermophysics and heat transfer* 25.4 (2011): 536-546.
- 90. Zhang, Bo-Ming, Shu-Yuan Zhao, and Xiao-Dong He. "Experimental and theoretical studies on high-temperature thermal properties of fibrous insulation." *Journal of Quantitative Spectroscopy and Radiative Transfer* 109.7 (2008): 1309-1324.

91. Keller, K., M. Hoffmann, W. Zörner, and J. Blumenberg. "Application of high temperature multilayer insulations." *Acta Astronautica* 26, no. 6 (1992): 451-458.